Confronting disk evolution theory with population-scale constraints from radio observations

Luca Delussu

SIGILL · UNIVERSITAT · LUDOVIC · MAXIM

München 2025

Confronting disk evolution theory with population-scale constraints from radio observations

Luca Delussu

Dissertation
der Fakultät für Physik
der Ludwig-Maximilians-Universität
München

vorgelegt von
Luca Delussu
aus Italy

München, den 20. Februar 2025

Erstgutachter: Prof. Dr. Til Birnstiel
Zweitgutachter: Prof. Dr. Giovanni Rosotti
Tag der mündlichen Prüfung: 08. April 2025

Contents

Zusammenfassung

Die Einführung des Atacama Large Millimeter/Sub-Millimeter Array (ALMA) hat die Erforschung protoplanetarer Scheiben in den letzten Jahren erheblich revolutioniert. Die hochauflösenden ALMA-Beobachtungen ermöglichten die Untersuchung und Charakterisierung einzelner Scheiben im Detail und enthüllten die Existenz von Substrukturen und deren Allgegenwärtigkeit in hellen Scheiben. Darüber hinaus ermöglichte die ständig wachsende Zahl großer Millimeter-Durchmusterungen ganzer Sternentstehungsgebiete die Untersuchung ganzer Populationen von Planeten bildenden Scheiben, wobei Korrelationen zwischen ihren beobachtbaren Eigenschaften sichtbar wurden. In dieser Arbeit werden zwei Populationssynthesestudien vorgestellt, die darauf abzielen, die Parameter und Anfangsbedingungen von planetenbildenden Scheiben zu untersuchen und einzugrenzen sowie die Schlüsselmechanismen zu identifizieren, die bei der Reproduktion der beobachteten Verteilungen von Scheiben in der Lupus-Region eine Rolle spielen. Die erste Studie zeigte, dass die allgemein beobachteten niedrigen Spektralindizes eine signifikante Substruktur erfordern, wie sie von Planeten mit Massen von Saturn bis zu einigen Jupitern hervorgerufen wird, die bereits vor 0.4 Myr vorhanden sein müssen. Scheiben mit relativ hohen Anfangsmassen, mäßigen Turbulenzen und einer bedeutenden und früh gebildeten Substruktur können gleichzeitig die beobachteten Verteilungen für den Spektralindex und die Größen-Leuchtkraft reproduzieren. Nur Trübungen mit hoher Absorptionseffizienz erwiesen sich als fähig, die beobachteten Spektralindizes zu reproduzieren. Die zweite Studie untersuchte die Möglichkeit, die beobachteten Gas-Staub-Größenverhältnisse $R_{\mathrm{gas}}/R_{\mathrm{dust}}$ zu reproduzieren. Da frühere Studien gezeigt haben, dass glatte Scheiben (d.h., Scheiben ohne Substruktur) $R_{\mathrm{gas}}/R_{\mathrm{dust}}$-Werte erzeugen, die größer sind als die beobachteten, wurde die Möglichkeit untersucht, diese Diskrepanz durch substrukturierte Scheiben zu beheben. Während die Einführung von Substruktur(en) diese Diskrepanz verringert, indem sie zu niedrigeren $R_{\mathrm{gas}}/R_{\mathrm{dust}}$-Werten als glatte Scheiben führt, wird das Problem dadurch nicht vollständig gelöst, da die geschätzten Verhältnisse immer noch über den beobachteten liegen. Eine eingehende Untersuchung ergab, dass die Reproduktion der Verhältnisse $R_{\mathrm{gas}}/R_{\mathrm{dust}}$ auch bei Berücksichtigung der externen Photoverdampfung eine Herausforderung darstellt. Die Ergebnisse deuten darauf hin, dass die Diskrepanz zwischen Simulationen und Beobachtungen auf eine ungenaue Schätzung der Gasgrößen der Scheiben zurückzuführen sein könnte. Es wird vorgeschlagen, die Untersuchung in zukünftigen Arbeiten zu erweitern, indem der Parameterraum der Anfangsbedingungen vergrößert und zusätzliche Szenarien, wie z.B. windgetriebene Scheiben, untersucht werden.

Abstract

The advent of the Atacama Large Millimeter/Sub-Millimeter Array (ALMA) significantly revolutionized the study of protoplanetary disks in recent years. ALMA high-resolution observations enabled the study and characterization of individual disks in great detail, revealing the existence of substructures and their ubiquity in bright disks. Furthermore, the ever-increasing number of large millimeter surveys of entire star-forming regions enabled the study of entire populations of planet-forming disks revealing correlations between their observable properties. This thesis presents two population synthesis studies aimed at investigating and constraining parameters and initial conditions of planet-forming disks and identifying key mechanisms at play to reproduce observed distributions of disks in the Lupus region. The first study showed that the generally low observed spectral indices call for significant substructure, such as that induced by planets with masses ranging from Saturn to a few Jupiters, to already be present before 0.4 Myr. Disks with relatively high initial masses, moderate levels of turbulence, and significant and early formed substructure can simultaneously reproduce the observed distributions for both the spectral index and size–luminosity. Only opacities with high absorption efficiency proved capable of reproducing the observed spectral indices. The second study explored the possibility of reproducing the observed gas-dust size ratios $R_{\mathrm{gas}}/R_{\mathrm{dust}}$. Given that previous studies showed that smooth disks (i.e., disks without substructure) produce $R_{\mathrm{gas}}/R_{\mathrm{dust}}$ values larger than the observed ones, the possibility for substructured disks to address this discrepancy was examined. While the introduction of substructure(s) reduces this discrepancy by producing lower $R_{\mathrm{gas}}/R_{\mathrm{dust}}$ than smooth disks, it does not fully address the problem, as the estimated ratios still exceed the observed ones. An in-depth investigation revealed that even when accounting for external photoevaporation, reproducing $R_{\mathrm{gas}}/R_{\mathrm{dust}}$ ratios remains challenging. The results suggested that the discrepancy between simulations and observations may arise from an inaccurate estimate of the gas sizes of the disks. It is then proposed to extend the investigation in future work broadening the parameter space of the initial conditions and exploring additional scenarios, such as wind-driven disks.

Chapter 1

Protoplanetary disks

The study of protoplanetary disks lies at the heart of modern astrophysics, as these structures serve as the birthplaces for planetary systems. This chapter delves into the evolution of the protoplanetary disk field, providing a comprehensive overview of the current state of protoplanetary disk research, from its historical origins to the latest observational and theoretical advancements. Section 1.1 provides an overview of the early development of the protoplanetary disk field, tracing its origins from early philosophical concepts, such as Kant and Laplace's nebular hypothesis. It examines the first indirect evidence for accreting disks around forming stars, which emerged in the 1970s through observations of young stellar objects (YSOs). Section 1.2 explores the theory of protoplanetary disk evolution, with a particular focus on the nature of protoplanetary disks as accretion disks. The focus of Section 1.3 shifts to the dust component of protoplanetary disks. Although dust represents only a small fraction of a disk's total mass, it plays a critical role in shaping the disk's structure, chemical evolution, and dynamics. As a primary tracer of disk properties, dust particles provide invaluable insight into disk evolution. Section 1.4 reviews recent advancements in protoplanetary disk observations, focusing on the impact of the advent of the Atacama Large Millimeter/Sub-Millimeter Array (ALMA). ALMA's high-resolution observations have enabled detailed studies of individual disks, while large samples of lower-resolution observations have uncovered correlations between several disk-star observables. The section also discusses current methods for estimating key disk parameters, such as mass and size for both dust and gas components, and the challenges in obtaining accurate measurements. Finally, Section 1.5 introduces disk population synthesis, a valuable tool for investigating and constraining the parameters and initial conditions of protoplanetary disks, as well as exploring the new range of questions raised by recent large sample surveys.

1.1 From stars to planets, via protoplanetary disks

Tracing the moment when the term 'protoplanetary disk' was first introduced in scientific literature is a challenging scientific archaeological task, as the term gradually emerged and gained popularity over time, ultimately becoming widely accepted in the literature. In particular, it began to take hold in the 1970s, when theories of planetary and star formation began to flourish. However, the concept of a ’protoplanetary disk’ existed long before the term was coined, circulating in both scientific and non-scientific discussions. It is unsurprising that, as often occurs in the history of science—particularly in the field of astronomy, which has long served as a crossroads for various artistic and intellectual pursuits—the precursors to the protoplanetary disk theory were polymaths such as Immanuel Kant (1755) and Pierre-Simon Laplace (1796), with their nebular hypothesis. While the authorship of the nebular hypothesis is typically attributed to Kant and Laplace, an early, embryonic formulation of this idea can be traced back to the works of Emanuel Swedenborg in 1734. Kant further developed Swedenborg’s preliminary concept, eventually publishing the final version of the nebular hypothesis anonymously in his "Universal Natural History and Theory of the Heavens" in 1755. In his "Exposition du système du monde", published in 1796, Laplace presented a similar model. However, the concept of the protoplanetary disk did not emerge until the second half of the last century, when the theoretical development of star and planet formation theories, along with the advent of modern, powerful observational techniques, paved the way for the development of protoplanetary disk theories and their first (indirect) observations. Indeed, general progress and interest in protoplanetary disks have always been intimately linked to the development of star and planetary formation theories.

Theoretical works by Shakura and Sunyaev (1973) Shakura & Sunyaev (1973) and Lynden-Bell & Pringle (1974) paved the way for the development of the protoplanetary disk field and are now considered seminal papers in the protoplanetary disk field. As the idea of protoplanetary disk formation within the framework of stellar and planetary formation gained increasing theoretical consensus, the first indirect evidence for the existence of accreting disks around forming stars emerged in the 1970s through observations of young stellar objects (YSOs). The infrared excess emission observed from YSOs suggested the presence of dust surrounding the forming stars, while ultraviolet excess indicated accretion onto the star, thus reinforcing the concept of protoplanetary disks. In this context, two pivotal observational studies were conducted in the 1980s: Lada & Wilking (1984) and Adams et al. (1987). Lada and Wilking observed YSO sources embedded in the ρ Ophiuchi dark cloud at mid-infrared wavelengths and, in particular, introduced a classification scheme for these objects based on the slope of the observed spectral energy distribution (SED) between near-IR and mid-IR wavelengths. The latter is defined as:

$$\alpha_{IR} = \frac{dlog(\lambda F_\lambda)}{dlog\lambda}, \tag{1.1}$$

for a wavelength λ in the range $1\mu m - 20\mu m$ in Lada and Wilking study, but nowadays λ typically relies in the range $2\mu m - 25\mu m.$ F_λ is the flux per unit wavelength λ. Based on the value of α_{IR}, Lada and Wilking subdivided the observed objects into three classes:

- Class 0: no near-IR emission, thus α_{IR} is undefined,
- Class I: $\alpha_{IR} \geq 0$,

- Class II: $\alpha_{IR} < 0$.

Later, Adams et al. (1987) introduced an evolutionary interpretation of the classes defined by Lada and Wilking. Class 0 represents an early evolutionary stage in which the forming star is heavily embedded in the infalling gas and dust cloud, which also surrounds the forming protoplanetary disk. In Class I, the star begins to emerge from the surrounding cloud, although it remains partially obscured, and the cloud continues to contribute to infall toward the disk. Class II objects have lost their envelopes and thus no longer experience the infall process but are characterized by relatively massive and often actively accreting disks. A classification proposed by Williams & Cieza (2011) introduced Class III YSOs, which are characterized by weak or no infrared excess emission. Evolutionarily, these objects are associated with the stage in which the disk has dissipated. The study of YSOs and protoplanetary disks provides valuable insight into the early stages of star and planet formation, which is essential for understanding the origins of planetary systems, including our own. Protoplanetary disk theories typically assume a disk in the Class II stage, a phase where the disk has fully decoupled from the infall process. The Class II stage is widely adopted as the starting point for planet formation theories as well. However, recent studies suggest that planet formation may begin as early as the Class I stage. Additionally, protoplanetary disk studies have emphasized the importance of the Class I stage in the overall evolution of the disk, raising the question of whether it is appropriate to base theories solely on the Class II stage.

1.2 Protoplanetary disk evolution

A protoplanetary disk is a rotating circumstellar structure composed of gas and dust that forms around a forming star due to the conservation of angular momentum from the infalling molecular cloud. Although their evolution does not occur on a fast timescale, protoplanetary disks are far from static structures. They evolve through interactions with the host (forming) star, the surrounding environment, and the mutual interactions between their internal dust and gas components. The UV excess observed in the spectral energy distribution of YSOs is a clear indicator and a fundamental evolutionary driver of protoplanetary disk evolution. The UV excess is generated by the emission from material at the star's surface, which is heated by material transported from the protoplanetary disk to the star (accretion process). While it is understood that protoplanetary disks behave as accretion disks, the theoretical explanation of this mechanism remains far from straightforward. It is well-established that for gas to be accreted by the star, it must lose angular momentum, but identifying the physical mechanism responsible for this loss remains an open problem within the scientific community. The necessity for gas to lose angular momentum to be accreted by the star arises from the fact that the angular momentum of the gas increases with distance from the star. This can be demonstrated by deriving the orbital velocity of the disk gas. Starting from the momentum equation for an inviscid and non-magnetized fluid,

$$\frac{\partial \mathbf{v}}{\partial t} + (\mathbf{v} \cdot \nabla)\mathbf{v} = -\frac{1}{\rho}\nabla P - \nabla \Phi, \tag{1.2}$$

where $\mathbf{v}$ is the fluid velocity, ρ the density, P the pressure and Φ the gravitational potential. Focusing on a stationary axisymmetric flow scenario in which the potential is dominated by that of the hosting star of mass $M_\star$, the radial component of the equation of motion reduces to

$$\frac{v_{\phi,gas}}{r} = \frac{GM_\star}{r^2} + \frac{1}{\rho}\frac{dP}{dr}, \tag{1.3}$$

which simply express the radial force balance between gravity, radial pressure gradient and centrifugal force. Assuming a power law for the radial pressure profile, that is $P \propto r^{-n}$, and a pressure $P(r_0) \equiv P_0 = \rho_0 c_s^2$ at a reference radius r_0, eq. 1.2 becomes

$$v_{\phi,gas} = v_k \left(1 - n\frac{c_s^2}{v_k^2}\right)^{1/2} = v_k\sqrt{1-2\eta}, \tag{1.4}$$

where $v_k = r\Omega_k = r\sqrt{\frac{GM_\star}{r^3}} = \sqrt{\frac{GM_\star}{r}}$ is the Keplerian velocity and the parameter which η defines the sub-Keplerity of the gas. Thus, the gas moves at sub-Keplerian velocity in the disk. Nevertheless, for a geometrically thin disk, the deviation from Keplerian velocity is minimal, and it can be safely assumed that the gas velocity is essentially the Keplerian velocity. Thus, the specific angular momentum of the gas is given by

$$l = rv_{\phi,gas} \simeq \sqrt{GM_\star r}. \tag{1.5}$$

The sub-Keplerian nature of the gas plays an important role and has to be taken into account when considering the motion of the dust particles in the disk (see Section 1.3). Equation 1.5 shows that the specific specific angular momentum of the gas is an increasing function of the radial distance r. As mentioned earlier, this implies that the gas must lose angular momentum to flow inward and be accreted by the host star. A mechanism capable of producing this loss of angular momentum is therefore necessary to drive accretion. More precisely, since the global conservation of angular momentum must hold, a redistribution of angular momentum within the disk is required. Indeed, reducing the angular momentum of gas so that local gas parcels can move inward necessitates that other gas parcels in the disk acquire angular momentum and move outward. Friction, commonly referred to as viscosity, arises from internal stresses within the disk and enables the redistribution of angular momentum, driving accretion and disk evolution. This mechanism was initially assumed to be the primary driver of protoplanetary disk evolution in early theories. However, modern theories have begun exploring the possibility that disk evolution may also be driven by the loss of angular momentum through disk winds. It remains a subject of ongoing debate whether disk evolution is primarily driven by viscosity or by disk winds (Bai & Stone 2013; Trapman et al. 2022; Zagaria et al. 2022; Tabone et al. 2022; Somigliana et al. 2023). In the main work of this thesis, presented in Chapter 3, viscous disks have been taken into account and the protoplanetary gas disk has been evolved according to the viscous disk evolution equation (Lynden-Bell & Pringle 1974) using the turbulent effective viscosity as parameterized in (Shakura & Sunyaev 1973). Therefore, the final part of this section will focus on introducing these works.

The evolution of the gas surface density Σ_{gas} can be derived from the continuity equation and the azimuthal component of the momentum equation. Assuming an axis-symmetric and thin disk, the mass continuity equation, expressing the conservation of mass, reads

$$r\frac{\partial \Sigma}{\partial t} + \frac{\partial}{\partial r}(r\Sigma v_r), \tag{1.6}$$

while the azimuthal component of the momentum equation, expressing the angular momentum conservation, as described by Pringle (1981) is given by

$$r\frac{\partial}{\partial t}(r^2\Omega\Sigma) + \frac{\partial}{\partial r}(r^2\Omega \cdot r\Sigma v_r) = \frac{1}{2\pi}\frac{\partial G}{\partial r}, \tag{1.7}$$

where Ω and $v_r \equiv v_r(r,t)$ are respectively the angular and the radial velocity of the gas in the disk. The torque G acting on an annulus, for a viscous fluid is given by

$$G = 2\pi r \cdot \nu \Sigma_{gas} r \frac{d\Omega}{dr} \cdot r, \tag{1.8}$$

where ν is the kinematic viscosity. Substituting eq. 1.8 in eq. 1.6 and combining it with eq. 1.7 the general equation governing the evolution of a viscous accretion disk with an arbitrary rotation profile $\Omega(r)$ is obtained:

$$\frac{\partial \Sigma}{\partial t} = -\frac{1}{r}\frac{\partial}{\partial r}\left[\frac{1}{\frac{\partial}{\partial r}(r^2\Omega)}\frac{\partial}{\partial r}\left(r^3\nu\Sigma\frac{d\Omega}{dr}\right)\right]. \tag{1.9}$$

If it is assumed that the disk is in Keplerian rotation, that is $\Omega = \Omega_k = \sqrt{GM_\star/r^3}$, it yields the advective diffusion equation

$$\frac{\partial \Sigma}{\partial t} = \frac{3}{r}\frac{\partial}{\partial r}\left[r^{1/2}\frac{\partial}{\partial r}(\nu\Sigma r^{1/2})\right]. \tag{1.10}$$

Introducing the variables $X \equiv 2r^{1/2}$ and $f \equiv \frac{3}{2}\Sigma X$ and assuming a constant viscosity ν, the diffusive form of the evolution equation 1.10 becomes more transparent

$$\frac{\partial f}{\partial t} = D\frac{\partial^2 f}{\partial X^2}, \tag{1.11}$$

with $D = 12\nu/X^2$ as the diffusion coefficient. Thus the viscous time scale τ_ν of a disk of characteristic size r is

$$\tau_\nu \simeq \frac{r^2}{\nu}. \tag{1.12}$$

A time-dependent analytic solution to eq. 1.10 is provided by the self-similar solution introduced by Lynden-Bell & Pringle (1974). Assuming a power law profile in radius for the viscosity ν, that is

$$\nu \propto r^{\gamma}, \tag{1.13}$$

with $y = constant$, the self-similar solution by Lynden-Bell & Pringle (1974) reads

$$\Sigma_{gas}(\tilde{r}, T) = \frac{C}{3\pi\nu_c \tilde{r}^{\gamma}} T^{-(5/2-\gamma)/(2-\gamma)} exp\left[-\frac{\tilde{r}^{(2-\gamma)}}{T}\right], \tag{1.14}$$

with C as a normalization constant, $\tilde{r} \equiv r/r_c$ and $\nu_c \equiv \nu(r_c)$. Where r_c is the characteristic radius of the disk, namely, the radius out of which the initial surface density profile of the disk is described as a steady-state solution, and as an exponential cut-off for $r > r_c$. Furthermore, T is defined as

$$T \equiv \frac{t}{t_s} + 1, \tag{1.15}$$

with

$$t_s \equiv \frac{1}{3(2-\gamma)^2} \frac{r_c^2}{\nu_c}. \tag{1.16}$$

While conceding that the transport of angular momentum in the disk (and, consequently, the phenomenon of accretion) is driven by viscosity, it is essential to understand the physical origin of this viscosity and the efficiency of angular momentum transport it produces. To this day, these issues are still a matter of debate. The idea that molecular viscosity could be responsible for the evolution of protoplanetary disks can be easily dismissed, as the associated viscous timescale would be on the order of $10^{13} yrs$ for a typical protoplanetary disk, about 1000 times the age of the universe. However, the low molecular viscosity of the disk results in an extremely high Reynolds number ($Re \geq 10^{10}$), implying that the disk will be highly turbulent in the presence of a physical instability. The idea of turbulence as a mechanism for angular momentum transport is the foundation of the α-disk model proposed by Shakura & Sunyaev (1973). The "effective" or "turbulent" viscosity, introduced by Shakura & Sunyaev (1973), arises from the turbulence within the disk and is given by

$$\nu = \alpha c_s h, \tag{1.17}$$

where $\alpha \leq 1$ is the Shakura-Sunyaev α parameter, a dimensionless parameter that measures the efficiency of the angular momentum transport due to the turbulence. The "effective" viscosity form is derived from dimensional arguments. The velocity of the turbulent motion is limited to the sound speed c_s because supersonic motions generate shock and rapid dissipation. The maximum scale of the turbulent motion cannot be larger than the smaller scale in the disk, which is usually given by the local disk scale height h. The formalism introduced by Shakura and Sunyaev offers a potential solution to the problem of identifying the physical mechanism behind angular momentum transport. However, it also introduces a new dilemma: the origin of turbulence within the disk. Nevertheless, the α-disk model provides a potential justification for the power-law profile assumed by

Lynden-Bell & Pringle (1974) and carries the advantage that the accretion equations are close if α is known. Even without knowing the cause of the turbulence, α can be estimated from observations, or, as shown in the study presented in Chapter 3, it can be inferred by comparing simulated and observed disk distributions. A consensus on the value of α has yet to be reached. Classical models in which the turbulence is driven by the magnetorotational instability (MRI)Balbus & Hawley (1991) predict $\alpha \sim 0.001$˘0.01. However, in recent years, it has been suggested Bai & Stone (2013) that non-ideal magnetohydrodynamics (MHD) effects may suppress MRI, leading to an effectively laminar disk, that is, a disk with $\alpha < 0.001$. The study introduced in Chapter 3 shows substructures and a moderate level of turbulence ($10^{-3.5} \leqslant \alpha \leqslant 10^{-2.5}$) are required to reproduce both the observed spectral index and size-luminosity distributions.

1.3 Little, but essential: dust in protoplanetary disks

Although dust constitutes only 1% of the total mass of a protoplanetary disk (Weingartner & Draine 2001), it plays a pivotal role in defining the structure, dynamical and chemical evolution of protoplanetary disks. Furthermore, dust serves as the primary observational tracer and source of information for protoplanetary disks. Indeed, dust particles are the main source of continuum opacity in the disk, determining the scattering or absorption of starlight and thereby shaping the temperature profile of the disk. The chemistry of the disk is intimately linked to dust, as some complex chemical reactions can only occur because of the presence of dust particles (Aikawa & Nomura 2006; Garrod & Herbst 2006). These reactions occur on the surface of dust particles. The study of the dust component is also critically important for the development of planetary formation theories, as it not only indirectly affects planet formation by shaping disk structure and evolution, but dust aggregates constitute the building blocks from which planets and other bodies are formed in the resulting planetary system. To gain insight into the evolution of the protoplanetary disk, it is therefore essential to understand the dynamics, transport, and collisional evolution of dust particles within the disks. Although dust dynamics can be influenced by various mechanisms, drag forces arising from the motion of the dust through the surrounding gas are the primary drivers of dust evolution in protoplanetary disks. Aerodynamic drag on solid particles falls into two regimes: the Epstein regime (Epstein 1924) and the Stokes regime (Stokes et al. 1851). Epstein drag is experienced by dust particles whose size is smaller than the mean free path of the gas molecules (λ_{mfp}), resulting in a scenario in which the dust experiences the gas not as a flow but as a bombardment of individual gas molecules. When the size of the dust particle exceeds the mean free path of the gas molecule, the dust feels the gas as a fluid, and it is said that the dust experiences a Stokes drag. A spherical dust particle with radius s, moving at relative velocity v_{rel} to the gas, experiences a drag force given by

$$\vec{F}_D = -\frac{C_D}{2}\pi s^2 \rho_{gas} v_{rel} \vec{v}_{rel}, \tag{1.18}$$

where ρ_{gas} is the gas density. C_D is a dimensionless coefficient which describes how aerodynamic the particle is, and it is usually called the drag coefficient. In the Epstein regime, the drag coefficient is

$$C_D^{Epstein} = \frac{8\bar{v}_{th}}{3v_{rel}}, \tag{1.19}$$

where $\bar{v}_{th} = c_s\sqrt{8/\pi}$ is the gas mean thermal velocity. As shown by Weidenschilling (1977), in the Stokes drag regime the drag coefficient takes the form

$$C_D \simeq \begin{cases} 24Re^{-1}, & \text{for } Re < 1, \\ 24Re^{-0.6}, & \text{for } 1 < Re < 800, \\ 0.44, & \text{for } Re > 800, \end{cases} \tag{1.20}$$

where

$$Re = \frac{2sv_{rel}}{\nu_m}, \tag{1.21}$$

is the Reynolds numbers, with ν_m as the gas molecular viscosity. The transition between Epstein and Stokes drag regime can be expressed in terms of the Knudsen number $Kn = \lambda_{mfp}/s$: if $Kn \geq 4/9$ the dust falls in the Epstein Regime. Thus, the dust transition size is $s = 9\lambda_{mfp}/4$.

The coupling between a dust particle of mass m and the gas component of the disk can be quantified by introducing the friction time scale

$$t_{fric} = \frac{mv_{rel}}{|F_D|}, \tag{1.22}$$

which is a measure of the time that takes for the drag to significantly modify the relative velocity v_{rel} between the dust particle and the gas component of the disk. Nevertheless, it is common and useful to introduce the Stokes number St, which is a dimensionless version of the friction time. The Stokes number relates the stopping time and the orbital timescale and is given by

$$St = t_{fric}\Omega_k, \tag{1.23}$$

with Ω_k the local Keplerian angular velocity. Two particles with the same Stokes number behave aerodynamically in the same way, even if they differ in composition, structure, shape, or mass. Particles with very small Stokes numbers (i.e., $St << 1$) are considered tightly coupled to the gas, while particles with very large Stokes numbers (i.e., $St >> 1$) are considered decoupled from the gas.

1.3.1 Radial drift

The radial dynamics of the dust component in a protoplanetary disk is a crucial element in the evolution of protoplanetary disk and planet formation theories. In particular, as early as the 1970s, Whipple (1972) and Weidenschilling (1977) showed that dust particles migrate toward the star due to the drag force exerted by the gas as a result of its sub-Keplerian motion, a mechanism known as radial drift. Small dust particles, strongly coupled aerodynamically to the gas, move at the sub-Keplerian gas azimuthal velocity. However, not being supported by a pressure gradient, as is the case for the gas, the dust particles spiral inward toward the star at their radial terminal velocity. Large dust particles or bodies, poorly coupled to the gas, experience a headwind effect while moving through the gas due to the difference in velocity with respect to the gas, leading to the removal of their angular momentum, resulting in inward drift. Nakagawa et al. (1986) derived both dust and gas azimuthal and radial terminal velocity components. In particular, the dust radial terminal velocity is given by:

$$v_{dust,r} = -\frac{2}{St + St^{-1}(1-\epsilon)^2}\eta v_k, \tag{1.24}$$

with $\epsilon = \rho_{gas}/\rho_{dust}$ the volumetric dust-to-gas ratio, $v_k = r\Omega_k$ the local Keplerian velocity, and η the parameter which defines the sub-Keplerity of the gas. Nevertheless, the radial drift of solids in protoplanetary disks is predicted to be excessively efficient (Takeuchi & Lin 2002, 2005), leading to challenges for both protoplanetary disk and planetary evolution theories. As discussed in Section 2.3, the presence of substructures in protoplanetary disks, particularly local maxima in the pressure profile, can mitigate and address the radial drift problem.

1.3.2 Dust growth

To gain a comprehensive understanding of dust evolution in protoplanetary disks, it is essential not only to study dust transport processes but also to investigate dust collisional evolution. Three main ingredients define dust collisional evolution in protoplanetary disks: collision rates, collision velocities, and a collisional model (i.e., the outcome of a collision). However, studying dust collisional evolution is far from trivial, and it primarily relies on laboratory or numerical experiments, rather than observations or theoretical calculations, to determine the outcome of particle collisions as a function of particle composition, size, and relative velocity (see Blum & Wurm 2008 and Blum 2018 for a review of laboratory experiments, and Wada et al. 2009 and Seizinger & Kley 2013 for numerical experiments). Indeed, some of the key information shaping dust collision outcomes cannot be accessed through observations and remains unknown. For example, particle chemical composition (e.g., silicates, water ice) and their internal structure (e.g., aggregates or solid particles) are still uncertain, and their impact on the final result of collisions can only be studied through laboratory or numerical experiments. In the protoplanetary disk field, it is common practice to assume a model for the composition and structure of dust particles, with their behavior defined by results from laboratory or numerical experiments. Given a model for dust structure and composition, it is possible to run simulations and determine whether the observed properties of the disk can be reproduced by the theoretical models, thereby constraining and validating the assumed dust model. However, dust particles produced in laboratories or simulated numerically may not accurately represent the dust particles present in protoplanetary disks, due to the incomplete knowledge of their true characteristics and properties.

The outcome of a collision between two dust particles can be classified into three categories: growth-positive collision (e.g. sticking, Teiser & Wurm 2009), growth-neutral collision (e.g. bouncing, Zsom et al. 2010), and growth-negative collision (e.g. fragmentation,erosion; Birnstiel et al. 2010a; Krijt et al. 2015). A critical collision velocity defining the boundary between growth-positive to growth-negative collision has been defined by Wada et al. (2013) as

$$v_{crit} = C \left(\frac{s_0}{0.1 \mu m} \right)^{-5/6}, \tag{1.25}$$

with $C = 8\ m\ s^{-1}$ for silicates and $C = 80\ m\ s^{-1}$ for water ice particles. However, recent laboratory experiments conducted by Musiolik & Wurm (2019) investigated the temperature dependence of the constant C, showing that the enhanced stickiness of ice particles, due to their high surface energies, may decrease at low temperatures, leading to a critical collision velocity similar to that of silicates.

Among the different collisional outcomes, observations suggest that fragmentation is highly efficient in protoplanetary disks, as they are rich in small dust particles (Williams & Cieza 2011). Along with radial drift, fragmentation represents a key growth-limiting mechanism for dust particles. Indeed, dust collision speeds increase with particle size, meaning that as particles grow (and their size increases), they tend to experience growth-negative (or growth-neutral) collisional outcomes. Therefore, it is possible to define a maximum particle size above which growth will cease due to the negative outcomes of the collisions they experience. Denoting with v_{frag} the fragmentation threshold velocity, as shown by Birnstiel et al. (2009), the Stokes number for the turbulent fragmentation barrier reads

$$St_{frag} = \frac{1}{3} \frac{v_{frag}^2}{\alpha c_s^2}, \tag{1.26}$$

where α is the Shakura-Sunyaev α parameter. The maximum particle size for a fragmentation-limited growth is then given by

$$s_{frag} = \frac{2\Sigma_{gas}}{3\pi\rho_s\alpha} \frac{v_{frag}^2}{c_s^2}, \tag{1.27}$$

with ρ_s denoting the density of the dust particle. Both laboratory experiments (e.g., Blum & Wurm 2008) and theoretical models (e.g., Stewart & Leinhardt 2009) measured a v_{frag} threshold velocity around $1 m\ s^{-1}$ for silicate dust grains. The higher surface energy of icy particles can increase the fragmentation threshold velocity up to one order of magnitude compared to silicates (Wada et al. 2009,Gundlach et al. 2011).

A further fragmentation growth barrier may be induced by the radial drift experienced by dust particles. Indeed, if the disk is in a low turbulence regime (i.e., α is small), the radial drift velocity, which also depends on particle size (eq. 1.24), may become the dominant velocity contribution to dust collisional outcomes, defining what is typically referred to as a drift-induced fragmentation barrier. The Stokes number associated with the drift-induced fragmentation barrier computed by Birnstiel et al. (2012) reads

$$St_{df} = \frac{2v_{frag}v_k}{\gamma c_s^2}, \tag{1.28}$$

where $\gamma = |\partial lnP/\partial lnr|$ is the magnitude of the logarithmic pressure gradient.

Both fragmentation and drift-induced fragmentation barriers limit or make particle growth inefficient; therefore, they are, in all respects, growth barriers. Another barrier due to dust radial drift is the radial drift barrier introduced by Birnstiel et al. (2012). The latter does not directly limit dust growth, but it can limit its maximum size. When the particle drift timescale is shorter than its growth timescale, the particle will drift faster than it grows. The Stokes number and the particle size limit in the radial drift barrier presented by Birnstiel et al. (2012) are given by

$$St_{drift} = \frac{\epsilon}{\gamma}\left(\frac{h_g}{r}\right)^{-2}, \tag{1.29}$$

$$s_{drift} = \frac{2\Sigma_{dust}}{\pi\rho_s\gamma}\left(\frac{h_g}{r}\right)^{-2}, \tag{1.30}$$

where $\epsilon = \rho_{dust}/\rho_{gas}$ is the dust to gas ratio and $h_g = c_s/\Omega_k$ is the gas scale height. Protoplanetary disks can thus be classified into two different regimes: a drift-limited regime and a fragmentation-limited regime. Birnstiel et al. (2012) showed that outer regions of the disk are usually in the drift-limited regime, while inner regions (i.e., within a few au) are typically in the fragmentation-limited regime. The concepts of fragmentation-limited and drift-limited regimes will be further discussed in Chapter 3, outlying their impact in shaping the disk dust size distribution.

1.4 High-resolution observations and large sample surveys

Although the study of protoplanetary disks had already been well underway in the previous century, it wasn't until 2015, with the iconic image of HL Tau (ALMA Partnership et al. 2015), obtained via the Atacama Large Millimeter/Sub-Millimeter Array (ALMA), that the first direct image of a protoplanetary disk was captured. This image not only marked the first long-baseline observation of a protoplanetary disk but also revealed, for the first time, the presence of substructures within protoplanetary disks (a more in-depth discussion of this topic is provided in the following Chapter 2). The field of protoplanetary disks has been significantly revolutionized in recent years thanks to advancements in observational capabilities (e.g., new generations of infrared and high-contrast optical instruments) and, in particular, the advent of ALMA. ALMA has significantly expanded our understanding of protoplanetary disks and, by extension, of planet formation, by providing high-resolution observations with an angular resolution as good as 0.025 arcseconds. The enhanced high-resolution offered by ALMA, which translates to an observational spatial resolution of $\sim 1au$ for the closest disks (in the pre-ALMA era, the minimum available spatial resolution was around $15-20au$, e.g. Andrews et al. 2016), has revealed disk substructures and broadened the knowledge of protoplanetary disks in multiple directions. As an example:

- high-resolution observations of the disk around HD163296 (Teague et al. 2018) enabled the measurement of gas orbital velocity with a meter per second accuracy, revealing that the velocity perturbations might be caused by the presence of three Jupiter mass planets (Teague et al. 2019),

- high-resolution observations deepened the understanding of turbulence strength in protoplanetary disks, the surprisingly low upper limits observed (Teague et al. 2016; Flaherty et al. 2017, 2018), have highlighted the potential importance of other drivers of disk evolution, such as disk winds.

Although high-resolution observations allow individual disks to be studied and characterized in great detail, they tend to be biased toward the brightest and largest disks. However, ALMA has also been revolutionary in enabling large samples of lower-resolution observations. These large sample surveys have provided data on hundreds of disks across entire star-forming regions (e.g., see Manara et al. 2023, for a recent review). Large sample surveys have uncovered the existence of correlations between several disk-star observables and the distribution of various key disk parameters.

- Studies of the cumulative disk mass distributions for the star-forming regions of Taurus (Andrews et al. 2013), Lupus (Ansdell et al. 2016), Upper Scorpius (Barenfeld et al. 2016), Chamaeleon I (Pascucci et al. 2016), σ Orionis (Ansdell et al. 2018), and some disks at earlier stages (Class 0/I) in Perseus (Tychoniec et al. 2018). show that the mass decreases over time as the youngest star forming regions (Perseus, Lupus) contain the largest amount of dust (e.g., see Figure 2 in Miotello et al. 2023). Observations thus suggest that a significant fraction of the initial dust reservoir in the disk must be rapidly processed during its evolution, for example through the formation of planetesimals and/or lost via radial drift.

- A correlation between the stellar accretion rate $\dot{M}_{acc}$ and disk dust mass M_{dust} was found by Manara et al. (2016) (see Figure 1.1).

- As shown by Pascucci et al. (2016), disk dust mass M_{dust} seems to be correlated with the mass of the hosting star $M_\star$ by a steeper than linear relation (i.e. $M_{dust} \propto M_\star^{1.3-1.9}$) which steepens with the age of the star-forming region. Nevertheless, the observed correlation is flatter for transition disks (e.g., see Pinilla et al. 2020, and Figure 1.2).

- The pre-ALMA study by Tripathi et al. (2017) already revealed a size-luminosity relation for disks in the Taurus star-forming region. Later, this relation was also observed by Andrews et al. (2018b) for disks in the Lupus region observed with ALMA (Figure 1.3). Later, Hendler et al. (2020) expanded this study to star-forming regions with ages ranging from $1 Myr$ to $10 Myr$ (Figure 1.4), confirming the size-luminosity relation for these regions and showing a flattening of the relation for older regions (e.g. Upper Sco). This result may be explained, as for the cumulative disk mass distribution evolution, by the formation of planetesimal and/or radial drift.

- Spectral index distribution studies by Tazzari et al. (2021a) and Tazzari et al. (2021b) provided important information on protoplanetary disks. In particular, as shown in Tazzari et al. (2021b), the integrated spectral index for disks belonging to Taurus, Ophiucus, and Lupus star-forming regions are relatively small (~ 2.3) (see also Figure 1.5). The study of the reproducibility of these observed distributions is the core of the work presented in Chapter 3, which showed the necessity of the presence of substructures to reproduce the observed spectral index distributions.

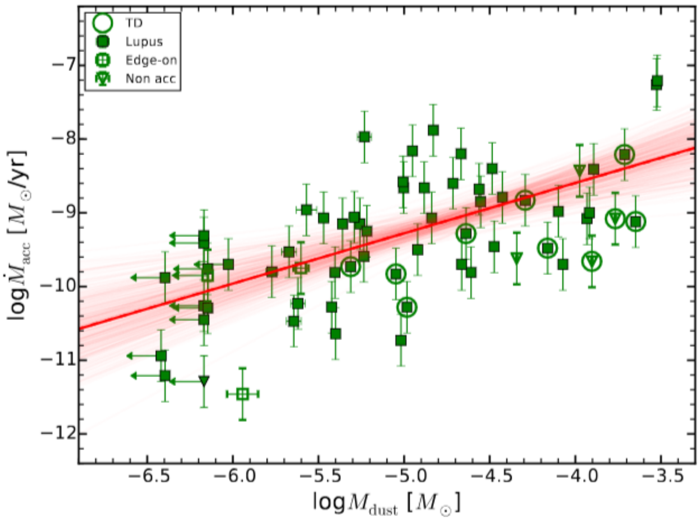

Figure 1.1: correlation between the stellar accretion rate $\dot{M}_{acc}$ and disk dust mass M_{dust} found by Manara et al. (2016). (image credit: Manara et al. 2016)

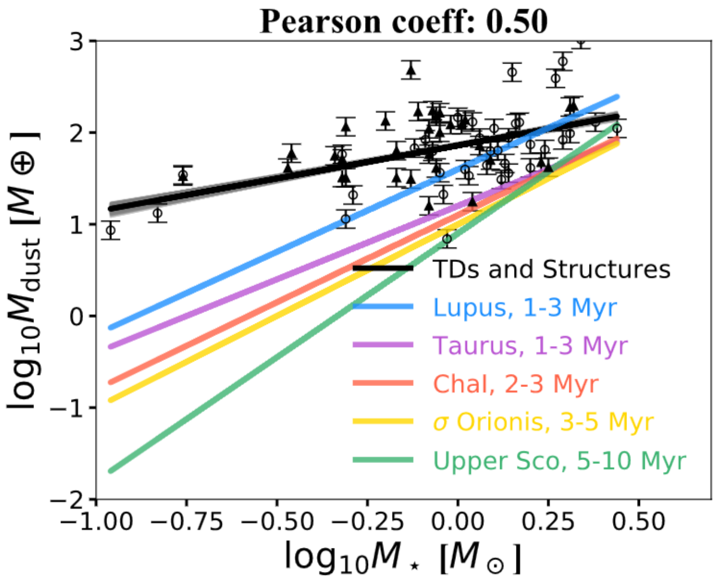

Figure 1.2: Disk dust mass M_{dust} vs hosting star mass $M_\star$ for disks belonging to different star-forming regions (Pascucci et al. 2016; Ansdell et al. 2017), for resolved cavities or transition disks (circles) and disks with structures (triangles). (image credit: Pinilla et al. 2020)

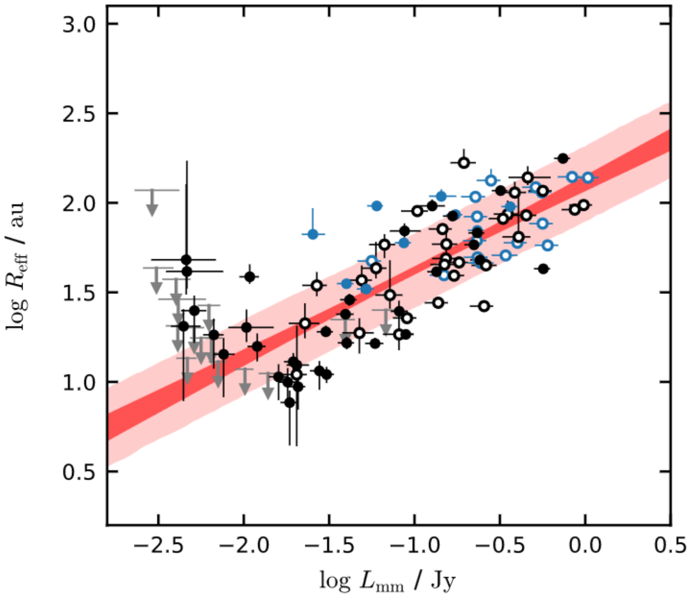

Figure 1.3: Size luminosity relation observed for the Lupus star-forming region by Andrews et al. (2018b). Image credit: Andrews et al. (2018b) (reproduced by permission of the AAS).

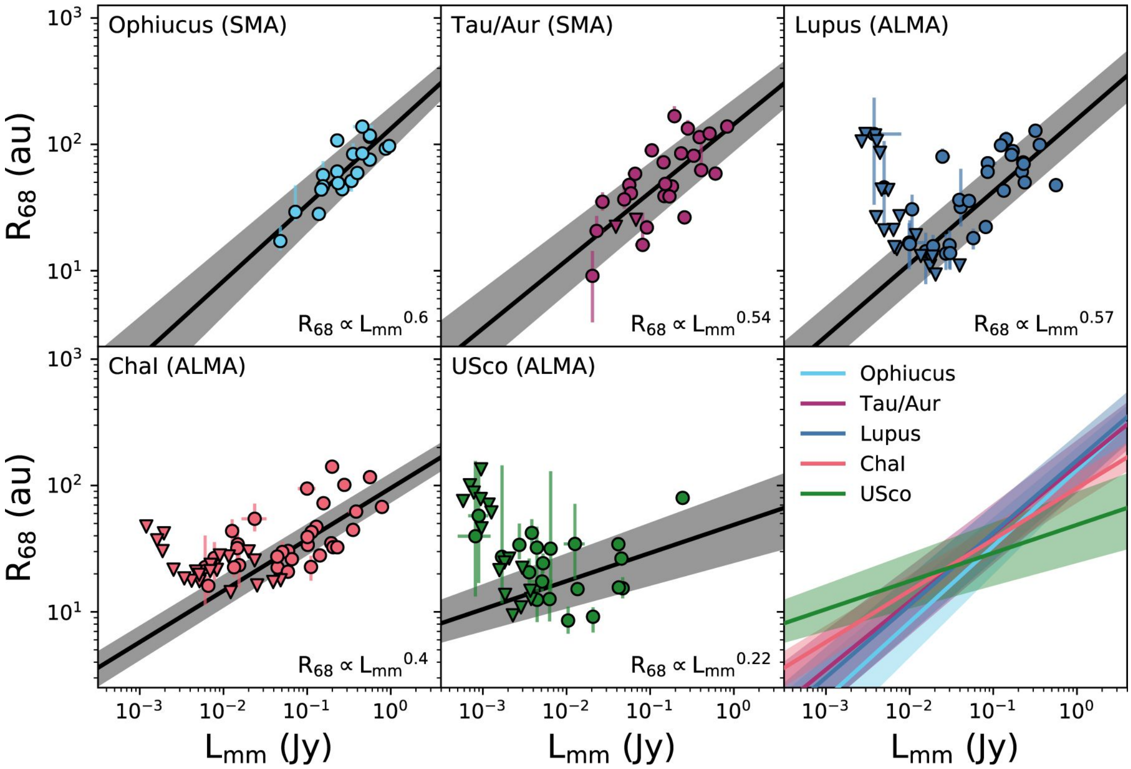

Figure 1.4: Size luminosity relation observed for different star-forming regions by Hendler et al. (2020). Image credit: Hendler et al. (2020) (reproduced by permission of the AAS).

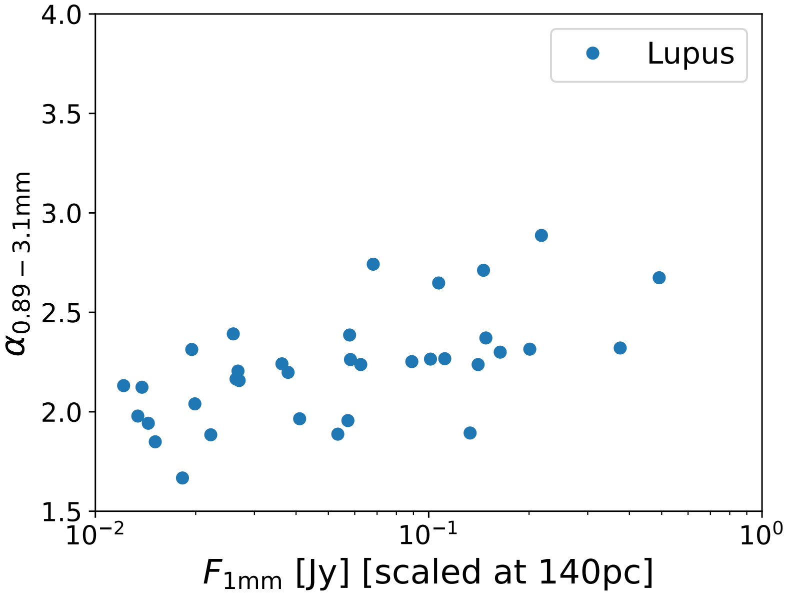

Figure 1.5: Spectral index between $0.89mm$ and $3mm$ as a function of integrated flux at $1mm$ (F_{1mm}) for disks in Lupus region after Tazzari et al. (2021b).

1.4.1 Observables: mass and size of protoplanetary disks

Before introducing the concept of disk population synthesis, which forms the core of the studies presented in this thesis, it is useful to outline the current state of the art in the observation and estimation of key disk observables, such as disk mass and size, for both the dust and gas components. For a recent, in-depth review of the measurements and implications of fundamental disk properties, see Miotello et al. (2023). A summary of the main findings from their review is provided in the following sections.

Disk dust mass

Although the contribution to the total disk mass is dominated by the gaseous component, estimating the dust disk mass remains crucial for understanding and developing protoplanetary disk evolution theories and, as well, for planetary formation theories. This is because it provides an estimate of the mass reservoir available for the formation of terrestrial planets and the cores of gas giants. Disk dust mass can be estimated through the observation of the continuum flux emitted by protoplanetary disks; however, this estimate relies on strong assumptions and theoretical models. An estimate of the dust mass M_{dust} of a protoplanetary disk can be obtained starting from the intensity I_ν of a plane-parallel layer with homogeneous temperature and opacity

$$I_\nu = B_\nu(T_{dust})(1 - e^{-\tau_\nu}), \tag{1.31}$$

where $B_\nu(T_{dust})$ denotes the Planck function at the frequency ν and for the dust temperature T_{dust}. τ_ν is the optical depth. In the optically thick limit (i.e. $\tau_\nu >> 1$) eq. 1.31 reduces to $I_\nu = B_\nu(T_{dust})$, thus T_{dust} can be evaluated from the observed intensity I_ν. In the optically thin limit (i.e. $\tau_\nu << 1$), eq. 1.31 reduces to

$$I_\nu = B_\nu(T_{dust})\tau_\nu = B_\nu(T_{dust})\Sigma_{dust}k_{abs}, \tag{1.32}$$

where k_{abs} is the dust absorption opacity. Thus, in the optically thin limit, knowledge of the dust temperature and opacity enables the calculation of the surface density and, consequently, the estimation of the dust disk mass by integrating Σ_{dust}. However, the challenge arises from the fact that the correct temperature profile and opacity of a protoplanetary disk are generally unknown. Therefore, to estimate the dust surface density (and M_{dust}) the standard approach is to assume a temperature profile and a model for the opacity. As shown by Carrasco-González et al. (2019), the problem can be solved by constraining all the individual parameters, provided that sufficient wavelength coverage is available. However, such a scenario is not yet common; therefore, the traditional approach for estimating the dust mass of the disk is to assume the disk is in the optically thin limit and to adopt an average temperature $\bar{T}_{dust}$ and opacity $\bar{k}$ for the disk. The total flux F_ν emitted by the disk can then be easily calculated as

$$F_\nu = \frac{1}{d^2}\int 2\pi r I_\nu(r)dr = \frac{1}{d^2}B_\nu(\bar{T}_{dust})\bar{k}\int 2\pi r\Sigma_{dust}(r)dr = \frac{B_\nu(\bar{T}_{dust})\bar{k}}{d^2}M_{dust}, \tag{1.33}$$

with d denoting the distance to the emitting source. Thus, the observed total flux can be used to get a rough estimate of M_{dust}. Despite the approximations underlying this method, the flux-to-mass conversion remains a widely adopted approach for estimating dust disk mass. An insight into the historical roots of this method can be found in Hildebrand (1983) and Beckwith et al. (1986, 1990). One of the main sources of uncertainty, and a quantity still largely unknown and debated today is the disk opacity, which ultimately depends on the dust grain structure (porosity and fractal dimension), their abundances, and mineralogy. A collection of opacity models has emerged in recent years (Zubko et al. 1996; Ricci et al. 2010b; Woitke et al. 2016; Birnstiel et al. 2018; Rosotti et al. 2019a). Recent studies, however, have begun questioning the optically thin assumption adopted in the flux-to-mass conversion method. Surveys such as DSHARP (Andrews et al. 2018a; Huang et al. 2018) and Long et al. (2018) have shown that optically thick substructures are ubiquitous in bright disks. As discussed by Tazzari et al. (2021a), this observational warning might indicate that a significant fraction of disk emission may originate from optically thick regions, potentially leading to an underestimation of M_{disk}. Furthermore, Tripathi et al. (2017) and Andrews et al. (2018a) predict that optically thick emission covering 30% of the disk area is necessary to explain the observed scaling of disk luminosity with disk area

Disk gas mass

Gas constitutes the primary contribution to the total mass of a protoplanetary disk, thus playing a fundamental role in theories of star, disk, and planetary formation. However, similar to dust mass, gas mass remains a challenging property to estimate (e.g., see Bergin & Williams 2017). Molecular hydrogen (H_2) is the predominant gaseous species in protoplanetary disks, making it theoretically an ideal tracer for estimating the disk's gas mass M_{gas}. However, in cold environments, such as the outer regions of protoplanetary disks where the temperature drops to $20-30K$, its emission is extremely faint. In the innermost regions of the disk, where temperatures may exceed $100K$, H_2 could become relevant. Nevertheless, these regions do not provide a reliable measure of the bulk disk gas mass (Bary et al. 2008; Carmona et al. 2008; Pascucci et al. 2013). The generally adopted approach for estimating M_{gas} relies on indirect tracers. Gas mass can be estimated from the hydrogen deuteride (HD) emission, an isotopologue of H_2 that is characterized by stronger emission than H_2 (Kama et al. 2016; Trapman et al. 2017). However, as shown by Trapman et al. (2017) and Calahan et al. (2021), a thorough understanding of the vertical structure of the protoplanetary disk is essential for accurately estimating the disk's gas mass from its HD mass. Given the caveats associated with gas mass estimation from H_2 and HD, carbon monoxide (CO) and some of its isotopologues (e.g., $^{12}\mathrm{CO}, ^{13}\mathrm{CO}, \mathrm{C}^{18}\mathrm{O}$) are the most commonly used molecular tracers for estimating disk gas masses. CO and its isotopologues represent excellent tracers for several practical and theoretical reasons:

- CO is the second most abundant molecule in protoplanetary disks, with a high detectability at (sub-)mm wavelengths.

- CO is chemically stable, and its interstellar chemistry behavior is already well known and implemented in numerous physical-chemical models (e.g., Williams & Best 2014; Miotello et al. 2014).
- CO not only allows for the estimation of disk gas mass but also provides insights into general gas properties, kinematics, and the structure of protoplanetary disks. ^{12}CO is so abundant that has an optically thick emission that can be used for kinematics and disk temperature measurements.
- Simple descriptions for the CO distribution in protoplanetary disks are available (e.g., Aikawa et al. 2002), and its distribution may be linked to H_2 without requiring many assumptions about the disk's chemistry (e.g., Kamp et al. 2017).

Nevertheless, CO is depleted in disks due to various physical-chemical mechanisms. Processes such as freeze out, isotope-selective photo-dissociation, and conversion in more complex chemical species can alter the CO/H_2 ratio in the disk throughout its evolution. These processes introduce significant uncertainty regarding the CO/H_2 ratio, which complicates the estimation of disk gas mass. Having said that, ALMA has allowed for a noteworthy expansion of gas estimates for various star-forming regions (e.g., see Ansdell et al. 2016; Cieza et al. 2019; Long et al. 2019; Cazzoletti et al. 2019; Ansdell et al. 2017; Barenfeld et al. 2016; Ansdell et al. 2020). An alternative method for estimating disk gas masses has been proposed by Powell et al. (2019), suggesting a dynamical approach that exploits disk dust lines. Nevertheless, the quest for a proper estimate of the gas mass reservoir in protoplanetary disks remains an open issue.

Disk dust size

The dust size of protoplanetary disks represents another key property for the study of disks and a crucial observable for the studies presented in Chapter 3 and Chapter 4. As discussed in Tripathi et al. (2017) and Rosotti et al. (2019b), the characteristic radius $r_{\rm c}$ cannot be adopted as a size indicator for disks. Furthermore, while a physical dust radius can be defined for a specific source (Ricci et al. 2014; Testi et al. 2016), this approach does not apply to large samples. Indeed, large sample surveys typically provide the millimeter surface brightness profile, rather than the surface density profile, of the observed disks. What is typically done then is to define an empirical radius, commonly referred to as the effective disk radius r_{eff}, which represents the radius that encompasses a given fraction of the total flux produced by the disk. The two most popular choices are $R_{68\%}$ and $R_{90\%}$, which correspond to the radii enclosing 68% and 90% of the total disk flux, respectively. As shown by Sanchis et al. (2020), $R_{68\%}$ is a safer choice, as it is usually characterized by a smaller dispersion.

Disk gas size

Estimating disk gas radii is even more challenging than estimating dust radii, as molecular emission lines are faint in the outer regions of protoplanetary disks. Additionally, deep gas observations are rarer as they are more expensive. Given their relatively brighter and optically thick emission, CO emission lines, particularly ^{12}CO lines, are the most commonly used tracers for disk gas radii estimates. However, converting the ^{12}CO radius to the actual gas radius is not a trivial task. The first large sample survey that includes both dust and gas radii estimates was conducted by Ansdell et al. (2018) for the Lupus star-forming region. A general finding from recent ALMA observations of various star-forming regions is that the disk gas radius is typically larger than the disk dust radius. Several studies have been conducted to reproduce and explain the gas-to-dust radii ratio (in particular Toci et al. 2021, 2023). Although these studies have not been able to fully reproduce the observed ratio distribution or pinpoint a clear reason for the discrepancy between simulations and observations, they seem to agree that the presence of substructures may play a key role in resolving this problem.

1.5 Disk population synthesis

The advent and continuous increase in the availability of large sample surveys have opened up a new range of questions that cannot be answered by studying individual disks: what are the key mechanisms at play during the evolution of the disks that are needed to reproduce the distributions at different disk ages and the observed correlations? Which mechanisms are responsible for the transport of angular momentum in disks (viscosity or MHD winds)? What are the initial conditions of protoplanetary disks that are necessary to reproduce observations? As a result, surveys have led to the need for models that can reproduce what we observe. Disk population synthesis is a great tool for studying these questions, gaining increasing popularity in recent years (e.g, Zormpas et al. 2022; Tabone et al. 2022; Somigliana et al. 2022, 2024; Delussu et al. 2024). By simulating thousands of models of protoplanetary disks evolving over several million years, disk population synthesis allows constraining disk initial conditions and identifying key evolutionary mechanisms in protoplanetary disks by comparing the results obtained with the simulations to the large number of surveys available. In the study presented in Chapter 3 a population synthesis of the continuum emission of disks has been performed.

Disk population synthesis has proven to be a valuable tool for investigating and constraining the parameters and initial conditions of planet-forming disks. However, the population synthesis approach can be applied not only to protoplanetary disks. While it is a relatively young method in the context of disks, it is already a well-established approach in the stellar field, where it is known as stellar population synthesis (Bruzual & Charlot 2003). Another relatively recent application of the population synthesis approach, closely related to disk population synthesis, is planet population synthesis. Notable works in planet population synthesis and disk-planet population synthesis include: Mordasini et al. (2012); Mordasini (2018); Burn et al. (2022); Emsenhuber et al. (2023a,b); Weder et al. (2023).

Chapter 2

Protoplanetary Disk Substructures

This chapter explores the discovery and observation of substructures in protoplanetary disks, a breakthrough that has revolutionized our understanding of disk dynamics and planet formation. The iconic image of HL Tau (ALMA Partnership et al. 2015) (Figure 2.1), obtained through the Atacama Large Millimeter/Sub-Millimeter Array (ALMA), provided the first direct image of a protoplanetary disk, revealing, for the first time, the presence of substructures within these disks. Subsequent surveys, such as DSHARP (Andrews et al. 2018a; Huang et al. 2018) and Long et al. (2018), have shown that optically thick substructures are ubiquitous in bright disks (Figure 2.2), sparking even greater interest in understanding the physical processes that give rise to these features and their implications for disk evolution and planet formation. High-resolution observations have uncovered a variety of complex structures, including gaps, rings, arcs, and spirals, offering crucial insights while raising new questions about the physical processes occurring within these environments. Section 2.1 provides an overview of the state of the art in the morphology of observed substructures. Section 2.2 provides an overview of the various mechanisms proposed in the literature to explain the origin of substructure in protoplanetary disks, highlighting the complexities and ongoing debates surrounding the origin of these intriguing features. Finally, Section 2.3 discusses why substructures are particularly appealing from a theoretical perspective. Beyond their observational significance, substructures are often invoked to address key challenges in disk evolution and planet formation, such as the radial drift problem and planetesimal formation. They also provide potential solutions to planetary migration issues and can account for the reproduction of the observed spectral index values in protoplanetary disks.

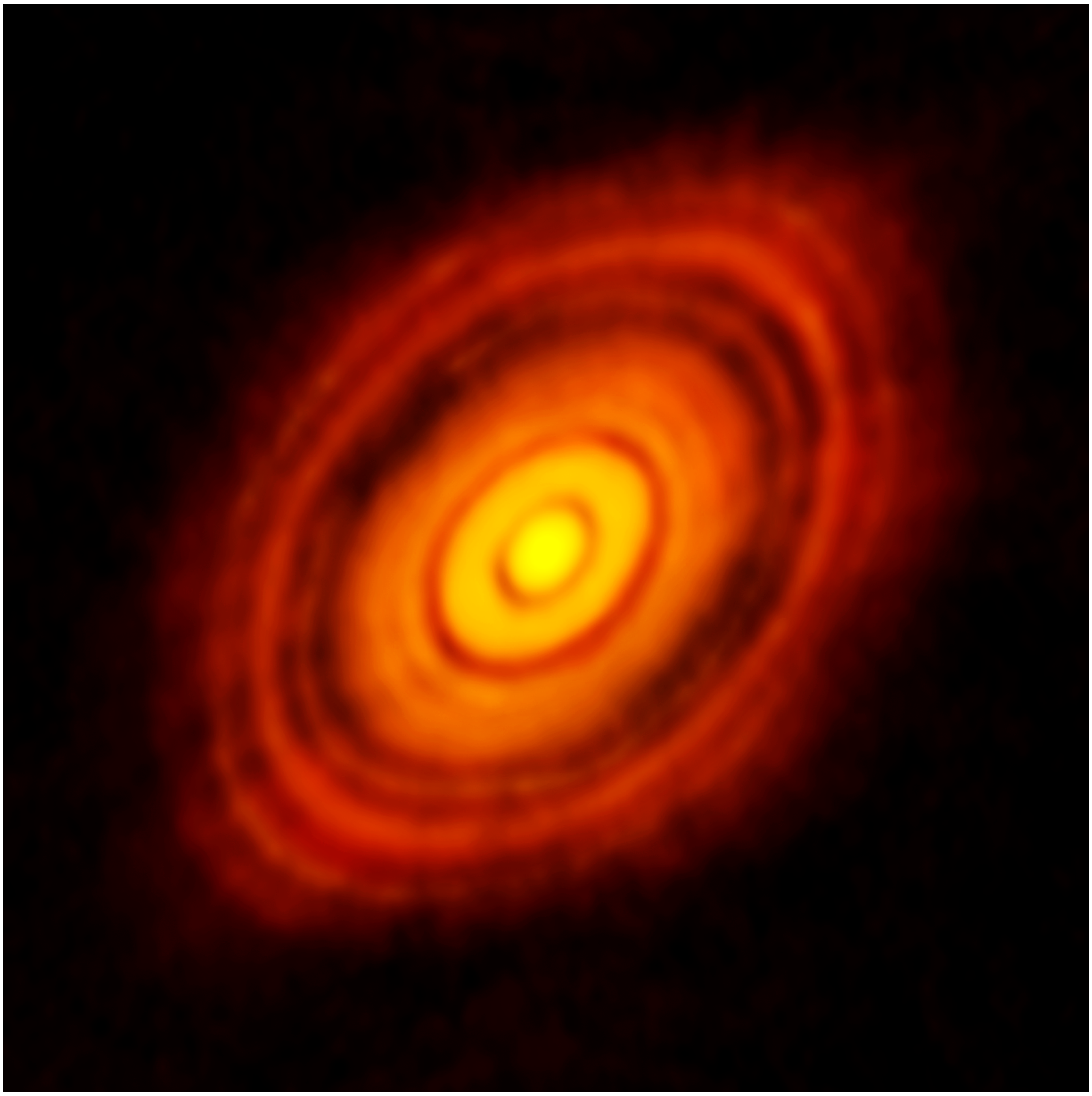

Figure 2.1: ALMA image of the protoplanetary disk observed in 2015 around HL Tauri. Image credit: ALMA (ESO/NAOJ/NRAO)

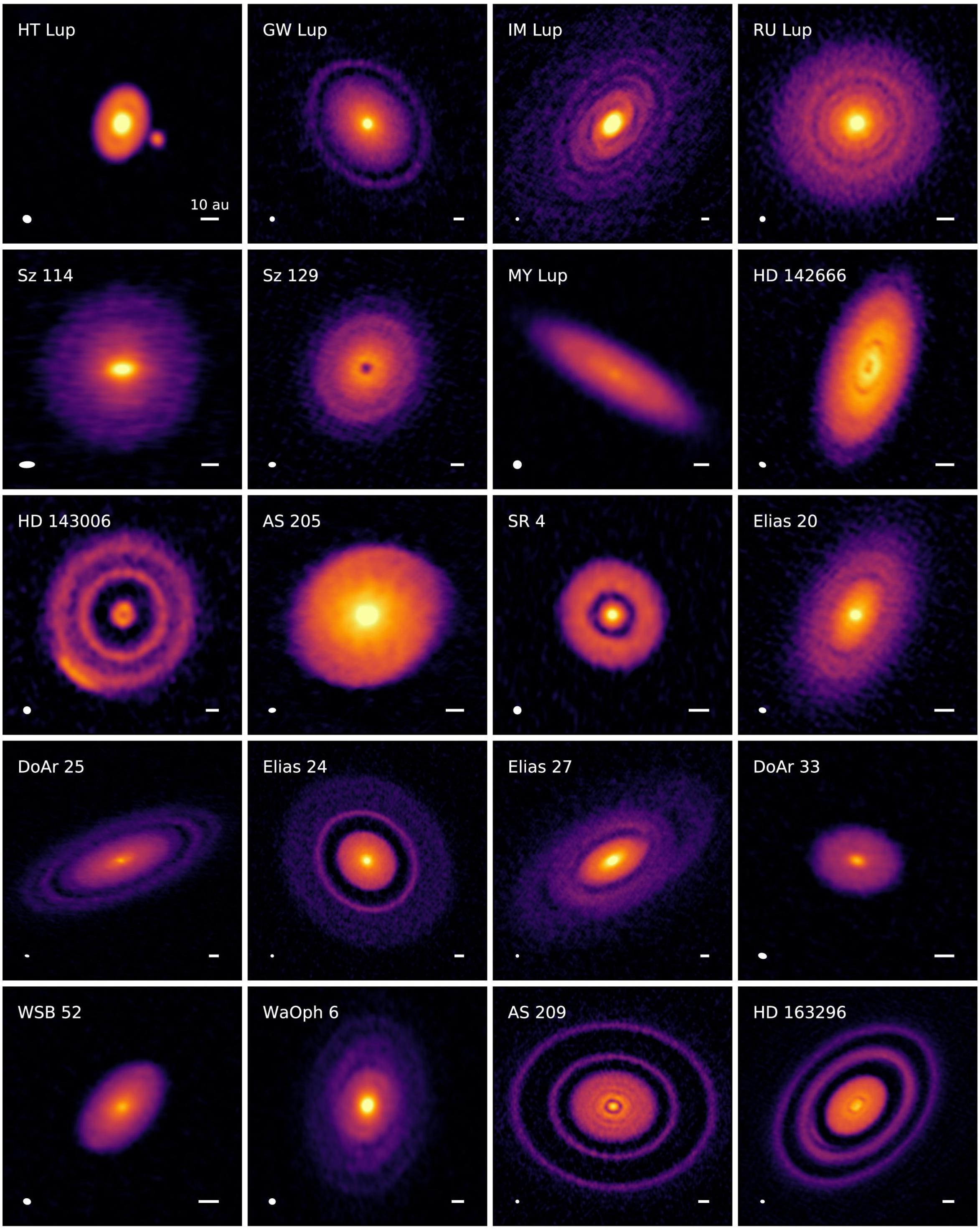

Figure 2.2: Gallery of 240 GHz (1.25 mm) continuum emission images for the disks in the DSHARP sample presented in Andrews et al. (2018a). Image credit: Andrews et al. (2018a) (reproduced by permission of the AAS).

2.1 Substructures morphology

Given the variety of observed substructures and their characteristics, and considering that disks hosting simultaneously multiple types of substructures have been observed, a morphological classification of disk substructures is not straightforward and lacks rigid boundaries. Nevertheless, a widely accepted classification categorizes them into four main types: rings, spirals, crescents, and arcs. Following the reviews by Andrews (2020) and (Bae et al. 2022), the following paragraphs summarize the key information currently available on the various morphological types of substructures observed in protoplanetary disks.

Rings

Rings are the most frequently observed type of substructure in protoplanetary disks. A ring is generally defined as a circular, azimuthally symmetric structure. Ring substructures typically do not occur alone; they are often accompanied by gaps or cavities.

- Ring-cavity: this is the standard morphology for transition disks (Espaillat et al. 2014). It is characterized by the presence of a narrow ring that encircles a depleted cavity.

- Ring-gap: ring-gap substructures represent the most commonly observed type so far, both in mm and continuum observations. The observed ring coincides with a pressure maximum, which effectively traps large particles, thereby enhancing mm observations. Ring-gap substructures are defined as concentric, axisymmetric patterns consisting of alternating intensity enhancements (rings) and depletions (gaps).

The majority of observed disks exhibit a single ring; however, high-resolution ALMA observations have enabled the detection of several multi-ring disks. Notable examples include the well-known HL Tau, which shows seven rings (ALMA Partnership et al. 2015), and TW Hya, which shows five rings (Andrews et al. 2016; Huang et al. 2018). The identification of ring multiplicity is, however, dependent on observational resolution. Future high-resolution observations may reveal the presence of additional rings and gaps in systems currently classified as single-ring. As reported in the recent review by Bae et al. (2022), rings are observed at essentially all radii distances from the host star, ranging from $3au$ as in the case of TW Hya, to $205au$ from the host star as in the case of HD 142527. Bae et al. (2022) report a maximum frequency at $20 - 50au$. Nevertheless, the lower boundary of the maximum frequency region may be influenced by the angular resolution limitations of currently available observations. A similar argument applies to the current understanding of ring widths. Observed ring widths range from a few au to $\sim 80au$, however, future high-resolution observations may reveal that the widest rings are, in fact, composed of multiple narrow rings.

Spirals

Spirals are less common than rings, with large-scale spirals primarily detected in scattered light observations. They can be characterized by modest asymmetries and a relatively open morphology (Akiyama et al. 2016) or by more intricate, tightly wrapped, and asymmetric structures (Garufi et al. 2016; Monnier et al. 2019). As reported in the recent review by Bae et al. (2022), the fraction of disks with spirals increase with the $M_{disk}/M_{\star}$ ratio; however, this trend may be due to observational bias. Nevertheless, they report no correlation between stellar or disk properties and the number of observed spirals in a disk. Regarding rings, Bae et al. (2022) show that spirals are observed across a wide radial range (from $5au$ to $> 1000au$).

Crescents

Crescents are less common than rings and spirals. They can be defined as rings exhibiting an azimuthal variation in intensity. When the azimuthal intensity contrast is close to unity, distinguishing between rings and crescents becomes challenging. Crescents have been detected, for example, in IRS 48 (van der Marel et al. 2013) and HD 142527 (Boehler et al. 2018). As reported by Bae et al. (2022), crescents appear to span a radial range from $22au$ to $185au$ from the hosting star. However, they note that, contrary to rings and spirals, crescents do not appear to cluster at a particular range.

Arcs

Arcs are a rare type of observed substructure (Pérez et al. 2016) defined as non-axisymmetric structures. They have been observed in several forms: 1) as partial rings surrounding a central cavity (van der Marel et al. 2013; Loomis et al. 2017), 2) as substructures exterior to a ring-cavity structure (van der Marel et al. 2016; Kraus et al. 2017; Boehler et al. 2018), and 3) within a gap (Isella et al. 2018; Pérez et al. 2018).

2.2 Substructure formation mechanisms

Different mechanisms have been proposed to explain the origin of substructures in protoplanetary disks, such as planets (e.g., Rice et al. 2006; Paardekooper & Mellema 2004; Pinilla et al. 2012), MHD processes (Johansen et al. 2009; Bai & Stone 2014), binary companions (e.g., Shi et al. 2012; Ragusa et al. 2017), or variations in dust material properties (e.g., Birnstiel et al. 2010a; Okuzumi et al. 2016; Pinilla et al. 2017). Nonetheless, planets or protoplanets are widely believed to be the reason behind substructures formation in the observed Class II disks. This belief is supported by kinematic evidence (Teague et al. 2018; Pinte et al. 2018; Izquierdo et al. 2022) and by directly imaged planets within the gaps, such as in the case of PDS70 (Müller et al. 2018; Keppler et al. 2018). Although the planet-induced substructures scenario is the one that has gained most popularity in recent years, it still cannot be ruled out the possibility that observed substructures may be due also to other mechanisms. Following Bae et al. (2022), the following paragraphs provide an overview of the main substructure formation mechanisms proposed in the literature.

Hydrodynamic processes

Hydrodynamic processes can lead to the formation of substructures in protoplanetary disks due to the disk's instability. These instabilities become apparent when considering inhomogeneous density structures in the disk, as well as more complex thermodynamic and/or three-dimensional treatments of the disk structure. Hydrodynamic processes that contribute to the formation of disk substructures can be classified into two categories: internally-operating processes (e.g. Rossby wave instability (RWI), vertical shear instability (VSI), convective overstability (COS), and zombie vortex instability (ZVI)) and externally-driven processes (e.g infall and photoevaporation).

- Rossby wave instability (RWI): The RWI arises from a local minimum in the radial profile of the potential vortensity (Lovelace et al. 1999; Li et al. 2000). Anticyclonic vortices are formed in a disk when a Kelvin-Helmotz instability is generated from a large velocity shear due to a perturbation to the temperature and/or gas density. RWI can develop at the edges of magneto rotational instability dead zone (MRI-dead zone) (Miranda et al. 2017; Pierens & Lin 2018), at the edge of gaps formed by planets (Lin 2014; Bae et al. 2016), at the edge of a region subject to infalling accretion (Kuznetsova et al. 2022), and between corrugated flows induced by the VSI (Richard et al. 2016).

- Vertical shear instability (VSI): it is a linear instability generated by vertical gradients in the rotational velocity of the disk (Urpin & Brandenburg 1998; Arlt & Urpin 2004; Nelson et al. 2013). Protoplanetary disks are prone to VSI formation as it is uncommon for them to be globally isothermal. Indeed, it can be demonstrated that if the disk is not globally isothermal, vertical differential rotation will inevitably develop. However, rapid gas cooling is required to sustain the differential rotation. VSI induces radially alternating upward and downward gas flows which can reach velocities on the order of $\sim 10-100ms^{-1}$ (Flock et al. 2017b, 2020). These nearly axisymmetric vertical structures are typically named corrugation modes, and they can be observed with ALMA (Barraza-Alfaro et al. 2021) using molecular line observations. Velocity perturbations produced by VSI may also lead to the formation of VSI-induced vortices.

- Convective Overstability (COS): the linear and axisymmetric convective overstability (COS) induces an exponential amplification of the epicyclic oscillations (Klahr & Hubbard 2014; Lyra 2014) leading to the formation of vortices (Lyra 2014; Raettig et al. 2021). The typically small initial vortices can merge to form larger vortices. Recent studies have shown that favorable disk regions for the COS are the midplane region located around $1-10au$ and the region above the midplane located at $\sim 10-100au$ (Malygin et al. 2017; Pfeil & Klahr 2019; Lyra & Umurhan 2019).

- Zombie vortex instability (ZVI): this hydrodynamic instability takes its name from the self-replicating nature of the vortex-forming mechanism that is induced in the disk. ZVI arises when the baroclinic critical layers of a disk are excited (Barranco & Marcus 2005; Marcus et al. 2015, 2016). These layers, which are the site of mathematical singularities, produce vortex layers, which are the birthplace of vortices. These vortices can then excite new critical layers, thus leading to a self-replicating vortex-forming mechanism. Malygin et al. (2017) have shown that ZVI is active in the innermost regions of protoplanetary disks, namely, at radial distances $\lesssim 1au$ from the host star.

- Infall: an infalling flow of material onto a protoplanetary disk can lead to substructure formation by generating vortices or spiral density waves. Vortices form when the rotational velocity of the infalling material is equal to the local Keplerian velocity. This results in the accumulation of material, creating a pressure bump that triggers a RWI near the outer edge of the infalling region, thereby leading to the formation of vortices in the disk (Bae et al. 2015; Kuznetsova et al. 2022). Spiral density waves are generated when the angular momentum of the infalling material differs from that of the local disk gas (Lesur et al. 2015; Kuznetsova et al. 2022).

- Photoevaporation: when the local photoevaporation mass-loss rate is greater than the local disk's accretion rate, inner cavities or annular gaps are formed, and a pressure bump at the inner edge of the outer disk is created. Dust particles trapped by the pressure bump can then be observed in (sub-)mm continuum observations (Gárate et al. 2021).

Magnetohydrodynamic processes

The interaction of protoplanetary disks with magnetic fields can lead to the formation of substructures. Based on the disk's ionization level, two classes of magnetohydrodynamic processes can be identified: ideal MHD (for highly ionized gas) and non-ideal MHD (for weakly ionized gas). Magnetohydrodynamic processes can be divided into zonal flows and magnetized winds, with each of these further classified into ideal and non-ideal MHD scenarios.

Zonal flows are long-lived, banded structures that may account for the observed rings in protoplanetary disks. These zonal flows can be generated through various mechanisms, both in the ideal MHD regime (e.g., ideal MHD zonal flows and spirals) and the non-ideal MHD regime (e.g., dead zones, Hall effect, and ambipolar diffusion). In general, zonal flows result from the magnetic self-organization process applied to an initially unordered flow.

- Ideal MHD Zonal flows: ring structures can form due to initially small radial variations in the Maxwell stress (Hawley 2001). The ring-forming mechanism of ideal

MHD zonal flows has been studied in both global (Jacquemin-Ide et al. 2021) and local sharing box simulations (Bai & Stone 2014).

- Spirals: magnetohydrodynamic processes can generate spirals in protoplanetary disks (Suzuki & Inutsuka 2014). In particular, given the homogeneity of the magnetohydrodynamic turbulence along the azimuthal direction, this will excite high-mode spirals. Nevertheless, the number and strength of the spirals ultimately depend on the specific properties of the magnetohydrodynamic turbulence.

- Dead zones: regions of the disk where MRI is inactive are called "dead zones". Due to the discrepancy in accretion efficiency between the MRI-active region and the dead zones, a pressure bump can form at the inner/outer edge of the dead zones, leading to a gap opening. Additionally, vortices may be induced by RWI, which arises from the density contrast between the dead zones and the MRI-active region (Lyra et al. 2015; Flock et al. 2017a). Rings or vortices induced at dead-zone inner edges are unlikely to be detectable with ALMA, as the inner edge of the dead zone is located at approximately $0.1au$ for T Tauri stars and around $1au$ for Herbig stars (Flock et al. 2016, 2019). Nevertheless, rings or vortices induced at the outer edge of a dead zone can be detected with ALMA as they can be located farther away from the star (Flock et al. 2015).

- Hall effect: large-scale axisymmetric pressure bumps can be generated by zonal flows in a Hall-dominated MRI turbulence scenario (Kunz & Lesur 2013).

- Ambipolar diffusion: although the reason behind the production of zonal flows induced by ambipolar diffusion is not yet completely clear, they have been observed in both 3D global simulations (Bai & Stone 2014) and sharing box simulations (Béthune et al. 2017).

Magnetized Winds: if a disk is crossed by net vertical magnetic fields, magnetized winds may develop (Blandford & Payne 1982), which generate a wind-driven accretion process in the disk that can lead to the formation of substructures like rings and gaps (Riols & Lesur 2019). If the local rate at which gas is lost due to wind action exceeds the rate at which it is replenished through viscous accretion, that is, if the local wind depletion timescale is shorter than the viscous accretion timescale, then a gap will be locally formed in the disk (Suzuki et al. 2016). Dust may then accumulate at the pressure maximum outside the gas gap, provided the radial drift timescale is shorter than, or at least comparable to, the wind depletion timescale (Takahashi & Muto 2018).

Gravitational instability

If a protoplanetary disk is sufficiently massive (large Σ) and/or cold (small c_s), that is its Toomre parameter $Q \equiv c_s\Omega/(\pi G\Sigma)$ is $\lesssim 1$ (Toomre 1964), its self-gravity can induce a gravitational instability regime, resulting in the formation of substructures within the disk (i.e. non-axisymmetric spirals, see for example Cossins et al. 2009) and/or impacting already existing ones. As confirmed by several simulations (Bae et al. 2014; Xu & Kunz 2021a,b), young protoplanetary disks ($< 1Myr$) are prone to gravitational instability (GI) in their outer regions ($\gtrsim 10au$), due to the significant infall of material that they experience from the surrounding molecular cloud during their early evolutionary stage. GI-driven spirals are usually a transient phenomenon, they continuously form and disappear, or they collapse and form bound objects when the cooling timescale is shorter than the orbital timescale (Gammie 2001; Cossins et al. 2009). The latter scenario is crucial in the context of planetary formation theories, as it represents a mechanism through which giant planets may form even at large distances from the star (Boss 1997), a process that is not sustainable through the classical core accretion mechanism.

Disk self-gravity can play an important role in many physical processes even for gravitationally stable (i.e. $Q > 1$) disks. As an example, ring substructures may arise due to the disk secular gravitational instability (Youdin 2011; Takahashi & Inutsuka 2014; Tominaga et al. 2019).

Disk self-gravity can also impact already existing substructures within the disk. For example, it can suppress RWI modes (Lovelace & Hohlfeld 2013) and weaken vortices (Lin & Papaloizou 2011).

Processes induced by dust particles

- Icelines: Icelines have been proposed as potential sites for substructure formation in protoplanetary disks. For example, Zhang et al. (2015) suggested that icelines could explain the origin of the gaps observed in HL Tau. The hypothesis that icelines serve as sites for substructure formation is based on the idea that radially drifting icy dust aggregates sublimate and condense when crossing the icelines, causing them to lose their ice. When ice is lost while drifting towards the star and crossing the iceline, the aggregates fragment into smaller pieces that accumulate within the icelines due to their small radial drift velocities (Ida & Guillot 2016; Hyodo et al. 2019). A steep variation of the grain size and dust surface density may be induced at the location of the icelines due to a change in the stickiness of the aggregates produced by a change in their composition once they cross the iceline (Pinilla et al. 2017; Okuzumi & Tazaki 2019). It has also been suggested (e.g., Drążkowska & Alibert 2017; Stammler et al. 2017; Hyodo et al. 2019) that dust surface density may be amplified around the location of the icelines due to condensation of the vapor released by the aggregates that have crossed the iceline, which then condenses in the regions outside the iceline. However, observations do not indicate a clear correlation between the locations of the observed substructures and the expected positions of the icelines associated with major volatile species, thereby questioning the validity of this mechanism.

- Dust-induced instabilities: dust substructures can be produced in protoplanetary disks via streaming instability (Youdin & Goodman 2005; Johansen & Youdin 2007), leading to the formation of dusty rings (Yang et al. 2017; Li et al. 2018). Furthermore, a local gas pressure maxima can form in disk regions where the dust-to-gas ratio is closer to unity, as a result of dust driving the gas dynamics (Gonzalez et al. 2017).

Tidal processes

Substructures can be induced in protoplanetary disks via tidal interactions with a bound companion (e.g., a formed/forming planet within the disk or a companion star) and/or with an unbound companion (e.g., stellar flyby).

- Excitation of spiral waves: companion-driven spirals can be generated due to the interaction between a companion (planet or star) and its hosting disk (Bae & Zhu 2018a; Miranda & Rafikov 2019). Multiple spiral arms can be excited by the companion due to constructive interference between the wave modes launched by the companion. The characteristics of the companion-driven spirals are connected to the companion mass and the temperature structure of the disk (Bae & Zhu 2018a,b).
- Disk breaking and misalignment: the disk breaking condition introduced by Zhu et al. (2019) shows that a protoplanetary disk can break into rings when a planetary or stellar companion produces a deep gap within a low viscosity disk.
- Vortex formation: RWI-induced vortices may be generated in the disk due to the RWI that can be triggered by the formation of a planetary gap in the disk.
- Stellar flybys: Stellar flybys can induce temporary spirals in a protoplanetary disk. The typically induced spiral pattern is given by a spiral connected to the passing star and a spiral generated on the opposite side to the trajectory of the passing star (Cuello et al. 2019, 2020).

Planet induced substructures: gap opening

Among the gravitational tidal interaction mechanisms that can induce the formation of substructures in a protoplanetary disk, special mention should be made of the planet-induced gap mechanism. Indeed, it is widely believed that the presence of planets or protoplanets is responsible for the substructures observed in Class II disks, primarily due to kinematic evidence (Teague et al. 2018; Pinte et al. 2018; Izquierdo et al. 2022) or the direct imaging of planets within the gaps, as seen in the case of PDS70 (Müller et al. 2018; Keppler et al. 2018). Companion-driven spirals, triggered by the presence of a planet or protoplanet, generate spiral shocks as they propagate (Goodman & Rafikov 2001; Cimerman & Rafikov 2021), leading to an exchange of angular momentum between the planet and the disk material. By transferring angular momentum to the disk material, the planet repels this material from its orbit, thereby opening an annular gap (Lin & Papaloizou 1979; Rafikov 2002). The width and depth of a planet-induced gap are influenced by the mass of the planet, the thermal structure of the disk, and local turbulent diffusion (Kley & Nelson

2012). Consequently, planet or protoplanet mass can be inferred from observations by analyzing the properties of its gap. Several analyses, both numerical (Duffell & MacFadyen 2013; Kanagawa et al. 2016; Yun et al. 2019) and analytical (Kanagawa et al. 2015a,b), have been conducted to determine a mathematical formula that describes the relationship between the properties of the formed gap, the hosting disk, and the gap-inducing planet. In the study presented in Chapter 3, the Kanagawa et al. (2016) prescription has been adopted to model the gap created by a given planet at a given position in the disk. In (Kanagawa et al. 2016), the main parameter that describes the gap formed by a planet of mass M_p located at a radial distance R_p from a host star of mass $M_\star$ within a disk described by a Shakura-Sunyaev alpha parameter α and a scale height h_p at R_p, is given by

$$K = \left(\frac{M_p}{M_\star}\right)^2 \left(\frac{h_p}{R_p}\right)^{-5} \alpha^{-1}, \tag{2.1}$$

which relates the perturbed (Σ) and unperturbed (Σ_0) surface densities via

$$\frac{\Sigma}{\Sigma_0} = \frac{1}{1 + 0.04K}, \tag{2.2}$$

which defines the depth of the induced gap. An empirical formula for the gap width Δ_{gap} has also been derived by Kanagawa et al. (2016), and reads as

$$\frac{\Delta_{gap}}{R_p} = 0.41 \left(\frac{M_p}{M_\star}\right)^{1/2} \left(\frac{h_p}{R_p}\right)^{-3/4} \alpha^{-1/4}, \tag{2.3}$$

where the width of the gap (Δ_{gap}) is simply defined as the difference between the outer (R_{out}) and inner (R_{in}) edges of the gap region.

If multiple spirals are excited by the planet/protoplanet, multiple gaps can be carved within the disk (Bae et al. 2017; Dong et al. 2017, 2018). Planetary migrations can affect the number and the location of the gaps induced within the protoplanetary disk.

2.3 The theoretical relevance of substructures in protoplanetary disks

While observations have brought substructures to the forefront by revealing their presence and, notably, their ubiquity in protoplanetary disks, theoretical interest in substructures arises primarily because they may offer a potential solution to the radial drift problem. In fact, the radial drift of solids in protoplanetary disks is predicted to be too efficient (Takeuchi & Lin 2002, 2005), posing challenges for both protoplanetary disk and planetary evolution theories. As an example, the excessively fast evolution driven by the high efficiency of the radial drift results in predictions of spectral indexes larger than the observed ones (Birnstiel et al. 2010a; Pinilla et al. 2013), a difficulty in reproducing the disk populating the high luminosity region of the size-luminosity distribution (Tripathi et al. 2017;

Rosotti et al. 2019a), and challenges planetary theories in that it makes the formation of meter-size objects and planetesimals quite challenging. The presence of substructures, and in particular of local maxima in the pressure profile of the disk, can reconcile evolutionary theories with observations and address the drift and planetesimal formation timescale problems. Specifically, solid particle migration can be mitigated, or particles can even be completely trapped at the pressure maximum (Pinilla et al. 2012, 2013). If the substructure trapping mechanism is efficient, solid particles can accumulate at the pressure maximum, thereby enhancing the local dust-to-gas ratio (Yang et al. 2017), which results in the formation of a region highly favorable for planetesimals formation (Youdin & Shu 2002; Youdin & Goodman 2005). As shown by Pinilla et al. (2012) modeling individual disks, substructure presence is needed to reproduce the observed spectral index values. An extension of this result to the broader level of a disk population synthesis is presented in Chapter 3, showing that substructures are needed to produce small values of the spectral index in the range of the observed ones and that smooth disks (i.e., disks without the presence of substructures) produce only large values of the spectral index. Substructures have also been suggested as a potential solution for the reproducibility of the observed gas-to-dust size ratio of protoplanetary disks. Toci et al. (2021) invoke the existence of unresolved or undetected substructures in the majority (or all) protoplanetary disks as the most favorable hypothesis for reconciling the simulated gas-to-dust size ratios with the observed ones.

The theoretical interest in the presence of substructures is closely linked to planet formation theories. On one hand, substructures provide a favorable environment for planet formation. In particular, the enhanced dust-to-gas ratio achievable in dust rings (Drążkowska et al. 2016) can trigger planetesimal formation through streaming instability and favor their rapid growth via pebble accretion (Lau et al. 2022). On the other hand, substructures have proven to be a key element in addressing planetary migration challenges, such as offering a solution to the difficulty of explaining Jupiter's location within solar system formation theories (Coleman & Nelson 2016; Bitsch et al. 2019; Morbidelli 2020; Andama et al. 2022). The recent work by Lau et al. (2024) investigating the formation of gas giants in the Solar system has further confirmed the difficulty in retaining planetary cores in a smooth disk scenario.

Chapter 3

Population Synthesis Models Indicate a Need for Early and Ubiquitous Disk Substructures

Luca Delussu, Tilman Birnstiel, Anna Miotello, Paola Pinilla, Giovanni Rosotti and Sean M. Andrews

This chapter was published in Astronomy & Astrophysics, 688, A81 (2024)

Abstract

Large mm surveys of star forming regions enable the study of entire populations of planet-forming disks and reveal correlations between their observable properties. The ever-increasing number of these surveys has led to a flourishing of population study, a valuable tool and approach that is spreading in ever more fields. Population studies of disks have shown that the correlation between disk size and millimeter flux could be explained either through disks with strong substructure, or alternatively by the effects of radial inward drift of growing dust particles. This study aims to constrain the parameters and initial conditions of planet-forming disks and address the question of the need for the presence of substructures in disks and, if needed, their predicted characteristics, based on the large samples of disk sizes, millimeter fluxes, and spectral indices available. We performed a population synthesis of the continuum emission of disks, exploiting a two-population model (two-pop-py), considering the influence of viscous evolution, dust growth, fragmentation, and transport varying the initial conditions of the disk and substructure to find the best match to the observed distributions. Both disks without substructure and with substructure have been examined. We obtained the simulated population distribution for the disk sizes, millimeter fluxes and spectral indices by post-processing the resulting disk profiles (surface density, maximum grain size and disk temperature). We show that the observed distributions of spectral indices, sizes, and luminosities together can be best reproduced by disks with significant substructure, namely a perturbation strong enough to be able to trap particles, and that is formed early in the evolution of the disk, that is within 0.4 Myr. Agreement is reached by relatively high initial disk masses ($10^{-2.3} M_\star \leqslant M_{disk} \leqslant 10^{-0.5} M_\star$) and moderate levels of turbulence ($10^{-3.5} \leqslant \alpha \leqslant 10^{-2.5}$). Other disk parameters play a weaker role. Only opacities with high absorption efficiency can reproduce the observed spectral indices. Disk population synthesis is a precious tool for investigating and constraining parameters and initial conditions of planet-forming disks. The generally low observed spectral indices call for significant substructure, as planets in the Saturn to few Jupiter-mass range would induce, to be present already before 0.4 Myr. Our results extend to the whole population that substructure is likely ubiquitous, so far assessed only in individual disks and implies that most "smooth" disks hide unresolved substructure.

3.1 Introduction

The advent of the Atacama Large Millimetre/Sub-Millimeter Array (ALMA) has strongly revolutionized the protoplanetary disk field. High-resolution observations have shown that most disks that have been imaged are characterized by the presence of substructures (Andrews et al. 2018a; Huang et al. 2018; Long et al. 2018). Different mechanisms have been proposed to explain the origin of substructures in protoplanetary disks, such as planets (e.g., Rice et al. 2006; Paardekooper & Mellema 2004; Pinilla et al. 2012), MHD processes (Johansen et al. 2009; Bai & Stone 2014), binary companions (e.g., Shi et al. 2012; Ragusa et al. 2017), or variations in dust material properties (e.g., Birnstiel et al. 2010a; Okuzumi et al. 2016; Pinilla et al. 2017). Nevertheless, it is widely believed that the presence of planets or protoplanets could be the reason behind the substructures observed in Class II disks, mainly due to kinematic evidence (Teague et al. 2018; Pinte et al. 2018; Izquierdo et al. 2022) or directly imaged planets within the gaps, as in the case of PDS70 (Müller et al. 2018; Keppler et al. 2018). However, there is still a need to connect the distribution of exoplanets observed to a potential planet population in protoplanetary disks.

High-resolution observations enable studying and characterizing individual disks in great detail. However, these observations tend to be biased towards the brightest and largest disks. Nevertheless, ALMA has also been revolutionary by enabling large samples of lower-resolution observations. These provided hundreds of disks in large sample surveys of entire star-forming regions (see Manara et al. 2023, for a recent review). These observations have uncovered the existence of correlations between several disk-star observables such as the disk-size-luminosity relation (Tripathi et al. 2017; Andrews et al. 2018b), $M_{\rm dust} - M_{\rm star}$(Andrews et al. 2013; Ansdell et al. 2016; Pascucci et al. 2016), $\dot{M} - M_{dust}$ (Manara et al. 2016) and the distribution of several key parameters of disks, such as the disk spectral index (Ricci et al. 2010a,b; Tazzari et al. 2021a).

Surveys have thus opened up a new range of questions that cannot be answered by studying individual disks: what are the key mechanisms at play during the evolution of the disks that are needed to reproduce the distributions at different disk ages and the observed correlations? What mechanisms are responsible for the transport of angular momentum in disks (viscosity or MHD winds)? What are the initial conditions of the protoplanetary disks that are needed to reproduce observations? Surveys have thus led to the need to find models that can reproduce what we observe. Disk population synthesis is the tool of choice to study these questions. Simulating thousands of models of protoplanetary disks evolving for several million years, disk population synthesis enables constraining disk initial conditions and identifying key evolutionary mechanisms of protoplanetary disks by comparing the results obtained from the simulations to the large amounts of surveys available.

This study represents an extension of the study performed by Zormpas et al. (2022). They explored whether smooth disks and sub-structured disks can reproduce the size-luminosity relation (SLR), performing a disk population study. In particular, they showed that smooth disks in the drift regime correctly reproduce the observed SLR (see also Rosotti et al. 2019a). However, their study has also shown that substructured disks can populate the bright part of the SLR, but they follow a different relation. Thus they state that the observed sample could be composed of a mixture of smooth and substructured disks. The performed disk population study has also exhibited the need to have a high initial disk mass and low turbulence to reproduce the observed distribution. Finally, they have shown that grain composition and porosity play a key role in the evolution of disks in the size-luminosity diagram. In particular, the opacity model from Ricci et al. (2010b) but with compact grains as in Rosotti et al. (2019a) has proved to better reproduce the SLR than the DSHARP opacities (Birnstiel et al. 2018, which is similar in composition to previously used opacities such as in Pollack et al. 1994 or D'Alessio et al. 2006). A similar indication concerning DSHARP opacities comes from the study of Stadler et al. (2022), which shows that the opacity model of Ricci et al. (2010b) leads to a better matching of the observed spectral index in contrast to DSHARP opacities.
In this study, we aim to extend the work of Zormpas et al. (2022), by exploring whether smooth and sub-structured disks can reproduce the observed spectral index distribution, and explore the required initial conditions that lead to evolved disks matching current observations. Moreover, we aim to understand whether it is possible to match both the size-luminosity and spectral index distributions at the same time and what initial disk parameters are required for that.

This paper is structured as follows: in Sect. 3.2, we describe our computational model for the evolution of the disk and introduce the analysis method used to compare to disk observations. Section 3.3 introduces the main results obtained and the comparison to the observed distributions. We first focus on reproducing the spectral index and then on the possibility of a simultaneous matching of both the spectral index and the size-luminosity distributions. Section 3.4 presents our conclusions.

3.2 Methods

The two-population model (two-pop-py) by Birnstiel et al. (2012) and Birnstiel et al. (2015) has been exploited to perform 1D simulations to describe the gas and dust evolution in the disk. Two-pop-py is a tool that is well suited for disk population studies since it captures the dust surface density evolution, the viscous evolution of the gas and the particle size with good accuracy. Being based on a set of simple equations, it allows to perform a single simulation quickly (order of seconds), making it computationally feasible to run large numbers of simulations within a reasonable amount of time. In the following we will describe the main characteristics of the two-pop-py model and the assumptions on which it is based.

3.2.1 Disk evolution

The protoplanetary gas disk is evolved according to the viscous disk evolution equation (Lüst 1952; Lynden-Bell & Pringle 1974) using the turbulent effective viscosity as parameterized in (Shakura & Sunyaev 1973),

$$\nu = \alpha_{gas} \frac{c_s^2}{\Omega_k}; \tag{3.1}$$

the dust diffusion coefficient is:

$$D \simeq \alpha_{dust} \frac{c_s^2}{\Omega_k}, \tag{3.2}$$

where α_{gas}, c_s and Ω_k denote the turbulence parameter, the sound speed and the Keplerian frequency respectively. The additional term $\frac{1}{1+\mathrm{St}^2}$, with St being the Stokes number, as derived in Youdin & Lithwick (2007) was dropped since the Stokes number is always < 1 in all the simulations that have been performed.

As in Zormpas et al. (2022), two different families of disk models have been taken into account in our study: *smooth disks* and *sub-structured disks.* A smooth disk is characterized by the absence of any gaps during its entire evolution while a sub-structured disk is a disk in which a single substructure is created during its evolution. In contrast to Zormpas et al. (2022) where substructure is inserted since the beginning of the evolution of the disk, our sub-structured disk starts as a smooth disk and during its evolution a gap is created, and thus the disk becomes sub-structured. This new approach allows investigating the effect of the time at which substructure is inserted during the evolution of the system. Substructure has been modelled as a gap due to the presence of a planet that is inserted in the disk. To mimic the presence of a planetary gap we have subdivided the α parameter into two different values: α_{gas} and α_{dust}. The presence of the planet has been modelled as a local variation of the gas viscosity, while other than in the proximity of the gap, the two parameters are taken to be identical, that is $\alpha_{gas} = \alpha_{dust}$. More information on how we model the planet's presence in the disk can be found in Sect. 3.2.3. Adopting the two-population model described in Birnstiel et al. (2012) we evolve the dust surface density assuming that the small dust is tightly coupled to the gas while the large dust particles can decouple from it and drift inward. The initial gas surface density follows the Lynden-Bell & Pringle (1974) self-similar solution,

$$\Sigma_g(r) = \Sigma_0 \left(\frac{r}{r_\mathrm{c}}\right)^{-\gamma} exp \left[- \left(\frac{r}{r_\mathrm{c}}\right)^{2-\gamma} \right], \tag{3.3}$$

where the normalization parameter $\Sigma_0 = (2-\gamma)M_{disk}/2\pi r_\mathrm{c}^2$ is set by the initial disk mass M_{disk}, r_c denotes the so-called characteristic radius of the disk and γ the viscosity exponent. For our simulations, γ has been set to 1 for the initial profiles of all the disks. This choice is mostly consistent with our choice of the viscosity (see Eq. 3.1) which deviates from $\gamma = 1$ only in the case of substructure being included and in the isothermal part of the disk. Furthermore, choosing a $\gamma \neq 1$ would relax back to the $\gamma = 1$ case in a viscous time scale. The initial dust surface density is related to the gas surface density by a constant initial dust-to-gas ratio $\Sigma_d/\Sigma_g = 0.01$.

The two-population model consists of a population of initial grain size $a_{min} = 0.1\mu m$ whose size is kept constant in time and space during the evolution and a large grain population that is allowed to increase in size with time. When Ricci et al. (2010b) opacities have been taken into account the particle bulk density has been set to a value of $\rho_s = 1.7\ g/cm^3$ as we considered the composition of Ricci et al. (2010b) but for the case of compact grains (no porosity), as in the model of Rosotti et al. (2019a). This opacity case will henceforth be referred to as *Ricci compact opacities*. For DSHARP (Birnstiel et al. 2018) opacities we set $\rho_s = 1.675\,\mathrm{g/cm^3}$ (0% porosity case) and this value decreases based on the porosity assumed for the grains. The grain composition consists of 60% water ice, 30% carbonaceous materials and 10% silicates by volume. For DIANA (Woitke et al. 2016) opacities we set $\rho_s = 2.08\,\mathrm{g/cm^3}$. For a comparison with the size-luminosity distribution observed by Andrews et al. (2018b), we computed the opacity in ALMA Band 7, more precisely at $0.89mm$, and as described in Subsect. 3.2.4 we evaluated the continuum intensity profile of the disk considering the absorption and scattering opacity contributions (see Subsect. 3.2.4). Four different grain porosity cases have been explored for the DSHARP opacity model (Birnstiel et al. 2018): 0%, 10%, 50% and 90% porosity. The bulk densities adopted for these four cases are the following: $\rho_s = 1.675\,\mathrm{g/cm^3}$, $\rho_s = 1.508\,\mathrm{g/cm^3}$, $\rho_s = 0.838\,\mathrm{g/cm^3}$ and $\rho_s = 0.168\,\mathrm{g/cm^3}$. Ricci compact opacities have been adopted as the standard case in our analysis. When another model has been adopted it will be specified. For each simulation, the disk has evolved for 3 Myr.

The 1D disk has been spatially modeled with a radial grid that ranges from 0.05 au to 2000 au, and the cells of the grid are spaced logarithmically. The main characteristics of the grid model are reported in Table 3.1.

The temperature of the disk is linked to the luminosity of the star, that is we have worked within an adaptive temperature scenario. However, both the stellar luminosity $L_\star$ and

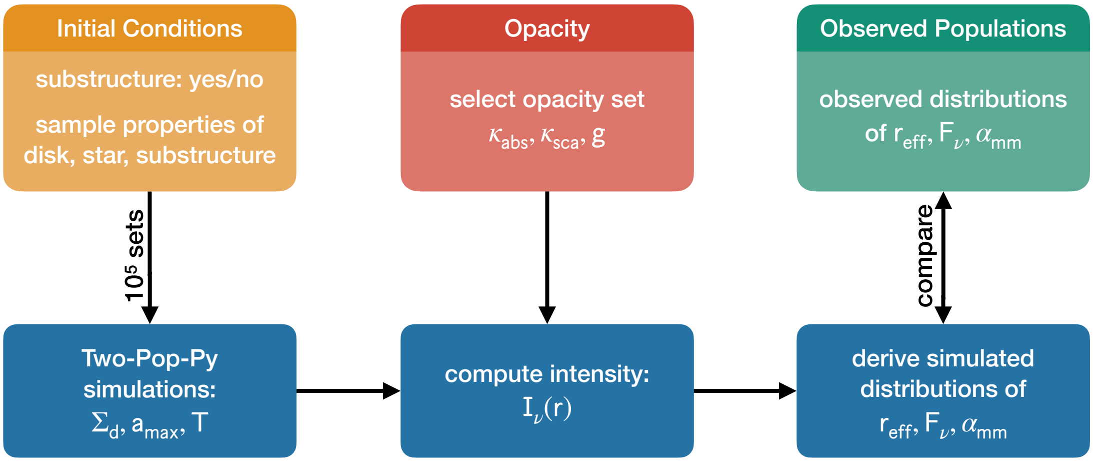

Figure 3.1: Disk population study procedure.

effective temperature T are not evolved in our simulations. In Appendix A we show a comparison to the scenario in which $L_\star$, and thus T, evolve, showing that the results are analogous to the fixed scenario.
We have adopted a passive irradiated disk temperature model; no viscous heating or other processes have been considered. In particular, we have followed the temperature profile adopted by Kenyon et al. (1996):

$$T = \left(\phi \frac{L_\star}{4\pi\sigma_{SB} r^2} + (10K)^4\right)^{1/4}, \tag{3.4}$$

where $L_\star$ is the star luminosity, σ_{SB} the Stefan-Boltzmann constant and ϕ is the flaring angle set to 0.05. The floor temperature of the disk has been set to $10K$. The star's luminosity value $L_\star$ was set starting from the star's mass value $M_\star$ exploiting Siess et al. (2000) evolutionary tracks and considering the value of $L_\star$ at an age of the star of 1Myr. $M_\star$ has been set based on the IMF of Chabrier and Kroupa (see next Sect. 3.2.2).

3.2.2 Disk Population synthesis

Disk population synthesis is based on the idea of performing a large number of simulations of the evolution of dust and gas for millions of years, to constrain disk initial conditions and identify what are the key mechanisms at play in the disk by comparing the distribution of the observable parameters obtained from the simulations with the observed ones.

Figure 3.1 explains the key idea behind our disk population study. Firstly a large set of initial parameters has been set up combining different initial values of the main parameters used to describe each disk. In particular, to map all the parameter space, the set of initial conditions adopted for each disk has been constructed randomly drawing each parameter from a probability distribution function. A total of 10^5 simulations have been performed for each population synthesis, which well map the entire relevant parameter

Table 3.1: Fixed parameters.

Parameter	Description	Value or Range
Σ_d/Σ_g	initial dust-to-gas ratio	0.01
ρ_s $[g/cm^3]$	particle bulk density (no porosity)	1.7 (Ricci opacity), 1.675 (DSHARP opacity)
γ	viscosity parameter	1
r $[au]$	grid extent	0.05-2000
n_r $[cells]$	grid resolution	400
t $[Myr]$	duration of each simulation	3

space. The main parameters that have been taken into account to describe the disk are: disk mass (M_{disk}), stellar mass ($M_\star$), disk characteristic radius (r_c), viscous parameter (α) and fragmentation velocity (v_{frag}). This choice of parameters applies to the description of all the disks (i.e., both smooth and sub-structured disks). Sub-structured disks have been characterized by three additional parameters: the mass of the planet that creates the gap (m_p), the time (t_p) and the position (r_p) at which the planet has been inserted. This set of three additional parameters applies for each planet that is inserted in the system, that is in the extra cases of double sub-structured systems (see Sect. 3.3.2), each gap has been characterized by its own set of three parameters ($m_{p,i}$, $t_{p,i}$, $r_{p,i}$). The drawing of the m_p value is performed after drawing a value of M_{disk}, to impose the further physically reasonable restriction of $m_p < M_{disk}$. In the case of multiple substructures, we applied the following constraint: $\sum_i m_{p,i} < M_{disk}$. Table 3.2 shows the range that has been adopted for each parameter.

The viscosity parameter α and the initial mass of the disk M_{disk} have been randomly drawn from a log uniform probability distribution function (PDF) to span uniformly the full range of values adopted for these two parameters. A log uniform PDF has been adopted for the disk characteristic radius r_c too, to favor smaller values of r_c to resemble the observed behavior of protoplanetary disks' sizes. The values of the stellar mass $M_\star$ have been drawn from a functional form of the IMF proposed by Maschberger (2013) which is based on the standard IMFs of Kroupa (Kroupa (2001),Kroupa (2002)) and Chabrier (Chabrier 2003).

Given the set of 10^5 initial conditions, each disk has been evolved for $3Myr$ using the two-pop-py evolutionary code. For the evolved disks obtained through two-pop-py, we have evaluated the observables parameters (Subsect. 3.2.4 and Subsect. 3.2.5). Finally, the distributions of the observable parameters obtained for the simulated disks have been compared to the observed ones.

Both observed and simulated fluxes of each disk have been scaled to a reference distance of 140pc.

Table 3.2: Disk initial parameters.

Parameter	Description	Range	PDF
α	viscosity parameter	$10^{-4} - 10^{-2}$	log uniform
M_{disk} $[M_\star]$	initial disk mass	$10^{-3} - 0.5$	log uniform
$M_\star$ $[M_\odot]$	stellar mass	$0.2 - 2.0$	IMF
r_c $[au]$	characteristic radius	$10 - 230$	log uniform
v_{frag} $[cm/s]$	fragmentation velocity	$200 - 2000$	uniform
m_p $[M_\oplus]$	planet mass	$1 - 1050$	uniform
r_p $[r_c]$	planet position	$0.05 - 1.5$	uniform
t_p $[Myr]$	planet formation time	$0.1 - 0.4$ (early formation case)	uniform
t_p $[Myr]$	planet formation time	$0.4 - 1.0$ (late formation case)	uniform

Notes. Disk initial parameters and corresponding probability distribution function (PDF) from which their value is drawn for each single simulation. The drawing of the m_p value was performed after the M_{disk} to impose the further physically reasonable restriction of $m_p < M_{disk}$. In the case of multiple substructures, we applied the following constraint: $\sum_i m_{p,i} < M_{disk}$.

3.2.3 Planetary gaps

The sub-structured disks have been produced generating a gap through the insertion of a planet during the evolution of the disk. The presence of a massive planet in the disk leads to the formation of a gap in the gas distribution, which we call substructure. To mimic the gap associated with a planet's presence in our disks, we have modified the value of the α_{gas} parameter. We took advantage of the inverse proportionality between α_{gas} and Σ_g in a steady state regime, that is $\alpha_{gas} \propto 1/\Sigma_g$. Thus, a bump in the α_{gas} profile will reflect in a gap in the Σ_g profile that reproduces the presence of a planetary gap, besides, this procedure allows keeping a viscous evolution for Σ_g. We have adopted the Kanagawa et al. (2016) prescription to model the gap created by a given planet at a given position in the disk.

The main parameter that describes the gap formed by the planet is:

$$K = \left(\frac{M_p}{M_\star}\right)^2 \left(\frac{h_p}{R_p}\right)^{-5} \alpha^{-1}. \tag{3.5}$$

The main caveat associated with the Kanagawa prescription is that it is an analytical approximation of the gap depth and width. However as described in Zormpas et al. (2022), the width of the gap is the dominant factor in the evolution of the disk, and the depth is not crucial to the evolution of the disk. The position and radial extent of the gap are what matter the most to the evolution of the disk and those are well reproduced by the prescription.

3.2.4 Observables

One of the problems when dealing with protoplanetary disks is defining their size (see Miotello et al. 2023, as a review). Indeed, as discussed in Tripathi et al. (2017) and Rosotti et al. (2019b), we cannot adopt the characteristic radius $r_{\rm c}$ as a size indicator of the disks. We have thus followed the procedure of defining an effective radius r_{eff} of the disk. The effective radius is defined as the radius that encompasses a given fraction of the total amount of flux that is produced by the disk. We have chosen to define our effective radius as the radius that encloses the 68% of the total amount of flux produced by the disk, following Tripathi et al. (2017).
The Miyake & Nakagawa (1993) scattering solution of the radiative transfer equation has been adopted to evaluate the mean intensity J_ν:

$$\frac{J_\nu(\tau_\nu)}{B_\nu(T(r))} = 1 - b\left(e^{-\sqrt{3\epsilon_\nu^{eff}}(\frac{1}{2}\Delta\tau - \tau_\nu)} + e^{-\sqrt{3\epsilon_\nu^{eff}}(\frac{1}{2}\Delta\tau + \tau_\nu)}\right), \tag{3.6}$$

where B_ν is the Planck function and

$$b = \left[\left(1 - \sqrt{\epsilon_\nu^{eff}}\right) e^{-\sqrt{3\epsilon_\nu^{eff}}\Delta\tau} + 1 + \sqrt{\epsilon_\nu^{eff}}\right]^{-1}, \tag{3.7}$$

and the optical depth τ_ν is given by

$$\tau_\nu = \left(k_\nu^{abs} + k_\nu^{sca,eff}\right)\Sigma_d, \tag{3.8}$$

where

$$k_\nu^{sca,eff} = (1 - g_\nu)\, k_\nu^{sca} \tag{3.9}$$

is the effective scattering opacity and k_ν^{abs} is the dust absorption opacity, obtained from the Ricci compact (Rosotti et al. 2019a), DSHARP (Birnstiel et al. 2018) or DIANA (Woitke et al. 2016) opacities. g_ν is the forward scattering parameter. The introduction of the effective scattering opacity $k_\nu^{sca,eff}$ reduces the impact of the underlying approximation that scattering is isotropic. The effective absorption probability ϵ_ν^{eff} is given by:

$$\epsilon_\nu^{eff} = \frac{k_\nu^{abs}}{k_\nu^{abs} + k_\nu^{sca,eff}}, \tag{3.10}$$

and $\Delta\tau$ is

$$\Delta\tau = \Sigma_d k_\nu^{tot} \Delta z. \tag{3.11}$$

The intensity I_ν^{out} has been evaluated following the modified Eddington-Barbier approximation as adopted by Zormpas et al. (2022) following Birnstiel et al. (2018):

$$I_\nu^{out} \simeq \left(1 - e^{-\Delta\tau/\mu}\right) S_\nu\left(\frac{\Delta\tau}{2\mu} - \frac{2}{3}\right), \tag{3.12}$$

with $\mu = cos\theta$ and the source function $S_\nu(\tau_\nu)$ given by:

$$S_\nu(\tau_\nu) = \epsilon_\nu^{eff} B_\nu(T_d) + (1 - \epsilon_\nu^{eff}) J_\nu(\tau_\nu). \tag{3.13}$$

The role of scattering vanishes for small optical depth ($\Delta\tau << 1$). Indeed, the assumption that only the absorption opacity matters, is appropriate for optically thin dust layers of protoplanetary disks. However, one of the reasons behind the choice of including the scattering opacity in our treatment is that DSHARP survey (Birnstiel et al. 2018) revealed that optical depth is not small in protoplanetary disks. Moreover, (Kataoka et al. 2015) pointed out the importance of scattering in the (sub-)millimeter polarization of protoplanetary disks.

A particle size distribution, evolved by two-pop-py, is needed to compute the optical properties of the dust. We assumed a population of grains described by a power-law size distribution, $n(a) \propto a^{-q}$, with q=2.5 for $a_{min} \leqslant a \leqslant a_{max}$. The grain size at each radius is set by the lower value among the maximum grain size possible in the fragmentation- or drift-limited regimes, As described in Birnstiel et al. (2012), disks in the drift-limited regime are better described by $q = 2.5$, while disks in the fragmentation-limited regime by $q = 3.5$. Following the same reasoning reported in Zormpas et al. (2022), we adopt a value of $q = 2.5$. Indeed smooth disks are mostly drift-limited and if there is a fragmentation-limited region in the disk, it resides in the inner part of the disk, thus the luminosity of the disk will still mainly depend on the drift region as it resides in the external part of the disk where there is the bulk of the disk mass. The fragmentation-limited region can be located further out in sub-structured disks in correspondence to the ring, but the difference between the choice of the two q exponents is reduced by the fact that the rings are mostly optically thick.

3.2.5 Spectral index

We define the spectral index as the slope of the (sub-)mm SED of the dust emission, that is:

$$\alpha_{mm} = \frac{dlogF_\nu}{dlog\nu}, \tag{3.14}$$

where F_ν is the *disk-integrated flux* at a given frequency ν[1], thus α_{mm} is the *disk-integrated spectral index.* Since we usually deal with frequencies that are very close to each other we can write:

$$\alpha_{mm} = \frac{log(F_{\nu,2}/F_{\nu,1})}{log(\nu_2/\nu_1)}. \tag{3.15}$$

If we assume that the radiation is emitted in a Rayleigh-Jeans regime and that the emission is optically thin we can further relate, in first approximation, the spectral index to the dust opacity power law slope β ($k_\nu \propto \nu^\beta$):

$$\alpha_{mm} \approx \beta + 2. \tag{3.16}$$

The spectral index represents a key parameter for the characterization of protoplanetary disks because it carries information about the maximum size of the particles that are

---

[1] All fluxes will be given in frequency space (F_ν, typically in units of Jy), even though the subscript is stating the corresponding wavelength instead of the frequency.

present in the disk (Miyake & Nakagawa (1993),Natta et al. (2004),Draine (2006)).

Starting from the post-processed values of the fluxes that have been obtained for each disk at different wavelengths, we have evaluated the spectral index of each simulated disk at different snapshots of their evolution. In particular, since we have referenced to the work of Tazzari et al. (2021b), we have considered $\lambda_2 = 0.89\,\mathrm{mm}$ and $\lambda_1 = 3.10\,\mathrm{mm}$ and we have applied Eq. 3.15 to determine the spectral index.

3.3 Results

The following section contains the main results obtained through our analysis. Subsection 3.3.1 firstly introduces the results obtained for the reproducibility of the spectral index distribution and then focuses on the simultaneous reproducibility of both the spectral index and the size-luminosity distribution. We underline the characteristics of the disks needed to match the observed distributions. In Subsect. 3.3.2 we extend the analysis to some extra cases (different opacity models, IMF and number of substructures). In Subsect. 3.3.3 we present some extra results that are linked to future development of this work and open problems in the protoplanetary disk field. To compare the simulated distributions with the observed ones, a possible age spread of the simulated disks was taken into account. That is, for each simulated disk, the observables taken into account for the creation of the overall simulated distributions were randomly selected from the snapshots at 1 Myr, 2 Myr, and 3 Myr.

We compare our simulated spectral index distributions to the observed sample adopted in Tazzari et al. (2021b). The latter is a collection of disks from Lupus region, detected at 0.89mm (Ansdell et al. 2016) and 3.1mm (Tazzari et al. 2021b), and Taurus and Ophiucus star-forming regions (Ricci et al. 2010a,b). We compare our simulated size-luminosity distribution to the observed sample reported in Andrews et al. (2018b).

3.3.1 Spectral index and size-luminosity distribution

The main focus of this study has been to investigate the population synthesis outcome for the spectral index distribution of smooth and sub-structured disks. The left and middle panels of Fig. 3.2 show the clear difference that has been found between smooth and sub-structured disks. Indeed, if we consider the entire parameter space of the initial conditions adopted and reported in Table 3.2, we observe the first important indication obtained through our simulations: smooth disks cannot produce a low value of the spectral index, that is $\alpha_{0.89-3.1mm} \leq 2.5$, while sub-structured disks produce both spectral index values around 3.5 and below 2.5, thus populating the observed spectral index region. This result confirms and extends the findings of previous studies (e.g Pinilla et al. 2012) that had already shown the need for the presence of substructures to reproduce the spectral index values observed modeling individual disks.

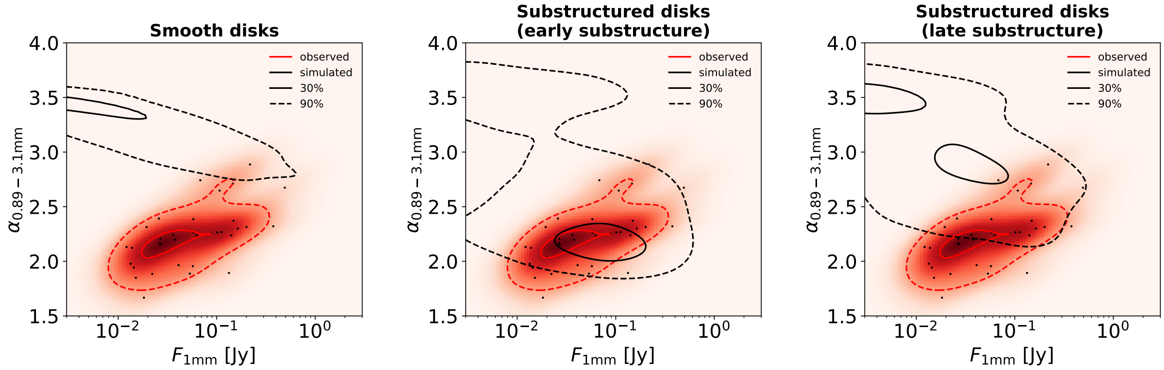

Figure 3.2: Spectral index distribution smooth disks (left) vs sub-structured disks (middle and right), for the entire parameter space of initial conditions (Table 3.2).
Middle plot: planet randomly inserted in a range between 0.1-0.4 Myr. Right plot: planet randomly inserted in a range between 0.4-1 Myr.
Heatmap of the observed disks with the black dots representing each single observed disk. The black and red lines refer to the simulated results and the observational results respectively. In particular, the continuous lines encompass the 30% of the cumulative sum of the disks produced from the simulations or observed. The dashed lines encompass the 90% instead.
We compare our simulated spectral index distribution to the observed sample adopted in Tazzari et al. (2021b). The latter is a collection of disks from Lupus region, detected at 0.89mm (Ansdell et al. 2016) and 3.1mm (Tazzari et al. 2021b), and Taurus and Ophiucus star-forming regions (Ricci et al. 2010a,b).

This is because a small value of the spectral index could be achieved due to the production of large dust particles and/or to the presence of optically thick regions originating from the accumulation of large quantities of solids. Neither can be achieved in a smooth disk due to the radial drift mechanism which preferentially removes the largest grains and depletes the overall dust mass. Moreover, since radial drift is stronger for the largest particles, it not only avoids creating more massive particles in general but also removes the massive particles created in the disk even faster. Substructure stops or slows down particle radial drift enabling particle growth and/or leading to the formation of optically thick regions. An in-depth investigation of the real cause behind the production of low spectral index values in the case of the presence of substructure is provided later in this section.

As a next step, we derive the initial conditions of the substructured disks that allow the production of a population in agreement with the observed one. In this regard, a second important result uncovered by this analysis involves the formation time of substructure. The middle and right panels of Fig. 3.2 show the comparison between the spectral index distribution obtained for disks in which the substructure is inserted in a range between

0.1 Myr and 0.4 Myr after the start of the simulation (early formation case) and those in which it is inserted in a range between 0.4 Myr and 1 Myr (late formation case). The delayed insertion of the substructure leads to the production of spectral indices tending to higher values, larger than those observed. Thus, both the ubiquity of substructures and their rapid formation are required to produce spectral index values in the observed range.

If the substructure is thought to be caused by a planet, as in our case, such a constraint on the formation time of substructure translates into an indication of the formation time of the planet associated with it. This leads to important insights into planetary formation theories. Namely, that planet formation is fast, in contrast with earlier formation models, such as Pollack et al. (1996). The result obtained on the rapid formation of substructure appears to be along the same lines as studies concerning the formation of giant planets such as Savvidou & Bitsch (2023), and with the results obtained by Stadler et al. (2022) when exploring the possibility of producing a small spectral index for different sets of initial disk parameters.

Having ascertained these two main results (ubiquity of substructures and their rapid formation), we therefore focused on the study of disks with substructure and in which they form rapidly ($0.1 Myr \leqslant t_p \leqslant 0.4 Myr$).

To characterize the initial conditions necessary to reproduce the observed distribution of the spectral index, the distribution of initial parameters associated with different selected regions in the spectral index vs. flux diagram was analyzed. Figure 3.3 shows the comparison between the observed and simulated distribution of the spectral index (top left panel) and the size luminosity distribution (top middle panel), while the blue panels show the distribution of parameters sampled. In particular, red contours represent the distribution we want to match while the black contours in the observational space show the resulting distribution of our population. Figure 3.16 in Appendix B shows the distribution of the initial parameters for the entire sampled parameter space (see Table 3.2). However, to compare the simulated disks with the observed ones, we filtered our original dataset selecting disks with a spectral index, size and flux of the order of the observed ones (see Fig. 3.3 and its description).
Figure 3.3 shows that we need a $M_{disk} \gtrsim 10^{-2.3} M_\star$ to produce disks with a flux of the order of the observed disks.

Figures 3.4, 3.5, 3.6 and 3.7 show the initial conditions and their distribution for three different regions in the spectral index vs. flux diagram. Figure 3.4 shows the distribution for the initial conditions leading to disks with a spectral index below 2.5. Figure 3.5, Fig. 3.6 and Fig. 3.7 show the initial conditions that lead to the production of disks populating three different flux regions ($F_{1mm} \leq 0.1 Jy$, $F_{1mm} \leq 0.01 Jy$ and $F_{1mm} > 0.1 Jy$, respectively), still in the case of disks producing a spectral index below 2.5.

Figure 3.4 shows a relationship between α and M_{disk}; to produce disks with a spectral index below 2.5, as α increases, M_{disk} must also increase. This general trend between α and M_{disk} primarily reflects the fact that to produce a low spectral index value, it is necessary to have an efficient trapping mechanism. For low α values, the trapping mechanism is highly efficient, and thus even disks that are not extremely massive are capable of producing low spectral index values, since although the system has little material available, it is still able to trap most of it. As α increases, the efficiency of the trapping mechanism tends to decrease, for example increased diffusivity, that is more grains will escape the bump, and decreased particle size in the fragmentation limit which are less efficiently trapped by the radial drift (Zhu et al. 2012), so to cope with this effect it is necessary to increase the reservoir of material available. Most of the material will not be trapped due to the lower trapping efficiency, but there will be enough material available for a good amount to be trapped and produce a low spectral index value. The observed trend also partly reflects the condition imposed on the drawing of the m_p value (i.e., $m_p < M_{disk}$). Indeed, Eq. 3.5, which describes the efficiency of the trapping mechanism, shows that low α values favor the trapping mechanism and generally make it unnecessary to have corresponding high m_p values. Nevertheless, to keep the trapping mechanism efficient as α increases, the value of m_p must be increased. But since the latter is limited by the condition $m_p < M_{disk}$, it is necessary to increase the value of M_{disk} to have access to the desired production of more massive planets.

In more detail, as shown in Fig. 3.5, if we also add a condition on the final flux value, we see that this flux region is populated by disks having $10^{-2.3}M_\star \lesssim M_{disk} \lesssim 10^{-1}M_\star$ and a value of $\alpha \lesssim 10^{-3}$ in the M_{disk} vs α space; the same upper limit on α is observed in the v_{frag} vs α space. The upper limit for M_{disk} is simply related to the fact that we want to populate a low-flux region. The upper limit for α comes from the fact that wanting to populate a low flux region we need lighter disks, thus a smaller value of α because we need to trap the little material available efficiently. Furthermore, a selection of disks with $v_{frag} \gtrsim 500cm/s$ in the v_{frag} vs M_{disk} space can be noted. Indeed for values of $v_{frag} \lesssim 500cm/s$ it becomes harder to trap as the Stokes number will become too small. It is further noted that this region is mostly populated by disks with $r_p \lesssim 0.75 r_{\rm c}$. Indeed, placing the gap too far away will lead to the production of a higher flux as the surface area of the ring will increase. More in detail, Fig 3.6 shows that disk with a flux $F_{1mm} \leq 0.01Jy$, lower than the observed disks' fluxes, are associated with the lowest α values, i.e $\alpha \lesssim 10^{-3.5}$.
In contrast, Fig. 3.7 shows that the "high-flux" region ($F_{1mm} > 0.1Jy$) is characterised by disks with an α that covers the full range $10^{-4} - 10^{-2}$ in the M_{disk} vs α space, but favouring the $\alpha \gtrsim 10^{-3}$ cases, and in general a $M_{disk} \gtrsim 10^{-1}M_\star$. The latter result reflects the request to populate the "high-flux" region. A relationship between v_{frag} and α is also evident, as one grows, so does the other. There is also a selection for planets with $m_p \gtrsim 150M_\oplus$ as in this case we are dealing with higher α in general, so a higher mass of the planet is needed to increase the efficiency of the trapping.

Having obtained these constraints on the initial conditions, we can now argue in the other direction: which cuts need to be imposed on the initial conditions to obtain a match be-

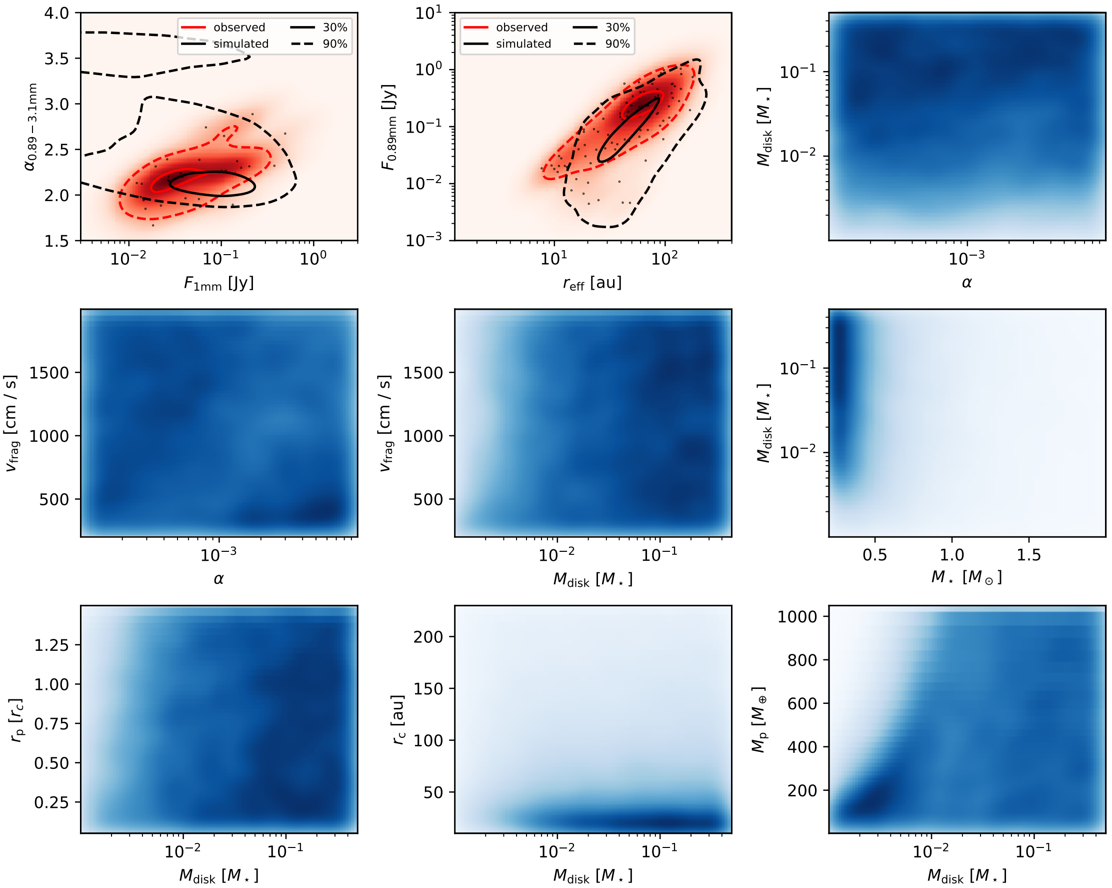

Figure 3.3: Spectral index, size-luminosity and initial parameters distributions for the parameter space of the initial conditions selecting disks with a spectral index $0 \leq \alpha_{0.89-3.1mm} \leq 4$, $10^{-3}Jy \leq F_{1mm} \leq 10Jy$, $10^{-3}Jy \leq F_{0.89mm} \leq 10Jy$ and $10^{0.1}au \leq r_{eff} \leq 10^{2.6}au$. We compare our simulated spectral index distribution to the observed sample adopted in Tazzari et al. (2021b). The latter is a collection of disks from Lupus region, detected at 0.89mm (Ansdell et al. 2016) and 3.1mm (Tazzari et al. 2021b), and Taurus and Ophiucus star-forming regions (Ricci et al. 2010a,b). We compare our simulated size-luminosity distribution to the observed sample reported in Andrews et al. (2018b).

tween the simulated and observed distribution. Figure 3.8 shows the result obtained by selecting the disks associated to the following initial conditions, for the early formation scenario (i.e., $0.1Myr \leqslant t_p \leqslant 0.4Myr$): $10^{-3.5} \leqslant \alpha \leqslant 10^{-2.5}$, $10^{-2.3}M_\star \leqslant M_{disk} \leqslant 10^{-0.5}M_\star$, $v_{frag} \geq 500cm/s$, $m_p \geq 150M_\oplus$ and $r_p \leq 0.75r_{\mathrm{c}}$. By filtering these disks, it is possible to obtain a spectral index distribution consistent with that observed. While more sophisticated constraints might lead to an even more precise match, the purpose of this work is to show that it is possible to reproduce the observed distribution of the spectral index from a disk population synthesis and outline the most basic constraints on the initial conditions

necessary to achieve this.
Although the cuts made were based solely on an analysis of the behavior of the spectral index distribution, Fig. 3.8 shows a remarkable result, that is not only applied cuts allow reproducing the spectral index distribution, but they simultaneously yield a distribution in the size-luminosity diagram that matches the observed one.

Figure 3.17 and Fig. 3.18 reported in Appendix C show the distribution of initial parameters associated with two different regions of the size-luminosity diagram. Both regions exhibit a spread in the initial α value that, while favoring intermediate (low-flux region) or high-intermediate (high-flux region) values, nevertheless extends over the entire range. Similarly to the two regions previously analyzed for the spectral index, in the size-luminosity diagram, the low-flux region requires $M_{disk} \gtrsim 10^{-2.3} M_\star$, while the high-flux region becomes more selective as it requires $M_{disk} \gtrsim 10^{-1} M_\star$. Furthermore, in the case of the low-flux region, the selection of $r_p \leq 0.75 r_\mathrm{c}$ is observed again. It is therefore reasonable that the cuts applied to reproduce the observed distribution of the spectral index also lead to an automatic and simultaneous matching of the distribution in the size-luminosity diagram. Besides, no further cuts appear necessary to improve the matchings. Better matchings could be obtained only by refining the way the cuts are made, that is imposing non-homogeneous distributions for the initial conditions and introducing an analytical way to compare the simulated disks' distribution to the observed one.

An in-depth investigation of the real cause behind the production of low spectral index values for substructured disks has been performed evaluating the flux averaged optical depth associated to each simulated disk. Figure 3.9 shows the value of the flux averaged optical depth obtained for the distribution of substructured disks obtained applying our best cuts. The figure reveals that a small value of the spectral index is achieved by the production of an optically thick region in the disk, originating from the accumulation of material due to the presence of substructure. We can also notice the presence of optically thin or marginally optically thin disks, which explains why we can now reproduce the size-luminosity distribution with only substructured disks. Indeed, Zormpas et al. (2022) study, from which it emerged that a mix of smooth and substructured disks was necessary to reproduce the SLR, relied on the hypothesis that all substructured disks were optically thick. The different parameter space adopted in our study, in particular the choice to draw $M_\star$ from the IMF instead of a uniform distribution, leads to a population of disks composed of a mix of optically thick substructured disks and optically thin (or marginally optically thin) substructured disks. This reflects directly on the final distribution of the simulated disks in the size-luminosity diagram. While massive disks, populating the high flux region ($-1 \leqslant log\ F_{0.89mm}[Jy] \leqslant 0.5$) of the size-luminosity diagram, will still populate the observed region as they are optically thick as in Zormpas et al. (2022); disks in the low flux region ($-2 \leqslant log\ F_{0.89mm}[Jy] \leqslant -1$) are now optically thin or marginally optically thin, and not optically thick as assumed in Zormpas et al. (2022), thus they experience a change (i.e., reduction) in their flux allowing them to fall in the observed region. Thus we can now reproduce the observed size-luminosity distribution having no longer required a mix of smooth and substructured disks.

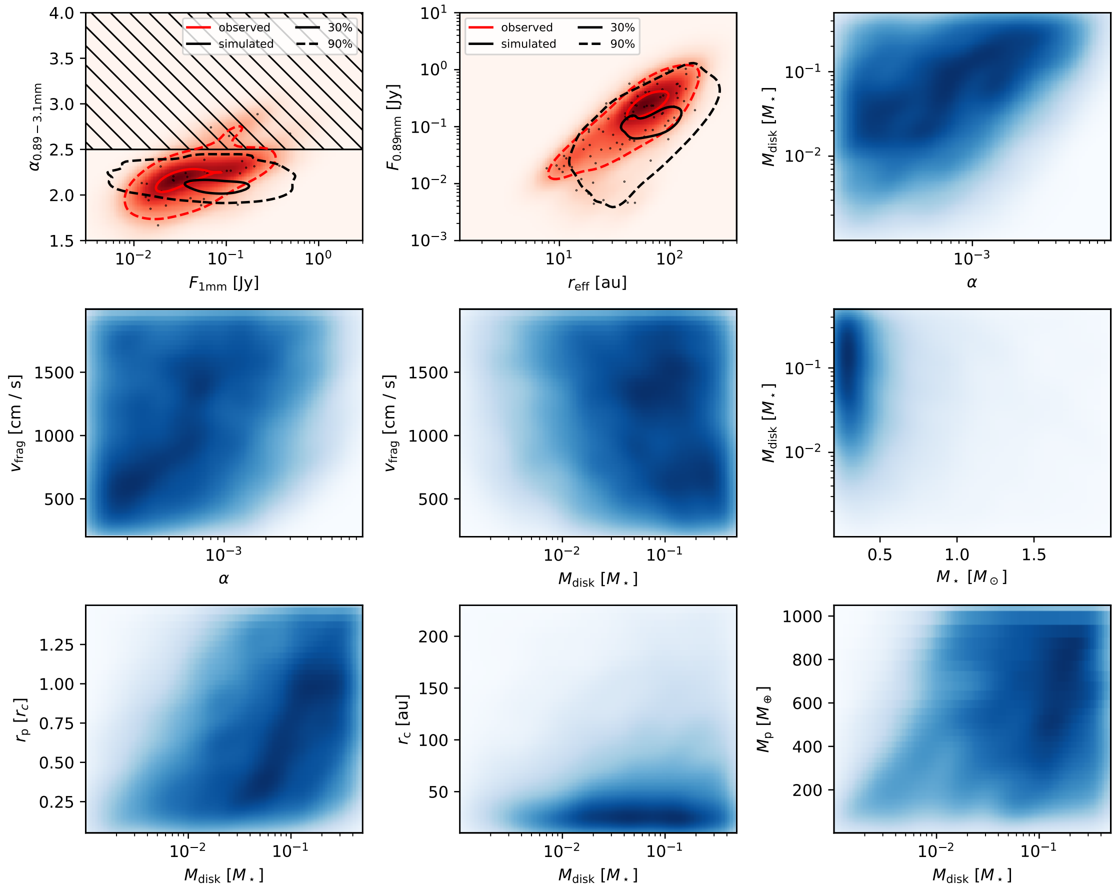

Figure 3.4: Spectral index, size-luminosity and initial parameters distributions selecting disks with a spectral index $\alpha_{0.89-3.1mm} \leq 2.5$.

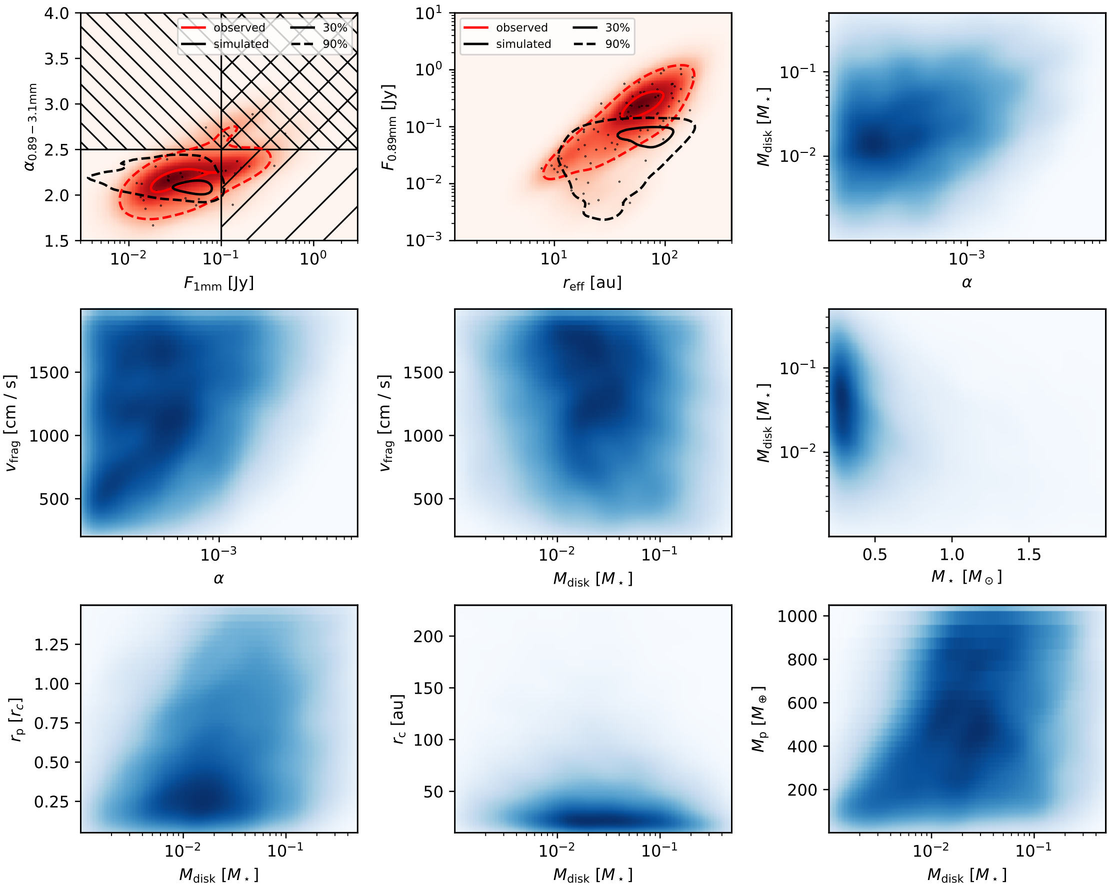

Figure 3.5: Spectral index, size-luminosity and initial parameters distributions selecting disks with a spectral index $\alpha_{0.89-3.1mm} \leq 2.5$ and a flux $F_{1mm} \leq 0.1 Jy$.

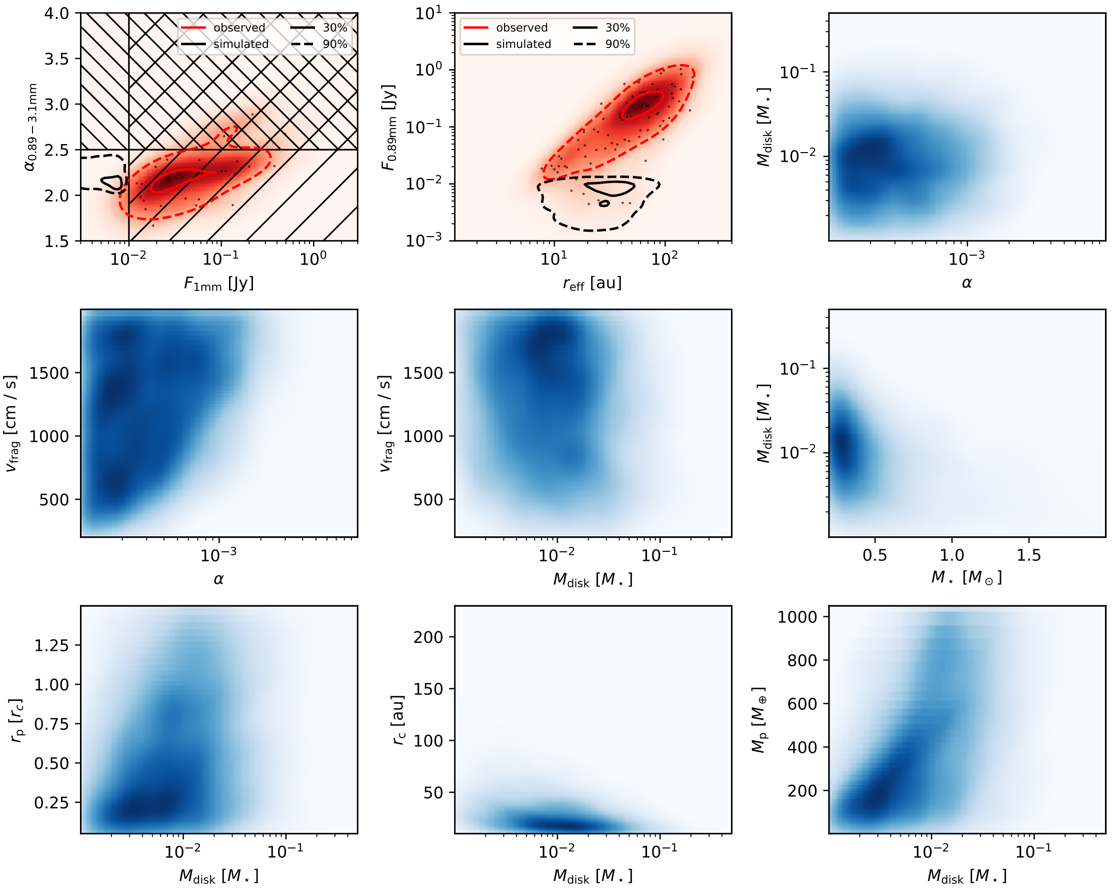

Figure 3.6: Spectral index, size-luminosity and initial parameters distributions selecting disks with a spectral index $\alpha_{0.89-3.1mm} \leq 2.5$ and a flux $F_{1mm} \leq 0.01Jy$.

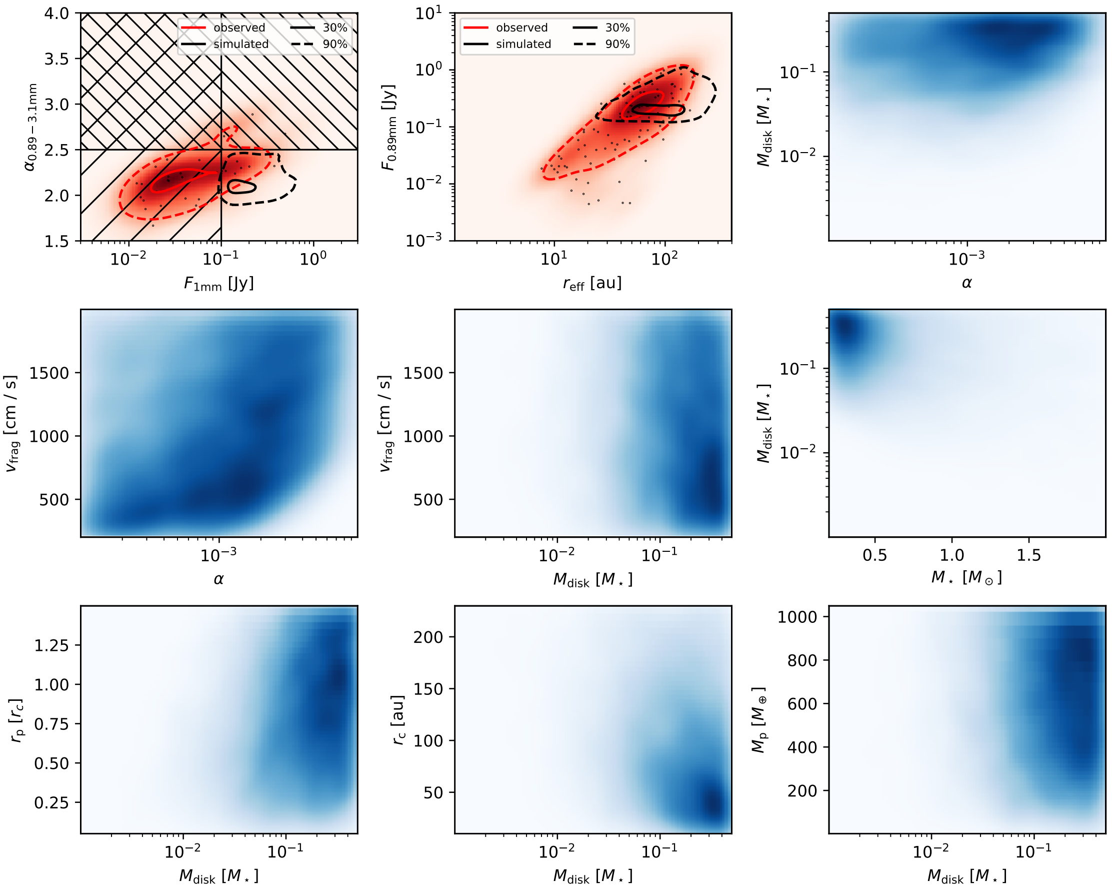

Figure 3.7: Spectral index, size-luminosity and initial parameters distributions selecting disks with a spectral index $\alpha_{0.89-3.1mm} \leq 2.5$ and a flux $F_{1mm} > 0.1Jy$.

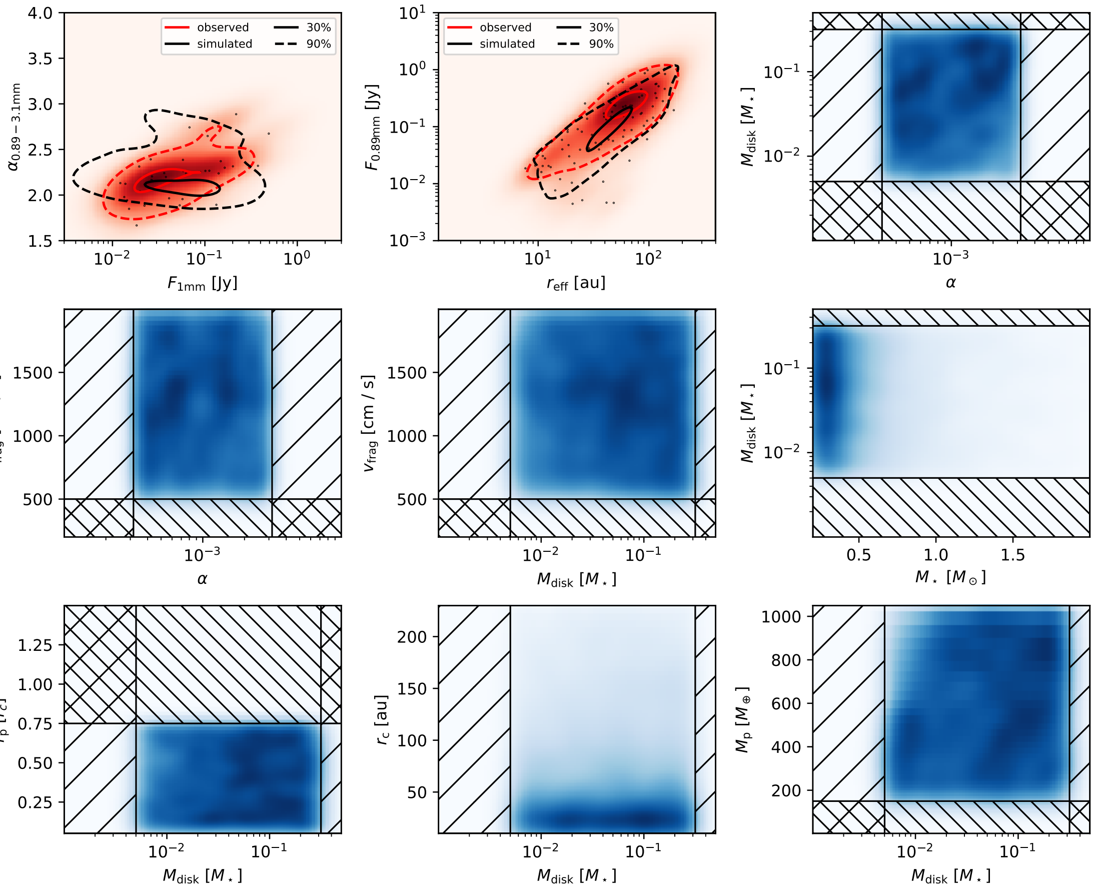

Figure 3.8: Spectral index, size-luminosity and initial parameters distributions selecting disks with: $10^{-3.5} \leqslant \alpha \leqslant 10^{-2.5}$, $10^{-2.3}M_\star \leqslant M_{disk} \leqslant 10^{-0.5}M_\star$, $v_{frag} \geq 500cm/s$, $m_p \geq 150M_\oplus$, $r_p \leq 0.75r_c$.

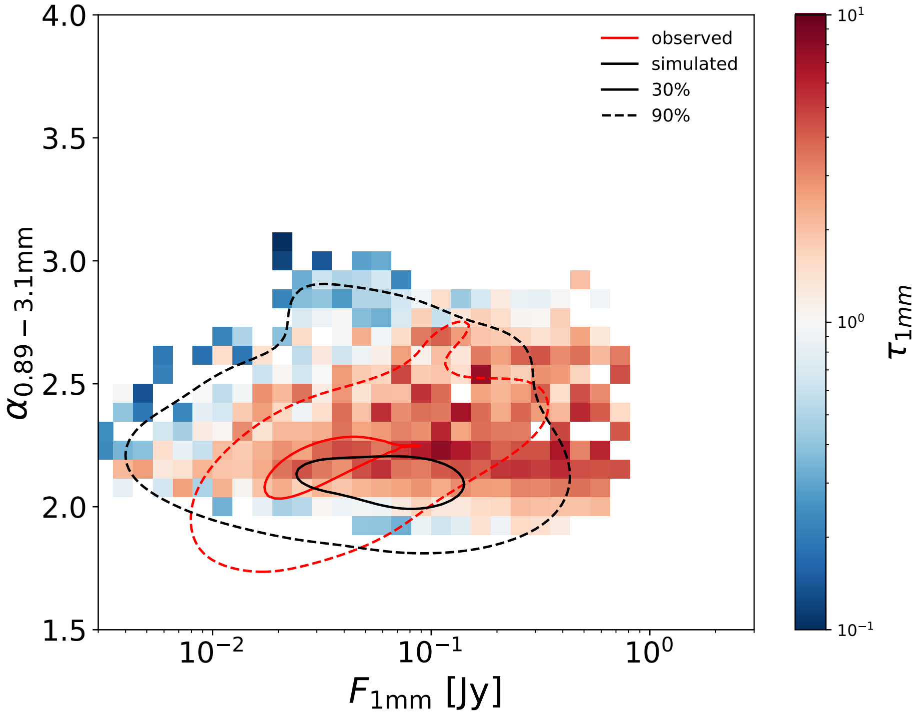

Figure 3.9: Spectral index and flux averaged optical depth distribution at 1mm (τ_{1mm}), selecting disks with: $10^{-3.5} \leqslant \alpha \leqslant 10^{-2.5}$, $10^{-2.3} M_{\star} \leqslant M_{disk} \leqslant 10^{-0.5} M_{\star}$, $v_{frag} \geq 500 cm/s$, $m_p \geq 150 M_{\oplus}$, $r_p \leq 0.75 r_c$. The optical depth associated with each bin is the mean of the flux averaged optical depths of the disks belonging to each bin.

3.3.2 Case studies on opacities, the IMF and double substructure

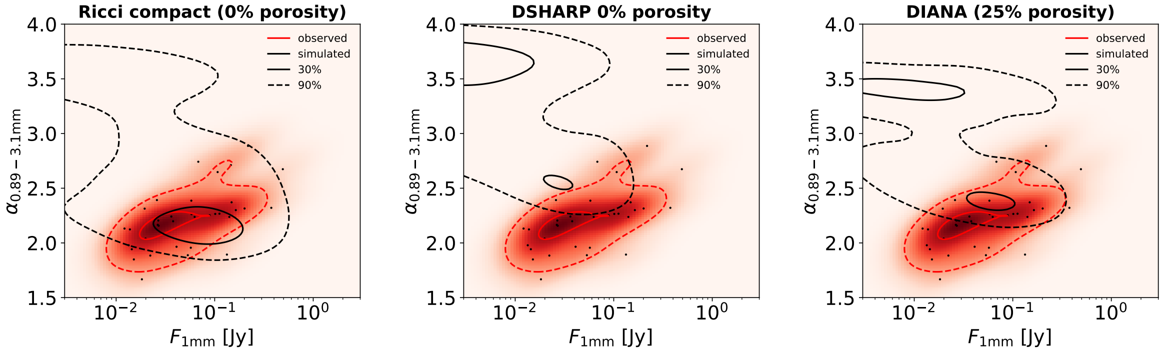

Figure 3.10: Spectral index distribution sub-structured disks, for the entire parameter space of initial conditions (Table 3.2) for three different opacities: Ricci opacity model (Ricci et al. 2010b) with compact grains (Ricci compact model) as in Rosotti et al. (2019a)(0% grain porosity), DSHARP (Birnstiel et al. 2018) with 0% grain porosity and DIANA (Woitke et al. 2016)(25% grain porosity) opacities. Heatmap of the observed disks with the black dots representing each observed disk. The black and red lines refer to the simulated results and the observational results respectively. In particular, the continuous lines encompass the 30% of the cumulative sum of the disks produced from the simulations or observed. The dashed lines encompass the 90% instead.

Opacities

All the results shown in the previous section were obtained considering Ricci compact opacities (Rosotti et al. (2019a)). This opacity proved to be the best for reproducing the observed distributions, as already noted in Zormpas et al. (2022) and Stadler et al. (2022), for the study of the size-luminosity distribution. Figure 3.10 shows the comparison between the distributions obtained for the spectral index in the case of three different opacities: Ricci opacity model (Ricci et al. 2010b) with compact grains (Ricci compact model) as in Rosotti et al. (2019a)(0% grain porosity), DSHARP (Birnstiel et al. 2018) with 0% grain porosity and DIANA (Woitke et al. 2016)(25% grain porosity) opacities. The only model capable of producing disks with a spectral index ~ 2.2 is the Ricci compact model. DIANA produces disks with low spectral index values but fails to populate the observed regions at $\alpha_{0.89-3.1mm} \leq 2.3$. DSHARP suffers from the same problem as DIANA and also produces disks with a lower flux that do not reach the observed extent. The latter problem was already highlighted by Zormpas et al. (2022), who also showed that as grain opacity increases, disk flux reduces for the DSHARP case (see Appendix D for an in-depth investigation of different % of grain porosity for DSHARP opacities). The difference in the final result between DIANA and Ricci compact lies in the compactness of the grains considered for Ricci. Instead, the difference between Ricci and DSHARP resides in the fact that Ricci's opacity has a value ~ 8.5 higher than DHSARP's at the position of the opacity cliff if, for example, we consider a wavelength of $850\mu m$. This explains the difference in the final flux value of the disks obtained in the case of Ricci compared to DSHARP.

Disk population synthesis represents a valuable tool that can provide additional insight into the definition of opacity and dust composition models. Dust composition, porosity and opacities determinations represent one of the main open problems in the field. Indeed, they are crucial hypotheses for determining disk characteristics, but we still lack precise knowledge of both of them. Thus, the solution to this problem constitutes a very active field in the protoplanetary disk panorama, which is being addressed through different techniques such as: sub-mm polarisation (Kataoka et al. 2016, 2017), scattered light phase function (Ginski et al. 2023) and multi-wavelength studies (Guidi et al. 2022). The multi-wavelength study by Guidi et al. (2022) and the scattered light phase function study by Ginski et al. (2023) support the idea of low-porosity grains in protoplanetary disks. In particular, Guidi et al. (2022) study on grain properties in the ringed disk of HD 163296 shows that low porosity grains better reproduce the observations of HD 163296. Ginski et al. (2023) shows that two categories of aggregates can be associated with polarized phase functions. The first category consists of fractal, porous aggregates, while the second consists of more compact and less porous aggregates. In particular, they note that disks belonging to the second category host embedded planets which may trigger enhanced vertical mixing leading to the production of more compact particles. Instead, sub-mm polarisation studies (Kataoka et al. 2016, 2017) provide important information about the maximum grain size. They constrain a maximum grain size $\sim 100\mu m$. In an optically thin regime, such grains would not produce a low spectral index value; indeed $\alpha_{0.89-3.1mm} \leq 2.5$ requires grains larger than $1mm$. However, as Fig. 3.9 shows, low spectral index values are produced by the presence of an optically thick region caused by substructure.

IMF

As shown in Table 3.2, the stellar masses of our simulations were drawn from the functional form of the IMF proposed by Maschberger (2013) which is based on the standard IMFs of Kroupa (Kroupa (2001),Kroupa (2002)) and Chabrier (Chabrier 2003). To make our comparison to the observed disk distributions more consistent, we also accounted for the fact that the observed disks may be characterized by a stellar mass distribution that differs from the standard IMFs of Kroupa and Chabrier. We therefore constructed an IMF from a Kernel Density Estimate derived from the stellar mass distributions of the samples in Tazzari et al. (2021a) and Andrews et al. (2018b). Figure 3.11 shows that the results obtained with the new IMF deviate only slightly from the classical IMFs case, mainly by a slight shift to higher fluxes.

Double substructure

Figure 3.12 shows the comparison of the behavior of the simulated spectral index distribution when one or two planets (i.e., substructures) are inserted during the evolution of the

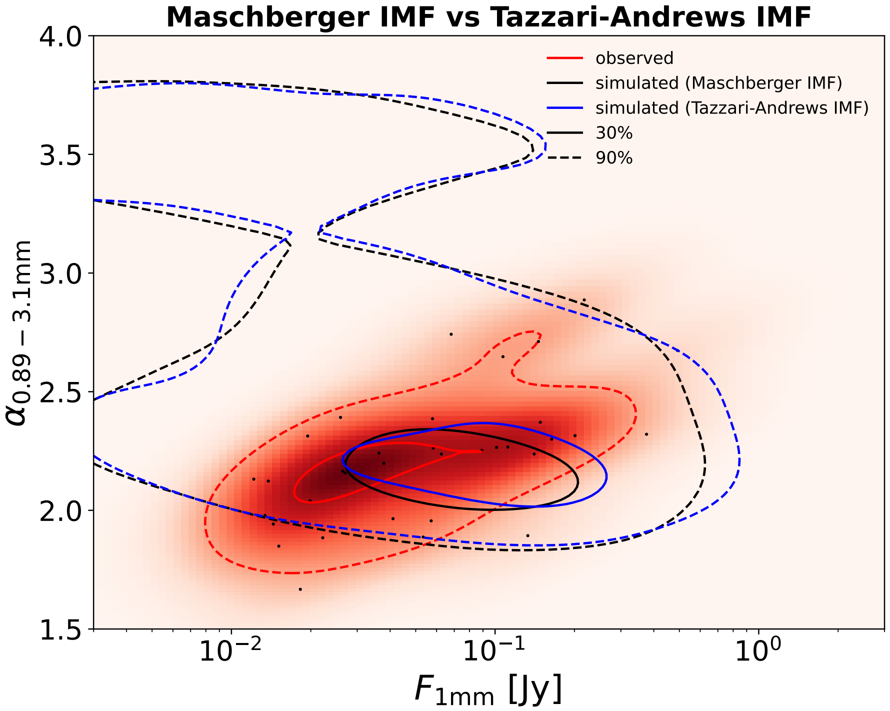

Figure 3.11: Spectral index distribution sub-structured disks, for the entire parameter space of initial conditions (Table 3.2) for two different IMF. Heatmap of the observed disks with the black dots representing each single observed disk. The black, blue and red lines refer to the simulated results obtained for the functional form of the IMF proposed by Maschberger (2013) (black) which is based on the standard IMFs of Kroupa (Kroupa (2001),Kroupa (2002)) and Chabrier (Chabrier 2003), the Andrews-Tazzari IMF (blue) and the observational results (red). In particular, the continuous lines encompass the 30% of the cumulative sum of the disks produced from the simulations or observed. The dashed lines encompass the 90% instead.

disk. We have analyzed two different scenarios: first scenario the earliest substructure is the innermost (blue contours), second scenario the earliest substructure is the outermost (green contours). It can be immediately observed that it is possible to produce spectral index values in the observed region even in the generic case of two substructures. In general, the double substructure distributions are similar to the single substructure case and simply show a shift in the final flux produced. In the case of two substructures and faster insertion of the innermost substructure, the value of the final flux produced is lower than in the case of faster insertion of the outer substructure, as in the latter case there is a greater accumulation of material in the outer region with which a greater area is associated. A brighter disk is therefore generally obtained in the second scenario. The double substructure case with primary insertion of the innermost substructure, produces generally fainter disks than the single substructure case because a range of $r_p = 0.05 - 0.5\ r_c$ was selected for the double substructure case.

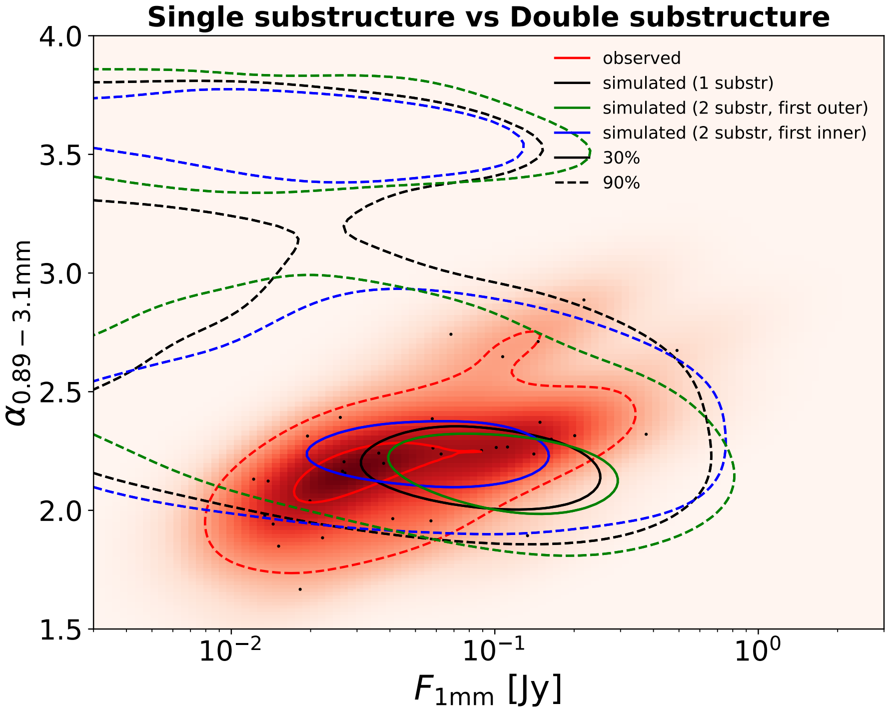

Figure 3.12: Spectral index distribution sub-structured disks, for the entire parameter space of initial conditions (Table 3.2) for disks with one substructure and two substructures. Heatmap of the observed disks with the black dots representing each single observed disk. The black, blue, green and red lines refer to the simulated results obtained for single substructured disks (black), simulated results obtained for double substructured disks with the inner planet inserted first (blue), double substructured disks with the outer planet inserted first (green) and the observational results (red). In particular, the continuous lines encompass the 30% of the cumulative sum of the disks produced from the simulations or observed. The dashed lines encompass the 90% instead.

3.3.3 Future perspectives and open problems: spectral index at longer wavelength, disk size and MHD disk winds

In Fig. 3.13 we investigate the distribution of the spectral index evaluated at longer wavelengths ($\alpha_{3.1-9mm}$) for the disk filtered by applying the best cuts introduced in Subsect. 3.3.1. We observe a slight general shift towards larger values of the spectral index since less of the emitting region produced by the substructure is optically thick and some parts become optically thin while not being made of very large grains. This behavior opens an interesting window towards disk mass estimates since a search for optically thin emission is required for accurate estimate of disk masses, and thus also for the estimate of the amount of material available for planet formation. However, at the moment, only a small sample of disks have been observed at large wavelengths, for instance only around 30 disks have been observed at $\lambda \sim 7.5mm$ (mostly by Rodmann et al. (2006) and Ubach et al. (2012)).

In this study we have chosen to define our effective radius for defining disk size as the radius that encloses the 68% of the total amount of flux produced by the disk ($r_{eff,68\%}$), following Tripathi et al. (2017). Nevertheless, most recent observations have considered the radius that encloses 90% of the emission ($r_{eff,90\%}$). However, Hendler et al. (2020) finds a 1-1 correlation between $r_{eff,90\%}$ and $r_{eff,68\%}$(see Fig. 15 in (Hendler et al. 2020)). We have thus evaluated $r_{eff,90\%}$ for each disk and tested if our population synthesis can reproduce this observed trend. Figure 3.14 shows the behavior exhibited by three different disk populations: smooth disks, substructured disks without applying any cut to the initial conditions and substructured disks filtered with our best conditions (i.e., $10^{-3.5} \leqslant \alpha \leqslant 10^{-2.5}$, $10^{-2.3}M_\star \leqslant M_{disk} \leqslant 10^{-0.5}M_\star$, $v_{frag} \geq 500cm/s$, $m_p \geq 150M_\oplus$, $r_p \leq 0.75r_c$). We select a set of 10^4 disk per population and fit each sample exploiting linmix implementation of the Bayesian linear regression method developed by Kelly (2007). Results reported in Table 3.3 show that smooth disks do not reproduce the correlation observed in Hendler et al. (2020), same applies to the sub-structured disks population. However, filtering the sub-structured disk population selecting disks with $10^{-3.5} \leqslant \alpha \leqslant 10^{-2.5}$, $10^{-2.3}M_\star \leqslant M_{disk} \leqslant 10^{-0.5}M_\star$, $v_{frag} \geq 500cm/s$, $m_p \geq 150M_\oplus$, $r_p \leq 0.75r_c$, that is applying the best cuts introduced in Subsect. 3.3.1 which lead to a matching to both the spectral index and size-luminosity distribution, we obtain a correlation between $log r_{eff,90\%}$ and $log r_{eff,68\%}$. This result further strengthens the outcomes outlined in Subsect. 3.3.1 concerning the need for substructure in protoplanetary disks and the associated parameters space.

In this work we focused on the classical scenario in which disks evolve viscously. However, in recent years, the hypothesis that the evolution of the disk is driven by magnetic winds has become increasingly popular. We therefore aim to expand our investigation on the MHD disk winds scenario in the future, to determine if and what differences might arise compared to the viscous scenario. In this respect, Zagaria et al. (2022) shows that current available observations do not allow discerning between viscous and magnetic wind scenarios and that from the dust perspective, there is little difference between the viscous

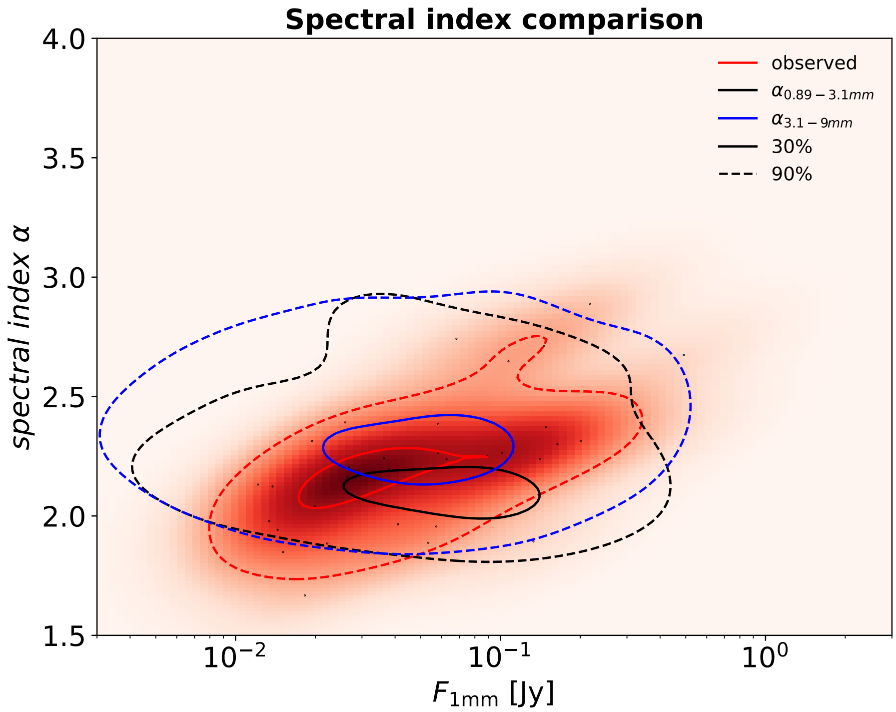

Figure 3.13: Spectral index distribution sub-structured disks, selecting disks with: $10^{-3.5} \leqslant \alpha \leqslant 10^{-2.5}$, $10^{-2.3}M_{\star} \leqslant M_{disk} \leqslant 10^{-0.5}M_{\star}$, $v_{frag} \geq 500cm/s$, $m_p \geq 150M_{\oplus}$, $r_p \leq 0.75r_{\mathrm{c}}$. Heatmap of the observed disks with the black dots representing each single observed disk. The black, blue and red lines refer to the simulated results obtained for $\alpha_{0.89-3.1mm}$ (black), simulated results obtained for $\alpha_{3.1-9mm}$ (blue) and the observational results ($\alpha_{0.89-3.1mm}$) (red). In particular, the continuous lines encompass the 30% of the cumulative sum of the disks produced from the simulations or observed. The dashed lines encompass the 90% instead.

Table 3.3: $log r_{eff,90\%}$ vs $log r_{eff,68\%}$ fit results.

Disk population	intercept	slope	regression intrinsic scatter	linear correlation coefficient
smooth disks	1.09±0.01	0.60±0.01	0.06±0.00	0.67±0.01
sub-structured disks	0.62±0.01	0.75±0.01	0.06±0.00	0.78±0.00
sub-structured disks (best cuts)	0.30±0.00	0.88±0.00	0.01±0.00	0.95±0.00

Notes. $log r_{eff,90\%}$ vs $log r_{eff,68\%}$ fit results for three different disk populations: smooth disks, substructured disks without applying any cut to the initial conditions and substructured disks filtered with our best cuts (i.e., $10^{-3.5} \leqslant \alpha \leqslant 10^{-2.5}$, $10^{-2.3}M_{\star} \leqslant M_{disk} \leqslant 10^{-0.5}M_{\star}$, $v_{frag} \geq 500cm/s$, $m_p \geq 150M_{\oplus}$, $r_p \leq 0.75r_{\mathrm{c}}$). Fit results obtained exploiting linmix implementation of the Bayesian linear regression method developed by Kelly (2007).

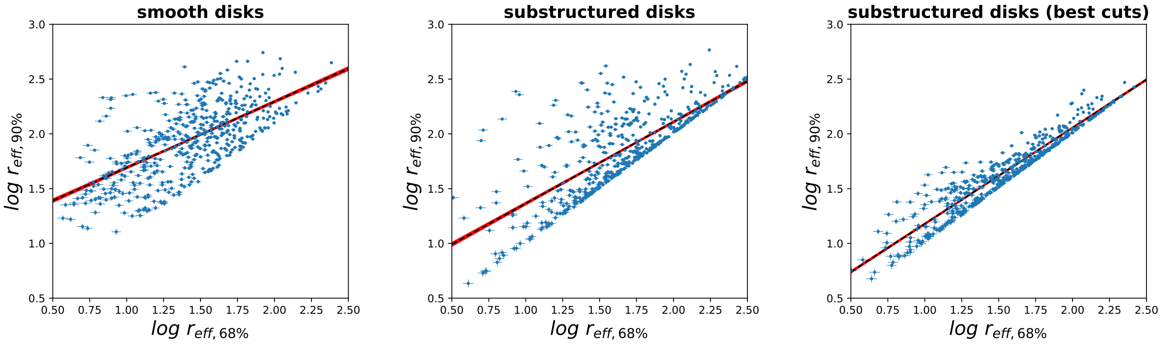

Figure 3.14: Comparison between $logr_{eff,90\%}$ and $logr_{eff,68\%}$ dust disk sizes for smooth disks (left panel), entire set of sub-structured disks (middle panel), sub-structured disks selected from our best case (i.e., $10^{-3.5} \leqslant \alpha \leqslant 10^{-2.5}$, $10^{-2.3}M_\star \leqslant M_{disk} \leqslant 10^{-0.5}M_\star$, $v_{frag} \geq 500cm/s$, $m_p \geq 150M_\oplus$, $r_p \leq 0.75r_c$)(right plot). Blue dots represent a subset of the disks used for the estimate of the correlation between $r_{eff,90\%}$ and $r_{eff,68\%}$. The best fit obtained exploiting linmix implementation of the Bayesian linear regression method developed by Kelly (2007) is shown as a black line, with a 1σ confidence interval reported in red.

case and MHD winds. Indeed, they show that SLR can be reproduced even by MHD disk winds models, except for the very large disks, which can, however, be explained assuming the presence of substructures. We therefore expect, adopting an MHD wind model, similar conclusions to those obtained for the viscous scenario.

3.4 Conclusions

In this work, we conducted a study aimed at understanding the possibility of reproducing the observed spectral index distribution of protoplanetary disks. We exploited the two-pop-py 1D evolutionary model for the dust and gas in protoplanetary disks. We considered both smooth and substructured disks and a wide initial parameter space. We firstly compared the simulated distribution obtained for the spectral index to the observed ones reported in Tazzari et al. (2021b) and then analysed the possibility of matching also the size-luminosity distribution considering the observed distribution reported in Andrews et al. (2018b). We have been able to identify the initial conditions and the kind of disks needed to match the spectral index distribution and in particular to match simultaneously also the size-luminosity distribution. These are the main results we have outlined:

1. Substructures are needed to produce small values of the spectral index in the range of the observed ones; smooth disks produce only large values of the spectral index (Fig. 3.2).

2. The substructure has to be formed quickly, that is within $\sim 0.4Myr$ (Fig. 3.2) to produce a value of the spectral index below 2.5.

3. Filtering the substructure disks with $10^{-3.5} \leqslant \alpha \leqslant 10^{-2.5}$, $10^{-2.3} M_\star \leqslant M_{disk} \leqslant 10^{-0.5} M_\star$, $v_{frag} \geq 500 cm/s$, $m_p \geq 150 M_\oplus$, $r_p \leq 0.75 r_\mathrm{c}$ we obtain a match between the spectral index simulated distribution and the observed distribution (Fig. 3.8), proving that it is possible to reproduce the observed distribution for a reasonable range of initial conditions.

4. An in-depth investigation of the real cause behind the production of low spectral index values for substructured disks revealed that this is achieved by the production of an optically thick region in the disk, originating from the accumulation of material due to the presence of substructure.

5. The matching obtained between the simulated and observed spectral index distribution automatically ensures a matching between the corresponding simulated and observed size-luminosity distribution.

6. It is possible to reproduce the size-luminosity distribution with a population of only substructured disks, thus, no longer requiring the mix of smooth and substructured disks proposed in Zormpas et al. (2022).

7. The 1-1 correlation between the $r_{eff,90\%}$ and $r_{eff,68\%}$ observed in Hendler et al. (2020) cannot be reproduced by smooth disks and by the entire sample of sub-structured disks, but it can be retrieved filtering the sub-structured disk sample with the same parameter ranges that lead to reproducing both the spectral index and size-luminosity distributions.

8. Studying different opacities (Ricci compact Rosotti et al. 2019a,DSHARP Birnstiel et al. 2018,DIANA Woitke et al. 2016) we showed that the only one capable of leading to a matching of the spectral index distribution is the Ricci compact opacity. Only opacities with high absorption efficiency can reproduce the observed spectral indices.

9. Disks with two substructures can match the spectral index distribution, showing a behavior similar to the single substructure case.

This study shows that it is possible to reproduce the observed distributions for both spectral index and size-luminosity, extending the results obtained for individual disk studies to the broader level of a disk population synthesis.

Acknowledgements

L.D. and T.B. acknowledge funding by the Deutsche Forschungsgemeinschaft (DFG, German Research Foundation) under grant 325594231 and Germany's Excellence Strategy - EXC-2094 - 390783311. T.B. acknowledges funding from the European Research Council (ERC) under the European Union's Horizon 2020 research and innovation programme under grant agreement No 714769.
PP acknowledges funding from the UK Research and Innovation (UKRI) under the UK government's Horizon Europe funding guarantee from ERC (under grant agreement No 101076489).
GR acknowledges funding from the Fondazione Cariplo, grant no. 2022-1217, and the European Research Council (ERC) under the European Union's Horizon Europe Research & Innovation Programme under grant agreement no. 101039651 (DiscEvol). Views and opinions expressed are however those of the author(s) only, and do not necessarily reflect those of the European Union or the European Research Council Executive Agency. Neither the European Union nor the granting authority can be held responsible for them.

Appendix A: Evolving L_{star} vs fixed L_{star}

In this appendix we show the comparison between the spectral index simulated distribution obtained for a scenario in which we keep the luminosity of the hosting star fixed and the scenario in which we let $L_\star$ evolve by time.

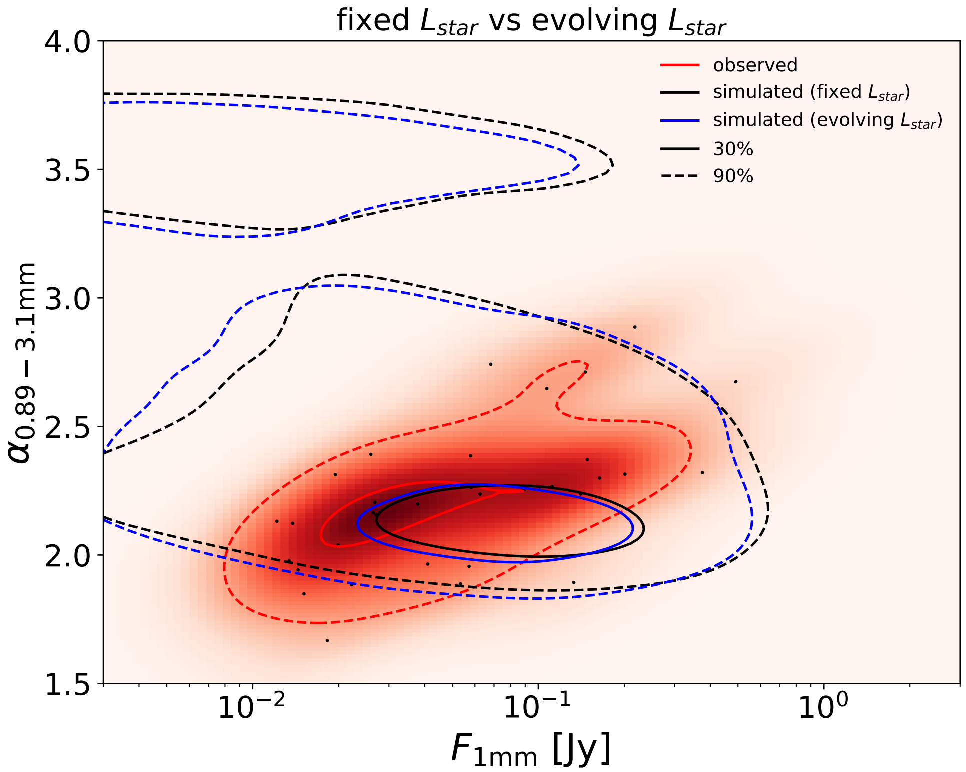

Figure 3.15: Spectral index distribution sub-structured disks, for the entire parameter space of initial conditions (Table 3.2) for the scenario in which we keep L_{star} fixed during the disk evolution (black lines) and the scenario in which L_{star} evolve by time. Heatmap of the observed disks with the black dots representing each single observed disk. The black, blue and red lines refer to the simulated results obtained for fixed L_{star} (black), simulated results obtained for evolving L_{star} (blue) and the observational results (red). In particular, the continuous lines encompass the 30% of the cumulative sum of the disks produced from the simulations or observed. The dashed lines encompass the 90% instead.

Appendix B: Initial parameter distributions

In this appendix we show the spectral index, size-luminosity and initial parameters distributions for the entire parameter space of the initial conditions (see Table 3.2).

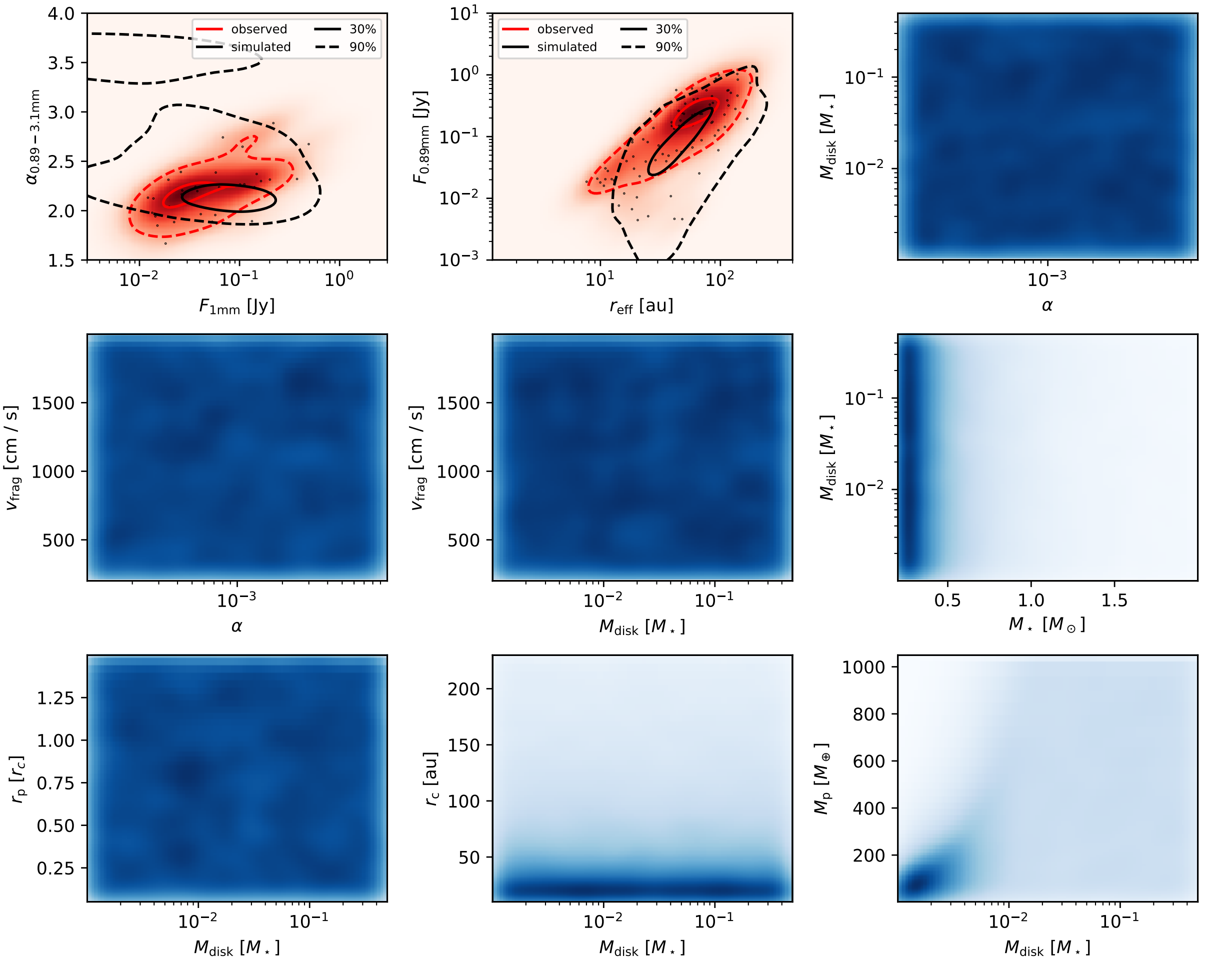

Figure 3.16: Spectral index, size-luminosity and initial parameters distributions for the entire parameter space of the initial conditions. We compare our simulated spectral index distributions to the observed sample adopted in Tazzari et al. (2021b). The latter is a collection of disks from Lupus region, detected at 0.89mm (Ansdell et al. 2016) and 3.1mm (Tazzari et al. 2021b), and Taurus and Ophiucus star-forming regions (Ricci et al. 2010a,b). We compare our simulated SLR to the observed sample reported in Andrews et al. (2018b).

Appendix C: Size-luminosity diagram analysis

In this appendix we show the spectral index, size-luminosity and initial parameters distributions selecting disks populating two different regions in the size-luminosity diagram.

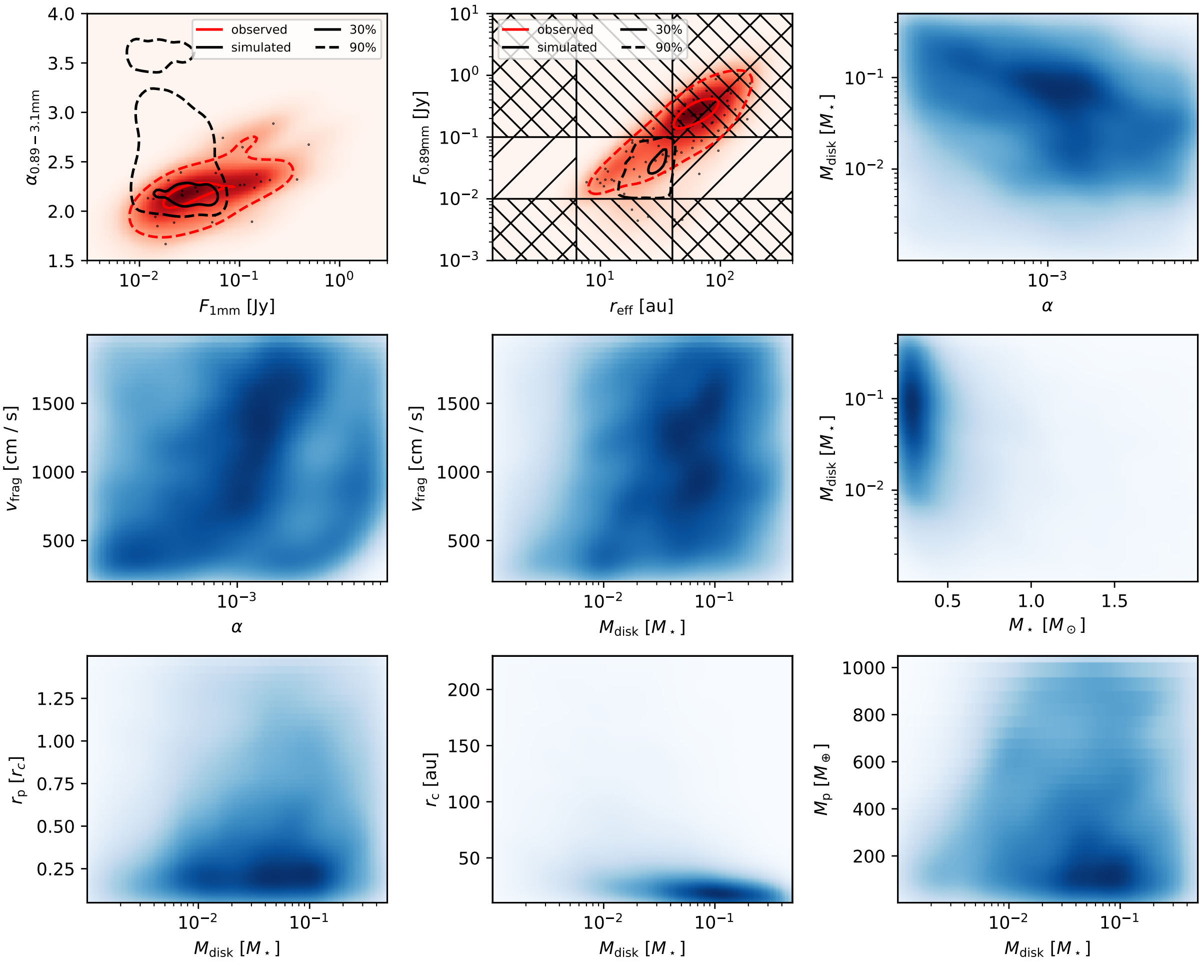

Figure 3.17: Spectral index, size-luminosity and initial parameters distributions selecting disks with $0.8 \leqslant log\ r_{eff}[au] \leqslant 1.6$ and $-2 \leqslant log\ F_{0.89mm}[Jy] \leqslant -1$.

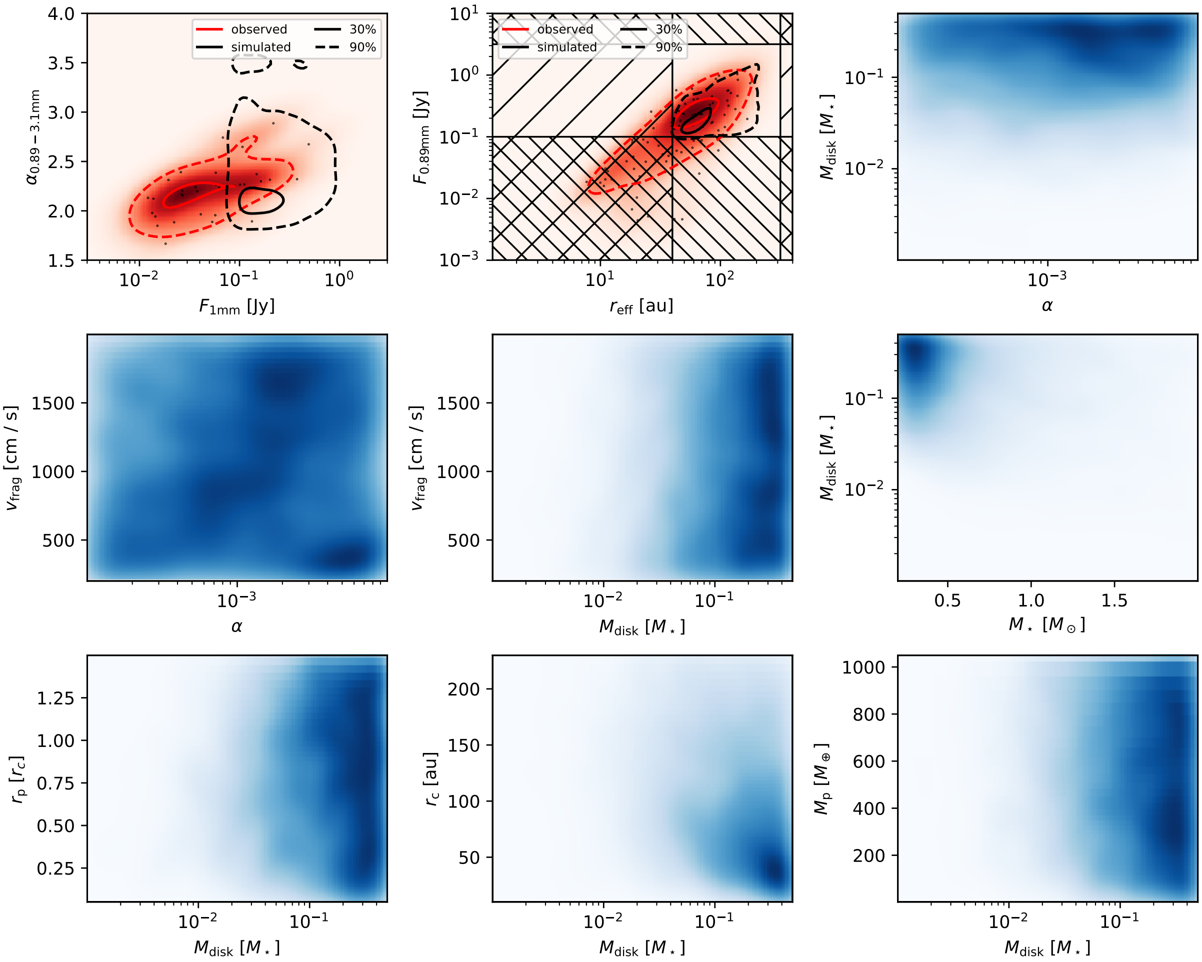

Figure 3.18: Spectral index, size-luminosity and initial parameters distributions selecting disks with $1.6 \leqslant log\ r_{eff}[au] \leqslant 2.5$ and $-1 \leqslant log\ F_{0.89mm}[Jy] \leqslant 0.5$.

Appendix D: DSHARP opacities for different % of grain porosity

In this appendix we show the comparison between the spectral index simulated distribution obtained for DHSARP opacities (Birnstiel et al. 2018) for different % of grain porosity.

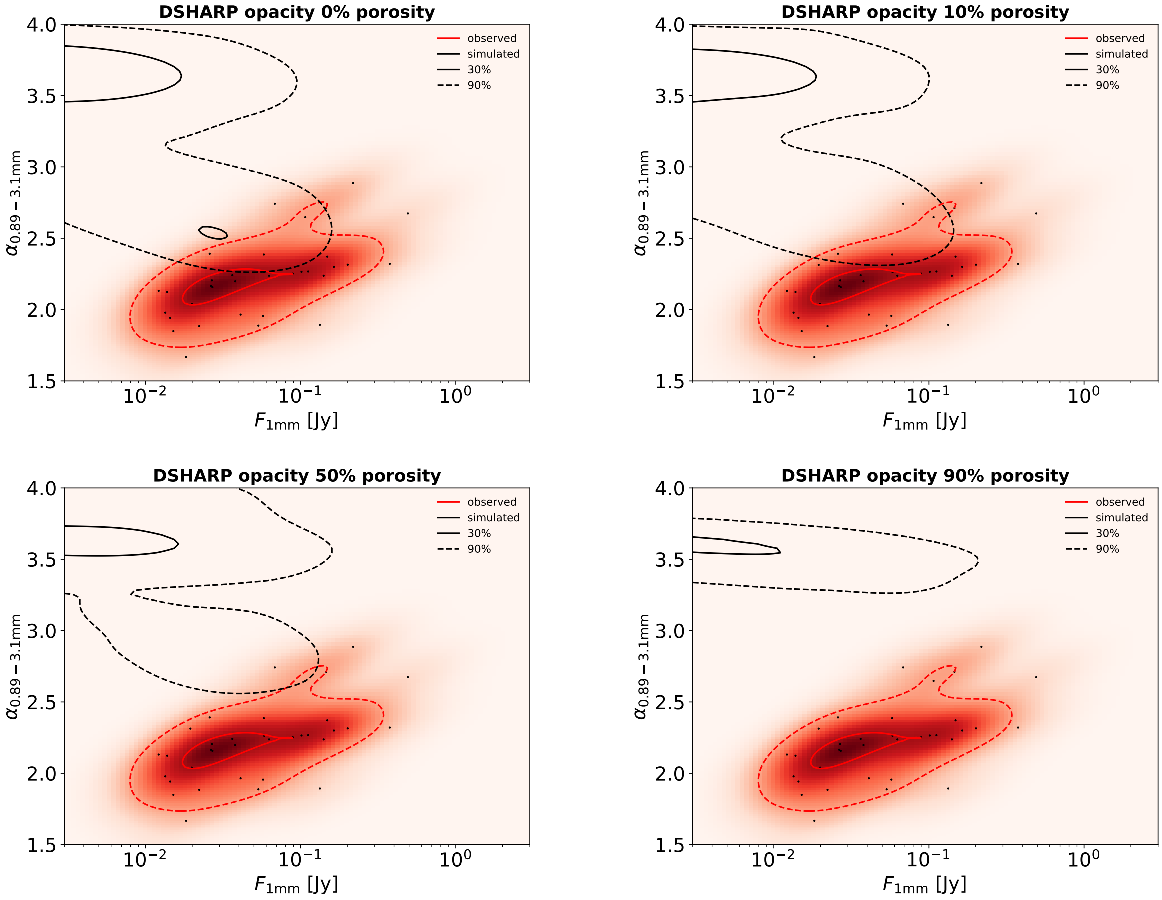

DSHARP opacity 0% porosity

DSHARP opacity 10% porosity

DSHARP opacity 50% porosity

DSHARP opacity 90% porosity

Figure 3.19: Spectral index distribution sub-structured disks, for the entire parameter space of initial conditions (Table 3.2) for DSHARP opacities (Birnstiel et al. 2018) for four different % of grain porosity. Heatmap of the observed disks with the black dots representing each observed disk. The black and red lines refer to the simulated results and the observational results respectively. In particular, the continuous lines encompass the 30% of the cumulative sum of the disks produced from the simulations or observed. The dashed lines encompass the 90% instead.

Chapter 4

Gas and dust disk radii: indications for future disk population synthesis

This chapter is included in *Luca Delussu, Rossella Anania, Tilman Birnstiel, Claudia Toci, Giovanni Rosotti, Tommy Chi Ho Lau and Sebastian Stammler (2025)* and is to be submitted to Astronomy & Astrophysics.

4.1 Introduction

The study and interest in protoplanetary disk substructures has been significantly fueled by the advent of the Atacama Large Millimeter/Sub-Millimeter Array (ALMA) and its high-resolution observations. The iconic image of HL Tau, captured by ALMA in 2015 (ALMA Partnership et al. 2015), not only provided the first direct image of a protoplanetary disk but also revealed, for the first time, the presence of substructures. In particular, surveys such as DSHARP (Andrews et al. 2018a; Huang et al. 2018) and Long et al. (2018) have shown that optically thick substructures are ubiquitous in bright disks, sparkling even more the interest in understanding the physical processes that give rise to such substructures and their implications for disk evolution and planet formation. Among the various mechanisms proposed to explain the origin of substructures in protoplanetary disks (see e.g., Bae et al. 2023), the most widely accepted scenario is that at least wide substructures are created by the presence of planets or protoplanets within the disk. This hypothesis is supported by kinematic evidence (Teague et al. 2018; Pinte et al. 2018; Izquierdo et al. 2022) and by direct imaging of planets within gaps, such as in PDS70 (Müller et al. 2018; Keppler et al. 2018). The interest in protoplanetary disk substructures extends beyond the observational findings. Indeed, it also arises from theoretical considerations, as they may help address several key open problems in disk and planet formation theories. In particular, the fact that dust radially drifts inward in a disk as a result of the different velocities between the dust and gas in the disk (Weidenschilling 1977) is a well-known open question of the field. Solid particles migrate too quickly in smooth disks due to the high efficiency of the radial drift (Takeuchi & Lin 2002, 2005), challenging the formation of planetesimals and leading to mismatches in spectral index predictions (Birnstiel et al. 2010b; Pinilla et al. 2013) and size-luminosity distributions (Tripathi et al. 2017; Andrews et al. 2018b; Rosotti et al. 2019a) compared to observations. Substructures, particularly the presence of local maxima in the pressure profile of the disk, can mitigate solid particle migration, or completely trap them at the pressure maximum (Pinilla et al. 2012, 2013). If the substructure trapping mechanism is effective, solid particles accumulate at the pressure maximum enhancing the local dust-to-gas ratio (Drążkowska et al. 2016; Yang et al. 2017), thus creating a favorable region for planetesimal formation (Youdin & Shu 2002; Youdin & Lithwick 2007). Additionally, substructures provide an ideal environment for planet formation by promoting processes like streaming instability and pebble accretion (Lau et al. 2022). They also offer solutions to planetary migration challenges, such as explaining the location of Jupiter within the Solar System (Lau et al. 2024).

The quick disappearance of large-sized dust particles in disks is not the only challenging problem of disk evolution. The gas component is also evolving with time, and the gas size, commonly measured as the radius enclosing $68, 90$ or 95% of the molecular emission of CO, is also studied as a way to probe disk evolution (Trapman et al. 2023). Different mechanisms of disk evolution predict different pathways for gas disk sizes. In a scenario where accretion is driven by viscosity, disk sizes should globally increase with time (the so-called 'viscous spreading' effect) to conserve angular momentum, while such expansion is not required in case of magnetohydrodynamical disk winds removing angular momentum from the disk (for a review see e.g., Manara et al. 2023). Environmental effects such as multiplicity (e.g., Zagaria et al. 2023), external and internal photoevaporation (e.g., Clarke 2007; Winter & Haworth 2022; Anania et al. 2025b) can reduce or modify the size of a disk, with substantial consequences for the evolution of disks.

A way to test with the same models the efficiency of radial drift and the mechanism driving disk evolution is to focus on the evolution of the dust and gas sizes of protoplanetary disks at the same time, value studied observationally by several authors in different star-forming regions (Sanchis et al. 2021 for Lupus, Long et al. 2022 for Taurus). For the measured sources, the vast majority of the disks in the sample show a ratio $R_{\rm CO}/R_{\rm dust}$ between 2-4, with a few (about 15%) outliers with $R_{\rm CO}/R_{\rm dust} > 4$. This hints at a similar evolution mechanism for the two star-forming regions. However, theoretical analysis modeling the evolution of protoplanetary disks assuming viscous evolution, grain growth and pure radial drift find that, for a broad range of disks values, the value of $R_{\rm CO}/R_{\rm dust}$ becomes > 5 after a short time. Substructures have also been proposed as a possible solution to this discrepancy between the observed and simulated gas-to-dust size ratios in protoplanetary disks. Toci et al. (2021) invoke the presence of unresolved or undetected substructures in most (or all) protoplanetary disks as the most likely explanation for reconciling the simulated gas-to-dust size ratios with the observed values. Indeed, the discrepancy between the small observed size ratios (i.e., $R_{\rm CO}/R_{\rm dust} < 5$) and the high simulated size ratios (i.e., $R_{\rm CO}/R_{\rm dust} > 5$) may potentially be addressed by increasing the disk dust size, $R_{\rm dust}$, through the presence of substructures within the disk. In Delussu et al. (2024) we show, performing a population synthesis, that substructures, and their rapid formation, are needed to produce small values of the spectral index in the range of the observed ones, and they allow reproducing the observed distributions for both spectral index and size-luminosity. In this work, we aim to extend our previous population study by investigating whether, as proposed by Toci et al. (2021), substructures can provide a solution to the gas and dust size ratio problem. Moreover, we aim to understand whether it is possible to match the gas-dust size, size-luminosity, and spectral index distributions at the same time and what initial disk parameters are required for that. Furthermore, we aim to explore other potential solutions to the $R_{\mathrm{CO}}/R_{\mathrm{dust}}$ problem, should the mere presence of substructures fail to fully resolve it. In this work, we consider the impact of the stellar formation environment, exploring whether the disk external photoevaporation caused by the ultraviolet (UV) radiation emitted by OBA-type stars may explain the $R_{\mathrm{CO}}/R_{\mathrm{dust}}$ observed in the population of disks in the Lupus region. The UV radiation induces outside-in photoevaporation of the outermost disk regions, which are poorly gravitationally bound to the central star (e.g. Adams et al.2004, Winter & Haworth2022). The far ultraviolet (FUV) component dominates over the extreme ultraviolet (EUV) in the nearby regions in ∼200 pc from the Sun, which host few massive stars (mainly of late-type B and early-type A). However, indirect evidences and models show that even a moderate FUV field (1-10 G_0) can significantly affect disk evolution (e.g. van Terwisga & Hacar2023), with photoevaporative mass loss rates depending on the stellar mass and disk parameters (e.g. Haworth et al.2023).

This paper is structured as follows: in Sect. 4.2, we describe our computational models for the evolution of the disk and introduce the analysis method exploited to compare to disk observations. Section 4.3 introduces the main results obtained and the comparison to the observed distributions. We first introduce the population synthesis results obtained with the two-pop-py model and then the results obtained for a small set of test disks using the code DustPy and in the presence of external photoevaporation. Section 4.4 presents our conclusions.

4.2 Methods

The two-population model (two-pop-py) by Birnstiel et al. (2012) and Birnstiel et al. (2015) and DustPy code (Stammler & Birnstiel 2022) have been exploited to perform numerical simulations to describe the gas and dust evolution in the disk. In the following we will describe the main characteristics of the two-pop-py model and DustPy code, and describe how external photoevaporation has been implemented in DustPy. The observables examined in this work will also be introduced, along with the process applied to evaluate each of them for every simulated disk.

4.2.1 Two-pop-py model

Two-pop-py is a tool ideally suited for disk population studies because it accurately captures the dust surface density evolution, the viscous evolution of the gas, and the particle size. Being based on a set of simple equations, it allows to perform a single simulation quickly (order of seconds), making it computationally efficient and allowing for the execution of large numbers of simulations within a reasonable amount of time. The two-pop-py model, as implemented and described in Delussu et al. (2024), has been used in this work. For an in-depth discussion, we refer to Delussu et al. (2024); a summary of its key elements is outlined as follows:

- The protoplanetary gas disk is evolved according to the viscous disk evolution equation (Lüst 1952; Lynden-Bell & Pringle 1974) using the turbulent effective viscosity as parameterized in Shakura & Sunyaev (1973).
- Adopting the two-population model described in Birnstiel et al. (2012) we evolve the dust surface density assuming that the small dust is tightly coupled to the gas while the large dust particles can decouple from it and drift inward.
- The initial gas surface density follows the Lynden-Bell & Pringle (1974) self-similar solution with a γ viscosity exponent set to 1 for the initial profiles of all the disks.
- We have adopted a passive irradiated disk temperature model (Kenyon et al. 1996) with a disk floor temperature set to 10 K. No viscous heating or other processes have been considered.
- Both disks without substructure (referred to as smooth disks) and with substructure have been examined. Substructure has been modeled as a gap due to the presence of a planet inserted in the disk. To mimic the presence of a planetary gap we have subdivided the α viscosity parameter into two different values: $\alpha_{\rm gas}$ and $\alpha_{\rm dust}$. The presence of the planet has been modeled as a local variation of the $\alpha_{\rm gas}$ parameter. Given the inverse proportionality between $\alpha_{\rm gas}$ and $\Sigma_{\rm g}$ in a steady-state regime, a bump in the $\alpha_{\rm gas}$ profile results in a gap in the $\Sigma_{\rm g}$ profile, effectively simulating the presence of a planetary gap. Moreover, this approach preserves the viscous evolution of $\Sigma_{\rm g}$. We have adopted Kanagawa et al. (2016) prescription to model planetary gaps created in the disk.

In this work, the 1D disk has been spatially modeled with a radial grid that ranges from 0.05 au to 10 000 au. The cells of the grid are spaced logarithmically. The main characteristics of the grid model are reported in Table 4.1. A total of 10^5 simulations have been performed for each population synthesis. To map all the parameter space, the set of initial conditions adopted for each disk has been constructed randomly drawing each parameter from a probability distribution function (PDF). As in Delussu et al. (2024), the main parameters that have been taken into account to describe both smooth and sub-structured disks are: disk mass ($M_{\rm disk}$), stellar mass ($M_{\rm star}$), disk characteristic radius ($r_{\rm c}$), viscous

Table 4.1: Fixed parameters (two-pop-py model).

Parameter	Description	Value or Range
Σ_d/Σ_g	initial dust-to-gas ratio	0.01
ρ_s $[g/cm^3]$	particle bulk density (no porosity)	1.7 (Ricci opacity)
γ	viscosity parameter	1
r $[au]$	grid extent	0.05-10000
n_r $[cells]$	grid resolution	2000
t $[Myr]$	duration of each simulation	3

Table 4.2: Disk initial parameters (two-pop-py population synthesis).

Parameter	Description	Range	PDF
α	viscosity parameter	$10^{-4} - 10^{-2}$	log uniform
M_{disk} $[M_{\rm star}]$	initial disk mass	$10^{-3} - 0.5$	log uniform
$M_{\rm star}$ $[M_\odot]$	stellar mass	$0.2 - 2.0$	IMF
$r_{\rm c}$ $[au]$	characteristic radius	$10 - 230$	log uniform
v_{frag} $[cm/s]$	fragmentation velocity	$200 - 2000$	uniform
m_p $[M_\oplus]$	planet mass	$1 - 1050$	uniform
r_p $[r_{\rm c}]$	planet position	$0.05 - 1.5$	uniform
t_p $[Myr]$	planet formation time	$0.1 - 0.4$	uniform

Notes. Disk initial parameters and corresponding probability distribution function (PDF) from which their value is drawn for each single simulation. The drawing of the m_p value was performed after the M_{disk} to impose the further physically reasonable restriction of $m_p < M_{disk}$. In the case of multiple substructures, we applied the following constraint: $\sum_i m_{p,i} < M_{disk}$.

parameter (α) and fragmentation velocity ($v_{\rm frag}$). The stellar mass values, have been drawn from a functional form of the IMF proposed by Maschberger (2013). Sub-structured disks have been characterized by three additional parameters: the mass of the planet creating the gap ($\rm m_p$), the time ($\rm t_p$) at which the planet was inserted, and the position ($\rm r_p$) of the planet within the disk. Table 4.2 shows the range that has been adopted for each parameter and the corresponding PDFs adopted for each of them.

4.2.2 DustPy and external photoevaporation

To perform numerical simulations of disks undergoing external photoevaporation, we used the existing and tested implementation of `DustPy` (Stammler & Birnstiel 2022) integrated with an external module that includes the effect of an external FUV field (Anania et al. 2025a). `DustPy` simulates the radial evolution of gas and dust in a viscous disk, considering a distribution of particle species subject to advection, diffusion, grain growth by coagulation

Table 4.3: Disk initial parameters (DustPy simulations).

Parameter	Description	Value
$M_{\rm star}$ $[M_\odot]$	stellar mass	0.3, 1
M_{disk} $[M_{\rm star}]$	initial disk mass	0.01, 0.1
$r_{\rm c}$ $[au]$	characteristic radius	20, 50, 100
α	viscosity parameter	$10^{-3.5}$, $10^{-2.5}$
v_{frag} $[cm/s]$	fragmentation velocity	1000
m_p $[M_J]$	planet mass	1
r_p $[r_{\rm c}]$	planet position	0.5, 0.7, 1, 1.2
$F_{\rm FUV}$ $[\rm G_0]$	FUV flux	4

Notes. Disk initial parameters used for `DustPy` simulations of disk subject to viscous evolution and external photoevaporation. The FUV flux corresponds to the average in the Lupus region and is constant during the simulation.

and fragmentation based on Birnstiel et al. (2010a). As in the Two-po-py model, the gas surface density of the disc, $\Sigma_{\rm g}$, evolves accordingly with the Lynden-Bell & Pringle (1974) viscous evolution, where we included an extra term to account for the loss of material in external winds:

$$\frac{\partial}{\partial t}\Sigma_{\rm g} = \frac{3}{R}\frac{\partial}{\partial R}\left(R^{1/2}\frac{\partial}{\partial R}(\nu\Sigma_{\rm g}R^{1/2})\right) - \dot{\Sigma}_{\rm ext}, \tag{4.1}$$

where $\dot{\Sigma}_{\rm ext}$ accounts for the rate of mass lost in external photoevaporative winds. The photoevaporative mass loss rate is evaluated performing a bi-linear interpolation of the FRIEDv2 grid (Haworth et al. 2023), where we assumed ISM-like Polycyclic Aromatic Hydrocarbons (PAHs) for ISM-like dust. Specifically, following the numerical implementation of Sellek et al. (2020), the grid is interpolated fixing the stellar mass and the FUV flux at the outer disk edge, and using the disk surface density at each radial position. At each time step, the disk radial position corresponding to the maximum mass loss rate defines a truncation radius (which corresponds to the optically thin/thick wind transition in the disk). To simulate the outside-in disk depletion caused by external photoevaporation, the disk material outside the truncation radius is removed accordingly to Sellek et al. (2020). The model takes into account that external photoevaporation influences the dust component, where dust grains smaller than a certain size limit, which depends on the stellar and disk parameters, are entrained in winds (Facchini et al. 2016). The study of Gárate et al. (2024) showed that dust substructures that may form in disks survive the outside-in disk depletion only if they are placed inside the truncation radius of external photoevaporation.

Due to the higher computational costs of `DustPy`, we performed a lower number of simulations based on the constraints on the parameter space placed by two-po-py simulations (Delussu et al. 2024) of not-photoevaporating disks for the initial conditions needed to reproduce the observed distributions of spectral index and size-luminosity. The initial parameters used are listed in Table 4.3. The extent of the radial grid, the dust particle distribution and the fragmentation velocity are set as in two-po-py simulations. In total we explored the parameter space performing 27 simulations. In the simulations including external photoevaporation, we assumed that the disks are subject to a constant external FUV flux of $4\,\mathrm{G}_0$, which is the average FUV flux experienced by disk-hosting stars in the Lupus star-forming region (Anania et al. 2025b). The simulated disks are let evolve up to the age of 3 Myr to compare with the Lupus disk population.

4.2.3 Observables

Post-processing the resulting profiles (surface density, maximum grain size, and disk temperature) of the simulated disks, we obtained the simulated population distribution for the disk dust radii, disk gas radii, millimeter fluxes, and spectral indices. In the following we describe the process applied to evaluate each of these observables for every simulated disk.

Millimeter fluxes

Disk fluxes have been evaluated following the procedure described in Delussu et al. (2024), that is, adopting Miyake & Nakagawa (1993) scattering solution of the radiative transfer equation and the modified Eddington-Barbier approximation (Birnstiel et al. 2018). Delussu et al. (2024) studied the effects of different opacities (Ricci compact Rosotti et al. 2019a, DSHARP Birnstiel et al. 2018, DIANA Woitke et al. 2016), and showed that only the Ricci compact opacity results in a match of the observed spectral index distribution. We therefore have adopted the Ricci compact opacity model for the analysis conducted in this paper.

Dust radii

One of the challenges in characterizing protoplanetary disks is defining their size (see Miotello et al. 2023, as a recent review). As discussed in Tripathi et al. (2017) and Rosotti et al. (2019b), the characteristic radius r_c cannot be adopted as a size indicator for disks. In large sample surveys the millimeter surface brightness profile of observed disks is typically provided, rather than their surface density profile, precluding the possibility of defining a physical dust radius as is typically done in the study of a specific source (Ricci et al. 2014; Testi et al. 2016). We have thus followed the procedure of defining an empirical radius, commonly referred to as the effective disk radius r_{eff}, which represents the radius encompassing a specified fraction of the total flux emitted by the disk. The two most commonly adopted choices are $R_{68\%}$ and $R_{90\%}$, the radii enclosing 68% and 90% of the total disk flux, respectively. As shown in Sanchis et al. (2020), $R_{68\%}$ is a safer choice, as it is usually characterized by a smaller dispersion. Based on the radii provided in the observed samples; $R_{68\%}$ has been evaluated for the comparison to the observed size-luminosity distribution (Andrews et al. 2018b), while $R_{90\%}$ has been evaluated for the comparison to the observed gas and dust radii distribution (Sanchis et al. 2021).

Gas radii

Estimating disk gas radii is even more challenging than estimating dust radii, as molecular emission lines are faint in the outer regions of protoplanetary disks. Additionally, deep gas observations are rarer as they are more time-consuming than dust continuum observations. Given their relatively brighter and optically thick emission, CO rotational emission lines, particularly ^{12}CO lines, are the most commonly used tracers for disk gas radii estimates. Given that we compared our simulated disks to the observed size distribution of disks of the Lupus star-forming presented in Sanchis et al. (2021), which provides the radius enclosing the 90% of the total flux emission of the ^{12}CO tracer, we assumed ^{12}CO as disk gas size tracer and $R_{\mathrm{CO,90\%}}$ as the gas radius for each of the simulated disks. As shown in Toci et al. (2023), $R_{\mathrm{CO,90\%}}$ is well-approximated by the radial location where the disk surface density equals a certain critical value, inhibiting ^{12}CO self-shielding.

We evaluate the disk gas radius $R_{\mathrm{CO,90\%}}$ starting from the gas critical column density threshold formula obtained by Trapman et al. (2023):

$$N_{gas,crit} = 10^{21.27-0.53log_{10}L_\star} \left(\frac{M_{gas}}{M_\odot}\right)^{0.3-0.08log_{10}L_\star} cm^{-2}. \tag{4.2}$$

Given the gas critical column density threshold, the critical surface density of the ^{12}CO tracer is given by

$$\Sigma_{crit} = 10\mu_{gas}N_{gas,crit} \tag{4.3}$$

where μ_{gas} is the mean molecular weight of the gas in the disk, adopted the standard value for protoplanetary disks (i.e, $\mu_{\mathrm{gas}} \sim 2.3\mu_{\mathrm{H}} = 1.15\mu_{\mathrm{H_2}}$). As in Eq. 4.2 the initial carbon abundance is assumed to be 10^{-4}; we account for extra carbon depletion by multiplying the critical surface density by a factor 10. The gas radius $R_{\mathrm{CO,90\%}}$ was then evaluated as the outermost radius for which the gas surface density profile obtained for each simulated disk equals its critical surface density.

Spectral index

The spectral index is defined as the slope of the (sub-)mm SED of the dust emission

$$\alpha_{mm} = \frac{dlogF_\nu}{dlog\nu}, \tag{4.4}$$

where F_ν is the disk-integrated flux at a given frequency ν[1], thus α_{mm} is the disk-integrated spectral index. Since we typically work with frequencies that are very close to each other, Eq. 4.4 can be written as

$$\alpha_{mm} = \frac{log(F_{\nu,2}/F_{\nu,1})}{log(\nu_2/\nu_1)}. \tag{4.5}$$

---

[1] All fluxes will be given in frequency space (F_ν, typically in units of Jy), even though the subscript is stating the corresponding wavelength instead of the frequency.

Eq. 4.5 has been applied to determine the spectral index for every simulated disk. Since we compare our simulated spectral index distribution to the observed Lupus region sample adopted in Tazzari et al. (2021b), which is a collection of disks detected at 0.89mm (Ansdell et al. 2016) and 3.1mm (Tazzari et al. 2021b), we have considered $\lambda_2 = 0.89\,\mathrm{mm}$ and $\lambda_1 = 3.10\,\mathrm{mm}$.

4.3 Results

The following section contains the main results obtained through our analysis. Subsection 4.3.1 presents the results obtained for the population synthesis produced with two-pop-py for the reproducibility of the gas and dust size observed distribution. In Subsection 4.3.2 we introduce the results obtained for a test population of disks exploiting DustPy code with the implementation of external photoevaporation. To compare the simulated distributions with the observed ones, a potential age spread of the simulated disks was considered. Specifically, for each simulated disk, the observables used to construct the overall simulated distributions were randomly selected from the snapshots at 1 Myr, 2 Myr, and 3 Myr. Our simulated gas and dust size distribution is compared to the observed sample reported in Sanchis et al. (2021) for the Lupus region, while the simulated spectral index distributions are compared to the observed sample from Tazzari et al. (2021b). The latter includes disks detected at 0.89mm (Ansdell et al. 2016) and 3.1mm (Tazzari et al. 2021b). The simulated size-luminosity distribution is compared to the observed sample of the Lupus region reported in Andrews et al. (2018b). In Subsection 4.3.3 we discuss our findings and their implications.

4.3.1 Population synthesis results with two-pop-py

The main focus of the study, conducted using two-pop-py model, was to investigate the population synthesis results for the gas and dust size distribution of smooth and substructured disks, to assess the validity of the solution proposed by Toci et al. (2021), namely, that substructures can solve the discrepancy between models and observations. Figure 4.1 shows the clear difference that has been found between smooth and substructured disks. If we consider the entire parameter space of the initial conditions adopted and reported in Table 4.2, we observe the first important indications obtained through our simulations:

- Smooth disks produce a large $R_{\mathrm{gas}(90\%)}/R_{\mathrm{dust}(90\%)}$ compared to observations. This result confirms and extends to the broader level of a disk population synthesis the result previously obtained by Toci et al. (2021).

- Substructured disks, either with one or two substructures, produce a size distribution shifted towards lower $R_{\mathrm{gas}(90\%)}/R_{\mathrm{dust}(90\%)}$. For both one and two substructures, the bulk of the population lies around $R_{\mathrm{gas}(90\%)}/R_{\mathrm{dust}(90\%)} \sim 4$.

- The presence of substructure(s) in the disks helps narrow the gap between theoretical models and observations, but it does not fully resolve the discrepancy.

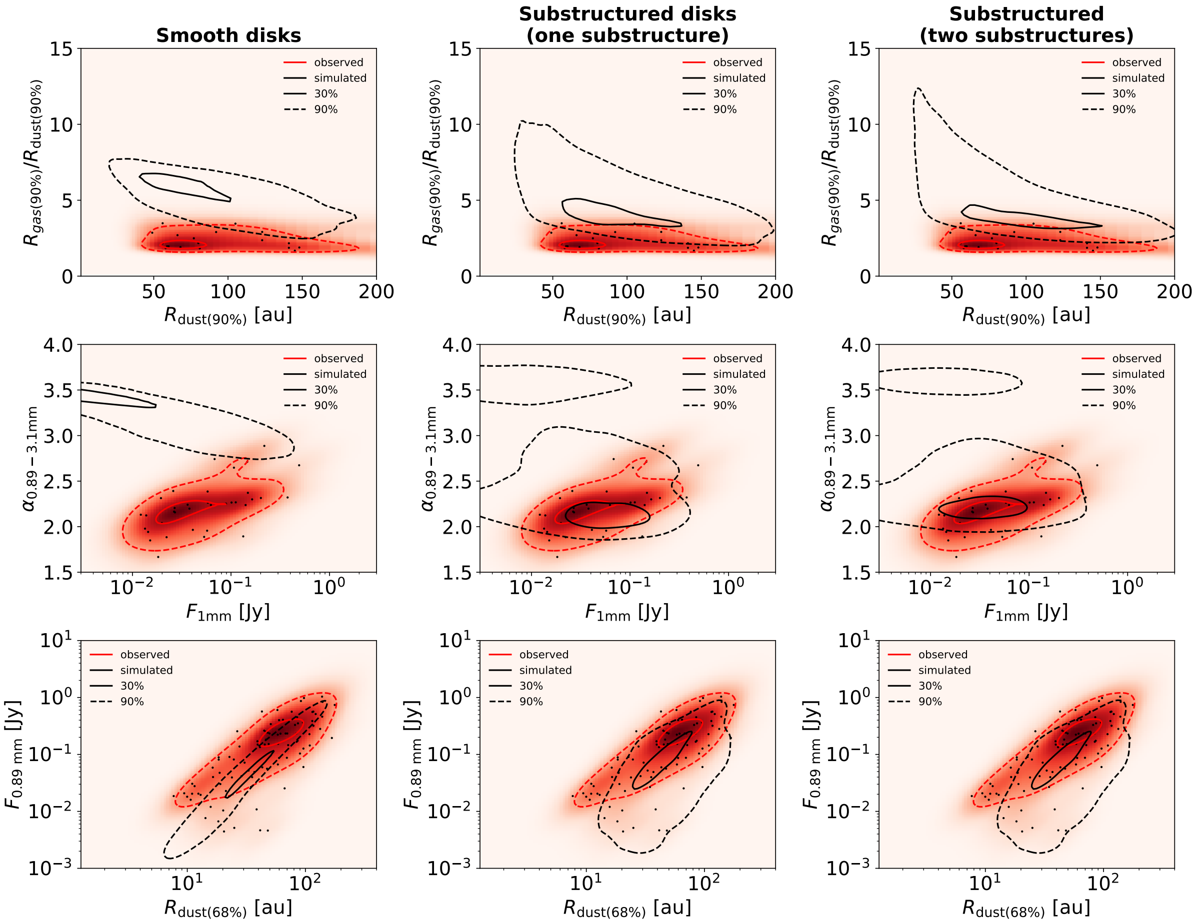

Figure 4.1: Gas-dust size distribution (first row), spectral index distribution (second row) and size-luminosity distribution (third row) for the parameter space of the initial conditions selecting disks with a spectral index $0 \leq \alpha_{0.89-3.1mm} \leq 4$, 10^{-3} Jy $\leq F_{1mm} \leq 10$ Jy, 10^{-3} Jy $\leq F_{0.89mm} \leq 10$ Jy, $10^{0.1}$ au $\leq R_{dust(68\%)} \leq 10^{2.6}$ au, 1 au $\leq R_{dust(90\%)} \leq 200$ au and $0.1 \leq R_{gas(90\%)}/R_{dust(90\%)} \leq 20$.
Left plots: smooth disks. Middle plots: sub-structured disks with one planet randomly inserted in a range between 0.1-0.4 Myr from the start of the disk evolution. Right plots: sub-structured disks with two planets randomly inserted in a range between 0.1-0.4 Myr (innermost planet) and between 0.5-0.8 Myr (outermost planet) from the start of the disk evolution.
Heatmap of the observed disks with the black dots representing each single observed disk. The black and red lines refer to the simulated results and the observational results respectively. In particular, the continuous lines encompass the 30% of the cumulative sum of the disks produced from the simulations or observed. The dashed lines encompass the 90% instead.

For completeness, Figure 4.1 also presents the spectral index and size-luminosity distributions associated with the three types of disks examined. As already shown in Delussu et al. (2024), only substructured disks are capable of producing spectral indices that populate the observed spectral index region. Therefore, Figure 4.1 illustrates how smooth disks fail to reproduce two of the three observed distributions examined. However, it also highlights a tension for substructured disks between the favorable results for the spectral index and size-luminosity distributions, which can be simultaneously reproduced by restricting the parameter space of the initial conditions of the simulated disks (Delussu et al. 2024), and the discrepancy between simulated and observed size distribution.

Figure 4.2 shows the distribution of $R_{\mathrm{gas}(90\%)}/R_{\mathrm{dust}(90\%)}$, confirming that the insertion of substructure(s) in the disk reduces the discrepancy between observation and simulation but doesn't completely address the problem.

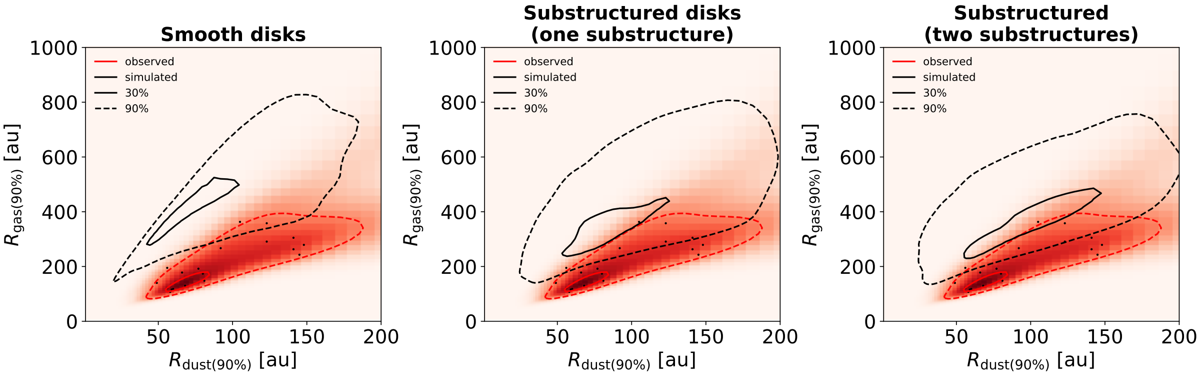

Figure 4.2: $R_{gas(90\%)}$ vs $R_{dust(90\%)}$ for the parameter space of the initial conditions selecting disks with a spectral index $0 \leq \alpha_{0.89-3.1mm} \leq 4$, $1 \times 10^{-3}\,\mathrm{Jy} \leq F_{1mm} \leq 10\,\mathrm{Jy}$, $1 \times 10^{-3}\,\mathrm{Jy} \leq F_{0.89mm} \leq 10\,\mathrm{Jy}$, $10^{0.1}\mathrm{au} \leq R_{dust(68\%)} \leq 10^{2.6}\mathrm{au}$, $1\,\mathrm{au} \leq R_{dust(90\%)} \leq 200\,\mathrm{au}$ and $0.1 \leq R_{gas(90\%)}/R_{dust(90\%)} \leq 20$.
Left plot: smooth disks. Middle plot: sub-structured disks with one planet randomly inserted in a range between 0.1-0.4 Myr from the start of the disk evolution. Right plot: sub-structured disks with two planets randomly inserted in a range between 0.1-0.4 Myr (innermost planet) and between 0.5-0.8 Myr (outermost planet) from the start of the disk evolution.
Heatmap of the observed disks with the black dots representing each single observed disk for the sample reported in Sanchis et al. (2021) for the Lupus region. The black and red lines refer to the simulated results and the observational results respectively. In particular, the continuous lines encompass the 30% of the cumulative sum of the disks produced from the simulations or observed. The dashed lines encompass the 90% instead.

4.3.2 DustPy and external photoevaporation results

Having determined that the mere presence of substructures in protoplanetary disks is insufficient to solve the size distribution problem, a further study was conducted to investigate whether external photoevaporation, in conjunction with substructures, may be the necessary ingredient to reconcile observations and simulations. Nevertheless, given that external photoevaporation is not yet available in two-pop-py, we switched from a population synthesis study to a study of a test population of disks conducted with DustPy where the effect of external photoevaporation is included in addition to viscous evolution. We assumed that the disks are exposed to a constant external FUV flux of 4 G_0, which corresponds to the average FUV flux experienced by disk-hosting stars in the Lupus star-forming region (Anania et al. 2025b). Figure 4.3 shows the behavior of some sub-structured test disks in the $R_{\rm gas(90\%)}/R_{\rm dust(90\%)}$ vs $R_{\rm dust(90\%)}$ space in the regime of low viscosity (i.e, $\alpha = 10^{-3.5}$):

- Disks hosted by a solar mass star evolve towards high ratios of $R_{\rm gas(90\%)}/R_{\rm dust(90\%)}$. The disk decreases in $R_{\rm dust(90\%)}$ rapidly settling to a fixed value corresponding to the location of the substructure; nevertheless, $R_{\rm gas(90\%)}/R_{\rm dust(90\%)}$ increases over time because these disks experience viscous spreading or just slightly reduces their $R_{gas(90\%)}$ due to a small effect of the external photoevaporation.

- Disks hosted by a star with $M_{\rm star} = 0.3\,{\rm M}_\odot$ and with a small characteristic radius $r_c = 20\,{\rm au}$ evolve towards high ratios of $R_{\rm gas(90\%)}/R_{\rm dust(90\%)}$ as they experience viscous spreading because their external photoevaporation truncation radius is placed too farther away ($\sim 100\,{\rm au}$) for impacting on disk evolution.

- Medium ($r_c = 50\,{\rm au}$) and large ($r_c = 100\,{\rm au}$) disks hosted by a star with $M_{\rm star} = 0.3\,{\rm M}_\odot$ evolve towards small ratios of $R_{\rm gas(90\%)}/R_{\rm dust(90\%)}$, falling close or inside the observed region.

Having established that small-size disks (i.e., $r_c = 20\,{\rm au}$) and disks hosted by a solar-mass star do not exhibit the desired behavior, we focused on medium (i.e., $r_c = 50\,{\rm au}$) and large (i.e., $r_c = 100\,{\rm au}$) disk size cases hosted by a star of mass $M_{star} = 0.3\,{\rm M}_\odot$. Figure 4.4 shows the impact of the external photoevaporation on the behavior of these disks. Disks completely revert their behavior in the absence of external photoevaporation moving towards high $R_{\rm gas(90\%)}/R_{\rm dust(90\%)}$ ratios as they experience viscous spreading in $R_{\rm gas(90\%)}$ in the absence of external photoevaporation. The first decrease in $R_{\rm gas(90\%)}/R_{\rm dust(90\%)}$ experienced by the disk with mass $M_{disk} = 0.01\,{\rm M}_{\rm star}$ and $r_c = 100\,{\rm au}$ is simply because $R_{\rm dust(90\%)}$ settles towards the location of the substructure which in this case happens to produce an increase in $R_{\rm dust(90\%)}$. However, also this disk is affected by spreading in $R_{\rm gas(90\%)}$, which combined with the stable $R_{\rm dust(90\%)}$ produced by the presence of the substructure leads to an increase of $R_{\rm gas(90\%)}/R_{\rm dust(90\%)}$ over time. Figure 4.5 and Figure 4.6 show an extension and in-depth investigation of our discussion focused on the disk cases that have proven so far successful in their behavior in the $R_{\rm gas(90\%)}/R_{\rm dust(90\%)}$ vs $R_{\rm dust(90\%)}$ space.

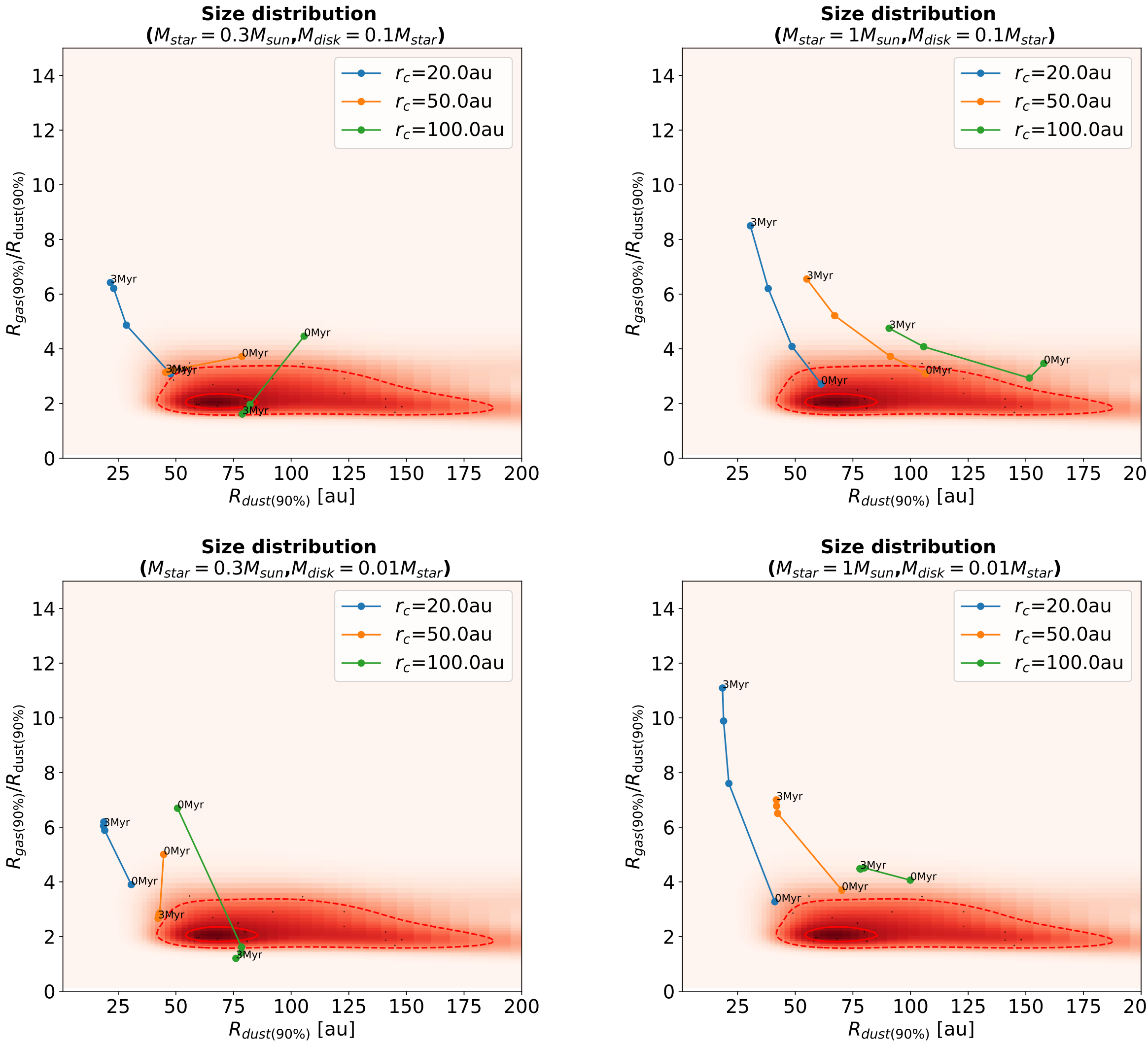

Figure 4.3: Evolution in the $R_{gas(90\%)}/R_{dust(90\%)}$ vs $R_{dust(90\%)}$ space for some test substructured disks evolved with DustPy code with external photoevaporation ($F_{FUV} = 4\mathrm{G}_0$) in a low viscosity regime ($\alpha = 10^{-3.5}$) for different values of the characteristic radius r_c. The points associated with each trajectory represent the snapshots taken at 0 Myr, 1 Myr, 2 Myr, and 3 Myr, respectively.
Heatmap of the observed disks with the black dots representing each single observed disk for the sample reported in Sanchis et al. (2021) for the Lupus region. The black and red lines refer to the simulated results and the observational results respectively. In particular, the continuous lines encompass the 30% of the cumulative sum of the disks produced from the simulations or observed. The dashed lines encompass the 90% instead.

- Figure 4.5 shows that medium disks (i.e., $r_c = 50\,\mathrm{au}$) experience a continuous reduction of their $R_{\mathrm{gas}(90\%)}/R_{\mathrm{dust}(90\%)}$ for all the substructures locations examined. However, if we extend our investigation to the behavior of these disks in the spectral

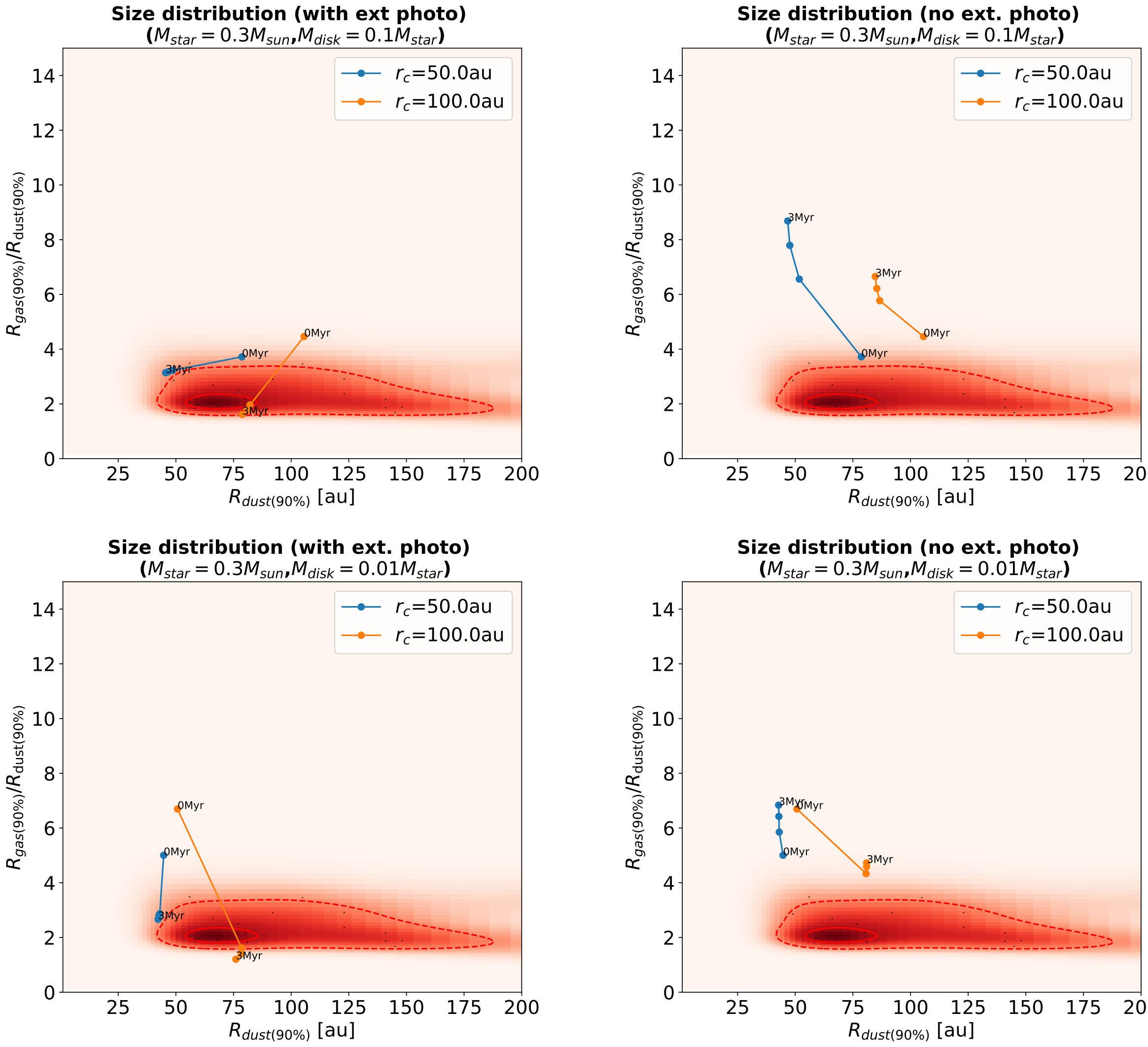

Figure 4.4: Evolution in the $R_{\text{gas}(90\%)}/R_{\text{dust}(90\%)}$ vs $R_{\text{dust}(90\%)}$ space for some test substructured disks evolved with DustPy code in a low viscosity regime ($\alpha = 10^{-3.5}$) for different values of the characteristic radius r_c. The points associated with each trajectory represent the snapshots taken at 0 Myr, 1 Myr, 2 Myr, and 3 Myr, respectively. Left plots: external photoevaporation ($F_{FUV} = 4\text{G}_0$). Right plots: no external photoevaporation. Heatmap of the observed disks with the black dots representing each single observed disk for the sample reported in Sanchis et al. (2021) for the Lupus region. The black and red lines refer to the simulated results and the observational results respectively. In particular, the continuous lines encompass the 30% of the cumulative sum of the disks produced from the simulations or observed. The dashed lines encompass the 90% instead.

index and size-luminosity space we immediately notice the emergence of some problems. All 'lighter' disks (i.e., with an $M_{disk} = 0.01\,\text{M}_{\text{star}}$) produce large values of spectral indexes and extremely low fluxes. The same problem is displayed by the more massive disks (i.e., with an $M_{disk} = 0.1\,\mathrm{M_{star}}$) if the substructure is placed at or beyond the characteristic radius. Nevertheless, placing the substructure too internal does not yield beneficial results, as demonstrated by the case $r_p = 0.5\,\mathrm{r_c}$. This configuration produces a smaller $R_{\mathrm{dust}(90\%)}$, which fails to sufficiently decrease the $R_{\mathrm{gas}(90\%)}/R_{\mathrm{dust}(90\%)}$ ratio.

- Figure 4.5 shows that if the substructure is placed at an intermediate position (i.e., $r_p = 0.7\,\mathrm{r_c}$) and $M_{\mathrm{disk}} = 0.1\,\mathrm{M_{star}}$, the disk behaves well in all the parameter space taken into account. Nevertheless, it introduces a warning that we may face and end up in a fine-tuning problem.

- Figure 4.6 shows that large disks (i.e., $r_c = 100\,\mathrm{au}$) experience a continuous reduction of their $R_{\mathrm{gas}(90\%)}/R_{\mathrm{dust}(90\%)}$ only in the case in which the substructure is placed at $r_p = 0.5\,\mathrm{r_c}$. Indeed, placing the substructure farther away causes it to be gradually removed by the external photoevaporation mechanism as it gets closer to the truncation radius location ($\sim 110\,\mathrm{au}$). Furthermore, the erosion of the substructure due to external photoevaporation translates into severe discrepancies with respect to the observed spectral indices and fluxes as these disks start to behave as smooth disks. Despite its good behavior in the size and size-luminosity space, the $r_p = 0.5\,\mathrm{r_c}$ fails to produce a spectral index in the observed range.

4.3.3 Possible solutions and future perspectives

While the population study conducted by Delussu et al. (2024) revealed that substructured disks can simultaneously reproduce the observed spectral index and size-luminosity distributions by imposing simple constraints on the parameter space of their initial conditions, both the population study performed with two-pop-py (Sec. 4.3.1) and the study on a test population conducted with DustPy in the presence of external photoevaporation (Sec. 4.3.2) exposed the difficulty in reproducing the observed ratios of $R_{\mathrm{gas}(90\%)}/R_{\mathrm{dust}(90\%)}$. The results obtained from both studies presented in the previous sections suggest that the discrepancy between simulations and observations may be linked to an incorrect estimate of the gas sizes of the disks. Indeed, the simulated dust radii align with the observed ones, while the simulated gas radii exceed the observed values. A combination of the mechanisms at play during the evolution of disks that prevent the production of large gas radii is thus needed. Since viscous evolution is causing the spreading of the disks, our results suggest that disks are either not evolving viscously or another mechanism is acting against the viscous spreading. External photoevaporation offers a means to counterbalance viscous expansion. However, external photoevaporation must be sufficiently strong to counteract viscous expansion and induce a reduction in the gas radius over time while also ensuring that the substructure is not eroded by its action. The results obtained demonstrate that it is possible to identify combinations of initial conditions under which disks undergoing viscous evolution, in conjunction with external photoevaporation, yield results consistent with the observed ones. However, the limited range of initial conditions required to achieve

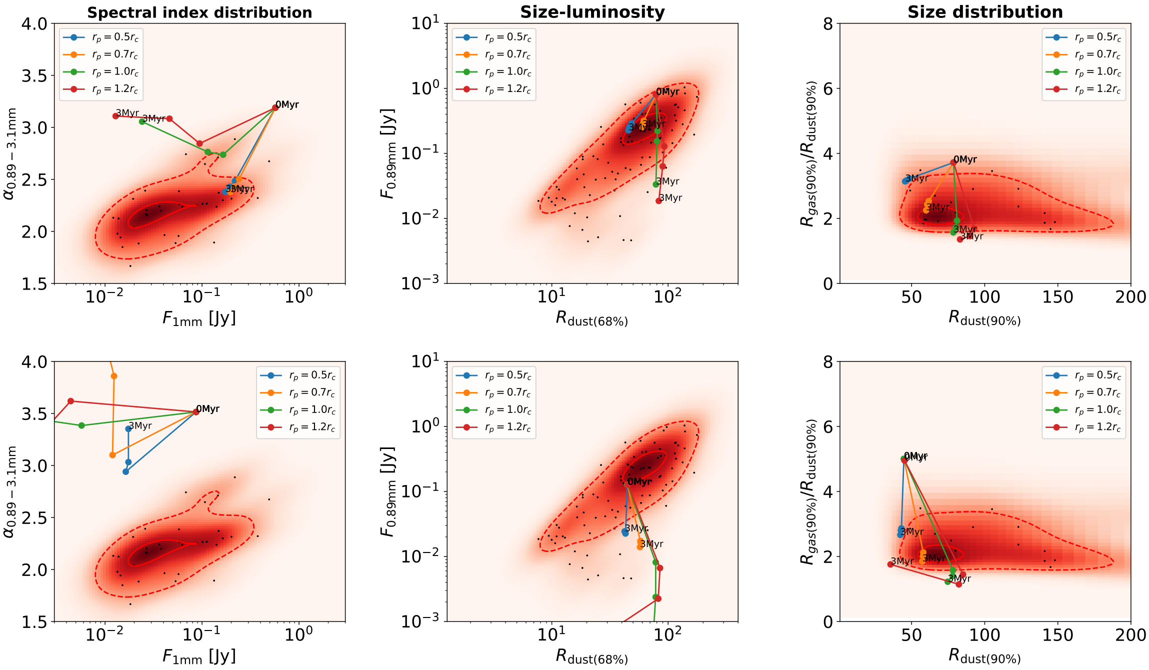

Figure 4.5: Evolution in the spectral index, size-luminosity, and $R_{\mathrm{gas}(90\%)}/R_{\mathrm{dust}(90\%)}$ vs $R_{\mathrm{dust}(90\%)}$ spaces of sub-structured disks evolved with DustPy code with external photoevaporation ($F_{FUV} = 4\mathrm{G}_0$). Low viscosity regime ($\alpha = 10^{-3.5}$) and disk characteristic radius fixed to $r_c = 50\,\mathrm{au}$. Different values of the position of the inserted substructure r_p have been explored. The points associated with each trajectory represent the snapshots taken at 0 Myr, 1 Myr, 2 Myr, and 3 Myr, respectively. Top row: $M_{disk} = 0.1\,\mathrm{M}_{\mathrm{star}}$. Bottom row: $M_{disk} = 0.01\,\mathrm{M}_{\mathrm{star}}$.
Heatmap of the observed disks with the black dots representing each single observed disk for the sample reported in Sanchis et al. (2021) for the Lupus region. The black and red lines refer to the simulated results and the observational results respectively. In particular, the continuous lines encompass the 30% of the cumulative sum of the disks produced from the simulations or observed. The dashed lines encompass the 90% instead.

such outcomes suggests that this result may be more akin to fine-tuning. If the mere introduction of external photoevaporation does not address the problem, it may be necessary to reconsider the assumptions underlying the adopted viscosity model. Could reducing the viscosity to values as low as 10^{-5} to mitigate viscous spread lead to the desired outcome? We plan to investigate this scenario in a future study by expanding the parameter space of the initial conditions. However, assuming such a low viscosity value could result in the formation of disks with very low fluxes and infinitely small rings. Nevertheless, if mixing occurs at the location of the substructure, a non-infinitesimal ring width can be preserved. Viscous evolution, which leads to large gas radii, might also be addressed by revisiting our assumption for the γ parameter. Indeed, as shown in Toci et al. (2021), reducing γ leads to a decrease in both the gas radius and the ratio of gas to dust radius. We intend to explore

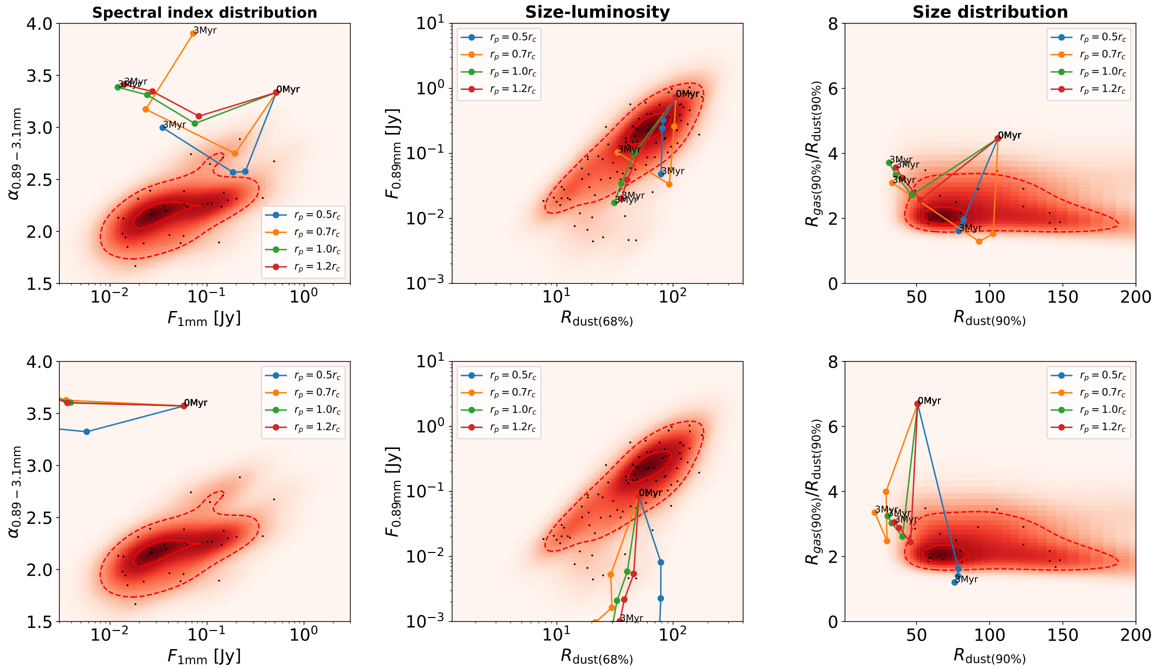

Figure 4.6: Same as Figure 4.5, but disks with characteristic radius fixed to $r_c = 100\,\mathrm{au}$.

this scenario in a future study by broadening the parameter space of the initial conditions.

An alternative option is to abandon the assumption that disks are driven by viscosity and instead assume that they are wind-driven. In contrast to purely viscous evolution, MHD winds extract angular momentum instead of exchanging it radially within the disk. This could drive disk evolution and accretion without spreading the disk, possibly keeping gas disk sizes small enough to fulfill observational constraints. This dust/gas radii discrepancy therefore may offer a way to constrain the relative contributions of viscous- and wind-like mechanisms but will require the implementation of an MHD wind parametrization (e.g. Tabone et al. 2022) into DustPy or two-pop-py which will be the subject of a future study.

4.4 Conclusions

In this work, we conducted a study to determine whether substructured disks can reproduce the observed gas-dust size distribution of protoplanetary disks. We first exploited the two-pop-py 1D evolutionary model for dust and gas in protoplanetary disks to perform a population synthesis study. Subsequently, we performed a study exploiting DustPy code integrated with an external module that includes the effect of an external FUV field to gain some insight into the dust-gas size behavior of disks undergoing external photoevaporation. We compared our simulated disks to the observed dust-gas size distribution of disks of the

Lupus star-forming presented in Sanchis et al. (2021). These are the main results we have outlined:

1. We confirmed that smooth disks produce a larger $R_{\mathrm{gas}(90\%)}/R_{\mathrm{dust}(90\%)}$ compared to observations (Fig. 4.1), extending Toci et al. (2021) result to the broader level of a disk population synthesis.
2. We proved, on a population synthesis level, that, as suggested by Toci et al. (2021), substructured disks, whether with one or two substructures, produce a size distribution shifted towards lower $R_{\mathrm{gas}(90\%)}/R_{\mathrm{dust}(90\%)}$ compared to smooth disks (Fig. 4.1). However, although the presence of substructures helps mitigate the discrepancy between simulation and observation, it does not completely resolve it.
3. We identified a tension for substructured disks between the favorable results presented in Delussu et al. (2024) for the spectral index and size-luminosity distributions, which can be simultaneously reproduced by restricting the initial condition parameter space, and the mismatch observed in the dust-gas size distribution (Fig. 4.1).
4. We found that even when accounting for external photoevaporation, reproducing the observed dust-to-gas size ratios remains challenging.
5. Disks hosted by a solar mass star evolve towards high ratios of $R_{\mathrm{gas}(90\%)}/R_{\mathrm{dust}(90\%)}$ (Fig. 4.3) because they undergo viscous spreading or experience only a slight reduction in $R_{\mathrm{gas}(90\%)}$ due to a small effect of the external photoevaporation.
6. Small-size disks (i.e., $r_c = 20\,\mathrm{au}$) evolve towards high ratios of $R_{\mathrm{gas}(90\%)}/R_{\mathrm{dust}(90\%)}$ (Fig. 4.3), regardless of the mass of the hosting star, as they undergo viscous spreading. This happens because their external photoevaporation truncation radius is placed too far away ($\sim 100\,\mathrm{au}$) for external photoevaporation to significantly affect disk evolution.
7. Medium ($r_c = 50\,\mathrm{au}$) and large ($r_c = 100\,\mathrm{au}$) disks hosted by a star with $M_{star} = 0.3\,\mathrm{M}_{\odot}$ due to the action of external photoevaporation evolve towards small ratios of $R_{\mathrm{gas}(90\%)}/R_{\mathrm{dust}(90\%)}$, falling close or inside the observed region (Fig. 4.4).
8. An in-depth investigation of medium-size disks ($r_c = 50\,\mathrm{au}$) (Fig. 4.5) showed that, except for the configuration in which the substructure is placed at $r_p = 0.7\,\mathrm{r_c}$ and $M_{\mathrm{disk}} = 0.1\,\mathrm{M_{star}}$, medium-size disks fail to simultaneously reproduce the spectral index, size-luminosity, and gas-dust size distributions. This result introduces a warning that we may face and end up in a fine-tuning problem.
9. An in-depth investigation of large-size disks ($r_c = 100\,\mathrm{au}$) (Fig. 4.6) revealed that, to reproduce the desired gas-dust size ratio, the substructure must be placed at a maximum distance of $r_p = 0.5\,\mathrm{r_c}$. Placing the substructure farther away results in its gradual removal by the external photoevaporation mechanism. However, all disks, including those with $r_p = 0.5\,\mathrm{r_c}$, fail to reproduce the spectral index and size-luminosity distributions.

10. The results obtained from both studies presented in the previous sections suggest that the discrepancy between simulations and observations may be linked to an incorrect estimate of the gas sizes of the disks. Indeed, the simulated dust radii align with the observed ones, while the simulated gas radii exceed the observed values.

Results suggest that the discrepancy between simulations and observations may stem from an inaccurate estimate of the gas sizes of the disks. Indeed, while simulated dust radii are consistent with the observed values, simulated gas radii exceed the observed ones. In future work, we aim to extend our investigation by broadening the parameter space of the initial conditions and exploring further scenarios such as wind-driven disks, lower viscosity values and reduced γ values.

Chapter 5

Conclusions and outlook

The study of protoplanetary disks has gained significant momentum in recent years, mainly driven by advancements in observational capabilities, such as new generations of infrared and high-contrast optical instruments, and particularly the advent of the Atacama Large Millimeter/Sub-Millimeter Array (ALMA). The protoplanetary disk field is currently experiencing a period of prosperity, carving out an increasingly important niche alongside well-established and popular fields such as stellar and planetary formation and evolution. This thesis presented two disk population synthesis studies that stem from two key developments made in recent years: the revolutionary discovery of substructures' presence and ubiquity in bright disks and the ever-increasing availability of large-sample surveys covering entire star-forming regions.

The study presented in Chapter 3 revealed the necessity of the presence and rapid formation (i.e., before 0.4 Myr) of significant substructures, as planets in the Saturn to few Jupiter-mass range would induce, in protoplanetary disks to reproduce the observed spectral index values. This result confirmed and, in particular, extended to the broader level of a disk population synthesis the findings of previous studies that had already shown the need for the presence of substructures to reproduce the observed spectral index values modeling individual disks. The study presented in Chapter 3 suggested that most "smooth" disks hide unresolved substructures. Furthermore, disks with relatively high initial masses ($10^{-2.3} M_\star \leqslant M_{disk} \leqslant 10^{-0.5} M_\star$), moderate levels of turbulence ($10^{-3.5} \leqslant \alpha \leqslant 10^{-2.5}$), and significant and early formed substructure proved to be capable of simultaneously reproducing the observed distributions for both the spectral index and size–luminosity. The study presented in Chapter 3 offered valuable insights into one of the main open problems in the protoplanetary disk field: what is the appropriate opacity model for protoplanetary disks? The study indicated that only opacities with high absorption efficiency can reproduce the observed spectral indices.

Building on the positive results obtained, a second study, presented in Chapter 4, expanded the first population synthesis study to investigate the possibility of reproducing an additional distribution: the gas and dust size ratios $R_{\mathrm{gas}}/R_{\mathrm{dust}}$ observed for disks of the Lupus star-forming region. Specifically, since previous studies have shown that smooth disks produce $R_{\mathrm{gas}}/R_{\mathrm{dust}}$ values larger than those observed, the possibility of substructured disks to address this discrepancy was explored. The study revealed that the introduction of substructure(s) reduces the discrepancy between simulations and observations by producing lower $R_{\mathrm{gas}}/R_{\mathrm{dust}}$ than smooth disks, nevertheless, it does not allow to fully address the problem as the estimated $R_{\mathrm{gas}}/R_{\mathrm{dust}}$ ratios for substructured disks still exceed the observed ones. Motivated by these results, a further investigation was conducted to assess whether external photoevaporation, combined with substructures, could be the key ingredient in reconciling observations with simulations. Nevertheless, since external photoevaporation is not yet implemented in the two-pop-py code exploited for performing a full population synthesis, the approach shifted from a population synthesis study to an analysis of a test population of disks conducted with the DustPy code, which includes the effects of external photoevaporation in addition to viscous evolution. The investigation showed that even when accounting for external photoevaporation, reproducing the observed $R_{\mathrm{gas}}/R_{\mathrm{dust}}$ ratios remains challenging. Indeed, only peculiar combinations of disks' initial conditions proved capable of producing $R_{\mathrm{gas}}/R_{\mathrm{dust}}$ ratios similar to the observed ones, introducing a warning that we may face and end up in a fine-tuning problem. This danger is further enhanced by the additional restriction on the combinations of disks' initial conditions that result if the observed spectral index and size-luminosity distributions are also to be reproduced. The results suggested that the discrepancy between simulations and observations may stem from an inaccurate estimation of the gas sizes in the disks. Indeed, the simulated dust radii align with the observed values, while the simulated gas radii exceed the observed ones. Therefore, a combination of the mechanisms at play during disk evolution that prevent the formation of large gas radii is needed. It is proposed to extend the investigation in future work by broadening the parameter space of the initial conditions and exploring additional scenarios, such as wind-driven disks.

5.1 Future work

5.1.1 From disk population synthesis models toward planet-disk population synthesis models

Disk population synthesis, which is increasingly gaining popularity and relevance in the protoplanetary disk field, proved as a precious tool for investigating and constraining parameters and initial conditions of planet-forming disks. As demonstrated by the studies presented in this thesis, the task of reproducing observed distributions becomes increasingly complex as the number of distributions examined grows, rapidly leading to the possibility of facing and ending up in a fine-tuning problem. This suggests the necessity to refine the adopted disk evolution model and/or incorporate additional physical mechanisms within it. The development of a comprehensive disk evolution model, namely a computational model accounting for all the physical mechanisms at play during the evolution of protoplanetary disks, may, therefore, not be merely a request for the sake of completeness, but a genuine necessity.

In future work, it is proposed to investigate the wind-driven scenario and expand the two-pop-py code to include external photoevaporation, planet migration, and the effects of planetesimal formation and pebble accretion; with the ultimate goal of creating a comprehensive planet and disk population synthesis, ranging from micron-sized dust particles to the final formation of planets. Creating such a comprehensive model inevitably represents a challenge in terms of computational costs as the inclusion of more mechanisms generally leads to a higher computational cost. Addressing this challenge will be critical for the future advancement of disk population synthesis studies.

5.1.2 Machine Learning and disk population synthesis

Machine learning (ML) is rapidly spreading and making a significant impact across all fields of society, including science, where it is advancing research and transforming the way scientific problems are approached and solved. One of the main applications of machine learning (ML) in the scientific field is data analysis and pattern recognition. ML algorithms can efficiently analyze massive datasets and identify patterns with remarkable speed, making them ideally suited for potentially highly impactful applications in disk population synthesis studies.

The ML-disk population synthesis approach can also be exploited in the opposite direction. Simulated disk populations can be fed to train ML algorithms to make predictions, for example, about disk observables. An ongoing study, which will be published as *Stammler, Delussu, and Birnstiel*, uses machine learning techniques to enhance the accuracy of gas and dust mass estimations for protoplanetary disks, demonstrating that training a self-normalizing neural network a significant improvement over the traditional method adopted to estimate disk masses (see Section 1.4.1) can be achieved.

Bibliography

Adams, F. C., Hollenbach, D., Laughlin, G., & Gorti, U. 2004, , 611, 360

Adams, F. C., Lada, C. J., & Shu, F. H. 1987, Astrophysical Journal, Part 1 (ISSN 0004-637X), vol. 312, Jan. 15, 1987, p. 788-806. NASA-supported research., 312, 788

Aikawa, Y. & Nomura, H. 2006, The Astrophysical Journal, 642, 1152

Aikawa, Y., Van Zadelhoff, G., van Dishoeck, E. F., & Herbst, E. 2002, Astronomy & Astrophysics, 386, 622

Akiyama, E., Hashimoto, J., baobabu Liu, H., et al. 2016, The Astronomical Journal, 152, 222

ALMA Partnership, Brogan, C. L., Pérez, L. M., et al. 2015, , 808, L3

Anania, R., Rosotti, G., Gárate, M., et al. 2025a,

Anania, R., Winter, A. J., Rosotti, G., et al. 2025b, arXiv e-prints, arXiv:2501.18752

Andama, G., Ndugu, N., Anguma, S. K., & Jurua, E. 2022, Monthly Notices of the Royal Astronomical Society, 512, 5278

Andrews, S. M. 2020, Annual Review of Astronomy and Astrophysics, 58, 483

Andrews, S. M., Huang, J., Pérez, L. M., et al. 2018a, , 869, L41

Andrews, S. M., Rosenfeld, K. A., Kraus, A. L., & Wilner, D. J. 2013, The Astrophysical Journal, 771, 129

Andrews, S. M., Terrell, M., Tripathi, A., et al. 2018b, , 865, 157

Andrews, S. M., Wilner, D. J., Zhu, Z., et al. 2016, The Astrophysical Journal Letters, 820, L40

Ansdell, M., Haworth, T. J., Williams, J. P., et al. 2020, The Astronomical Journal, 160, 248

Ansdell, M., Williams, J., Trapman, L., et al. 2018, The Astrophysical Journal, 859, 21

Ansdell, M., Williams, J. P., Manara, C. F., et al. 2017, The Astronomical Journal, 153, 240

Ansdell, M., Williams, J. P., van der Marel, N., et al. 2016, The Astrophysical Journal, 828, 46

Arlt, R. & Urpin, V. 2004, Astronomy & Astrophysics, 426, 755

Bae, J., Hartmann, L., & Zhu, Z. 2015, The Astrophysical Journal, 805, 15

Bae, J., Hartmann, L., Zhu, Z., & Nelson, R. P. 2014, The Astrophysical Journal, 795, 61

Bae, J., Isella, A., Zhu, Z., et al. 2022, arXiv preprint arXiv:2210.13314

Bae, J., Isella, A., Zhu, Z., et al. 2023, Structured Distributions of Gas and Solids in Protoplanetary Disks

Bae, J. & Zhu, Z. 2018a, The Astrophysical Journal, 859, 118

Bae, J. & Zhu, Z. 2018b, The Astrophysical Journal, 859, 119

Bae, J., Zhu, Z., & Hartmann, L. 2016, The Astrophysical Journal, 819, 134

Bae, J., Zhu, Z., & Hartmann, L. 2017, The Astrophysical Journal, 850, 201

Bai, X.-N. & Stone, J. M. 2013, The Astrophysical Journal, 769, 76

Bai, X.-N. & Stone, J. M. 2014, , 796, 31

Balbus, S. A. & Hawley, J. F. 1991, Astrophysical Journal, Part 1 (ISSN 0004-637X), vol. 376, July 20, 1991, p. 214-233., 376, 214

Barenfeld, S. A., Carpenter, J. M., Ricci, L., & Isella, A. 2016, The Astrophysical Journal, 827, 142

Barranco, J. A. & Marcus, P. S. 2005, The Astrophysical Journal, 623, 1157

Barraza-Alfaro, M., Flock, M., Marino, S., & Pérez, S. 2021, Astronomy & Astrophysics, 653, A113

Bary, J. S., Weintraub, D. A., Shukla, S. J., Leisenring, J. M., & Kastner, J. H. 2008, The Astrophysical Journal, 678, 1088

Beckwith, S., Sargent, A., Scoville, N., et al. 1986, Astrophysical Journal, Part 1 (ISSN 0004-637X), vol. 309, Oct. 15, 1986, p. 755-761. Research supported by the Sloan Foundation., 309, 755

Beckwith, S. V., Sargent, A. I., Chini, R. S., & Guesten, R. 1990, Astronomical Journal (ISSN 0004-6256), vol. 99, March 1990, p. 924-945. Research supported by the Max-Planck-Gesellschaft zur Foerderung der Wissenschaften., 99, 924

Bergin, E. A. & Williams, J. P. 2017, Formation, evolution, and dynamics of young solar systems, 1

Béthune, W., Lesur, G., & Ferreira, J. 2017, Astronomy & Astrophysics, 600, A75

Birnstiel, T., Andrews, S. M., Pinilla, P., & Kama, M. 2015, The Astrophysical Journal Letters, 813, L14

Birnstiel, T., Dullemond, C., & Brauer, F. 2009, Astronomy & Astrophysics, 503, L5

Birnstiel, T., Dullemond, C. P., & Brauer, F. 2010a, , 513, A79

Birnstiel, T., Dullemond, C. P., Zhu, Z., et al. 2018, , 869, L45

Birnstiel, T., Klahr, H., & Ercolano, B. 2012, Astronomy & Astrophysics, 539, A148

Birnstiel, T., Ricci, L., Trotta, F., et al. 2010b, , 516, L14

Bitsch, B., Izidoro, A., Johansen, A., et al. 2019, Astronomy & Astrophysics, 623, A88

Blandford, R. D. & Payne, D. 1982, Monthly Notices of the Royal Astronomical Society, 199, 883

Blum, J. 2018, Space Science Reviews, 214, 52

Blum, J. & Wurm, G. 2008, Annu. Rev. Astron. Astrophys., 46, 21

Boehler, Y., Ricci, L., Weaver, E., et al. 2018, The Astrophysical Journal, 853, 162

Boss, A. P. 1997, Science, 276, 1836

Bruzual, G. & Charlot, S. 2003, Monthly Notices of the Royal Astronomical Society, 344, 1000

Burn, R., Emsenhuber, A., Weder, J., et al. 2022, Astronomy & Astrophysics, 666, A73

Calahan, J. K., Bergin, E., Zhang, K., et al. 2021, The Astrophysical Journal, 908, 8

Carmona, A., van Den Ancker, M., Henning, T., et al. 2008, Astronomy & Astrophysics, 477, 839

Carrasco-González, C., Sierra, A., Flock, M., et al. 2019, The Astrophysical Journal, 883, 71

Cazzoletti, P., Manara, C., Liu, H. B., et al. 2019, Astronomy & Astrophysics, 626, A11

Chabrier, G. 2003, Publications of the Astronomical Society of the Pacific, 115, 763

Cieza, L. A., Ruíz-Rodríguez, D., Hales, A., et al. 2019, Monthly Notices of the Royal Astronomical Society, 482, 698

Cimerman, N. P. & Rafikov, R. R. 2021, Monthly Notices of the Royal Astronomical Society, 508, 2329

Clarke, C. J. 2007, Monthly Notices of the Royal Astronomical Society, 376, 1350

Coleman, G. A. & Nelson, R. P. 2016, Monthly Notices of the Royal Astronomical Society, 460, 2779

Cossins, P., Lodato, G., & Clarke, C. 2009, Monthly Notices of the Royal Astronomical Society, 393, 1157

Cuello, N., Dipierro, G., Mentiplay, D., et al. 2019, Monthly Notices of the Royal Astronomical Society, 483, 4114

Cuello, N., Louvet, F., Mentiplay, D., et al. 2020, Monthly Notices of the Royal Astronomical Society, 491, 504

D'Alessio, P., Calvet, N., Hartmann, L., Franco-Hernández, R., & Servín, H. 2006, , 638, 314

Delussu, L., Birnstiel, T., Miotello, A., et al. 2024, arXiv preprint arXiv:2405.14501

Dong, R., Li, S., Chiang, E., & Li, H. 2017, The Astrophysical Journal, 843, 127

Dong, R., Li, S., Chiang, E., & Li, H. 2018, The Astrophysical Journal, 866, 110

Draine, B. 2006, The Astrophysical Journal, 636, 1114

Drążkowska, J. & Alibert, Y. 2017, Astronomy & Astrophysics, 608, A92

Drążkowska, J., Alibert, Y., & Moore, B. 2016, Astronomy & Astrophysics, 594, A105

Duffell, P. C. & MacFadyen, A. I. 2013, The Astrophysical Journal, 769, 41

Emsenhuber, A., Burn, R., Weder, J., et al. 2023a, Astronomy & Astrophysics, 673, A78

Emsenhuber, A., Mordasini, C., & Burn, R. 2023b, The European Physical Journal Plus, 138, 181

Epstein, P. S. 1924, Physical Review, 23, 710

Espaillat, C., Muzerolle, J., Najita, J., et al. 2014, arXiv preprint arXiv:1402.7103

Facchini, S., Clarke, C. J., & Bisbas, T. G. 2016, , 457, 3593

Flaherty, K. M., Hughes, A. M., Rose, S. C., et al. 2017, The Astrophysical Journal, 843, 150

Flaherty, K. M., Hughes, A. M., Teague, R., et al. 2018, The Astrophysical Journal, 856, 117

Flock, M., Fromang, S., Turner, N., & Benisty, M. 2016, The Astrophysical Journal, 827, 144

Flock, M., Fromang, S., Turner, N., & Benisty, M. 2017a, The Astrophysical Journal, 835, 230

Flock, M., Nelson, R. P., Turner, N. J., et al. 2017b, The Astrophysical Journal, 850, 131

Flock, M., Ruge, J. P., Dzyurkevich, N., et al. 2015, Astronomy & Astrophysics, 574, A68

Flock, M., Turner, N. J., Mulders, G. D., et al. 2019, Astronomy & Astrophysics, 630, A147

Flock, M., Turner, N. J., Nelson, R. P., et al. 2020, The Astrophysical Journal, 897, 155

Gammie, C. F. 2001, The Astrophysical Journal, 553, 174

Gárate, M., Delage, T. N., Stadler, J., et al. 2021, Astronomy & Astrophysics, 655, A18

Gárate, M., Pinilla, P., Haworth, T. J., & Facchini, S. 2024, , 681, A84

Garrod, R. T. & Herbst, E. 2006, Astronomy & Astrophysics, 457, 927

Garufi, A., Quanz, S. P., Schmid, H. M., et al. 2016, Astronomy & Astrophysics, 588, A8

Ginski, C., Tazaki, R., Dominik, C., & Stolker, T. 2023, The Astrophysical Journal, 953, 92

Gonzalez, J.-F., Laibe, G., & Maddison, S. T. 2017, Monthly Notices of the Royal Astronomical Society, 467, 1984

Goodman, J. & Rafikov, R. 2001, The Astrophysical Journal, 552, 793

Guidi, G., Isella, A., Testi, L., et al. 2022, Astronomy & Astrophysics, 664, A137

Gundlach, B., Kilias, S., Beitz, E., & Blum, J. 2011, Icarus, 214, 717

Hawley, J. F. 2001, The Astrophysical Journal, 554, 534

Haworth, T. J., Coleman, G. A. L., Qiao, L., Sellek, A. D., & Askari, K. 2023, arXiv e-prints, arXiv:2310.03097

Hendler, N., Pascucci, I., Pinilla, P., et al. 2020, The Astrophysical Journal, 895, 126

Hildebrand, R. H. 1983, The determination of cloud masses and dust characteristics from submillimetre thermal emission, Tech. rep.

Huang, J., Andrews, S. M., Cleeves, L. I., et al. 2018, The Astrophysical Journal, 852, 122

Huang, J., Andrews, S. M., Dullemond, C. P., et al. 2018, , 869, L42

Hyodo, R., Ida, S., & Charnoz, S. 2019, Astronomy & Astrophysics, 629, A90

Ida, S. & Guillot, T. 2016, Astronomy & Astrophysics, 596, L3

Isella, A., Huang, J., Andrews, S. M., et al. 2018, The Astrophysical Journal Letters, 869, L49

Izquierdo, A. F., Facchini, S., Rosotti, G. P., van Dishoeck, E. F., & Testi, L. 2022, The Astrophysical Journal, 928, 2

Jacquemin-Ide, J., Lesur, G., & Ferreira, J. 2021, Astronomy & Astrophysics, 647, A192

Johansen, A. & Youdin, A. 2007, The Astrophysical Journal, 662, 627

Johansen, A., Youdin, A., & Klahr, H. 2009, , 697, 1269

Kama, M., Bruderer, S., Van Dishoeck, E., et al. 2016, Astronomy & Astrophysics, 592, A83

Kamp, I., Thi, W.-F., Woitke, P., et al. 2017, Astronomy & Astrophysics, 607, A41

Kanagawa, K. D., Muto, T., Tanaka, H., et al. 2015a, The Astrophysical Journal Letters, 806, L15

Kanagawa, K. D., Muto, T., Tanaka, H., et al. 2016, Publications of the Astronomical Society of Japan, 68, 43

Kanagawa, K. D., Tanaka, H., Muto, T., Tanigawa, T., & Takeuchi, T. 2015b, Monthly Notices of the Royal Astronomical Society, 448, 994

Kataoka, A., Muto, T., Momose, M., et al. 2015, The Astrophysical Journal, 809, 78

Kataoka, A., Tsukagoshi, T., Momose, M., et al. 2016, The Astrophysical Journal Letters, 831, L12

Kataoka, A., Tsukagoshi, T., Pohl, A., et al. 2017, The Astrophysical Journal Letters, 844, L5

Kelly, B. C. 2007, The Astrophysical Journal, 665, 1489

Kenyon, S. J., Yi, I., & Hartmann, L. 1996, The Astrophysical Journal, 462, 439

Keppler, M., Benisty, M., Müller, A., et al. 2018, , 617, A44

Klahr, H. & Hubbard, A. 2014, The Astrophysical Journal, 788, 21

Kley, W. & Nelson, R. 2012, Annual Review of Astronomy and Astrophysics, 50, 211

Kraus, S., Kreplin, A., Fukugawa, M., et al. 2017, The Astrophysical Journal Letters, 848, L11

Krijt, S., Ormel, C. W., Dominik, C., & Tielens, A. G. 2015, Astronomy & Astrophysics, 574, A83

Kroupa, P. 2001, Monthly Notices of the Royal Astronomical Society, 322, 231

Kroupa, P. 2002, Science, 295, 82

Kunz, M. W. & Lesur, G. 2013, Monthly Notices of the Royal Astronomical Society, 434, 2295

Kuznetsova, A., Bae, J., Hartmann, L., & Mac Low, M.-M. 2022, The Astrophysical Journal, 928, 92

Lada, C. J. & Wilking, B. A. 1984, Astrophysical Journal, Part 1 (ISSN 0004-637X), vol. 287, Dec. 15, 1984, p. 610-621., 287, 610

Lau, T. C. H., Drążkowska, J., Stammler, S. M., Birnstiel, T., & Dullemond, C. P. 2022, Astronomy & Astrophysics, 668, A170

Lau, T. C. H., Lee, M. H., Brasser, R., & Matsumura, S. 2024, Astronomy & Astrophysics, 683, A204

Lesur, G., Hennebelle, P., & Fromang, S. 2015, Astronomy & Astrophysics, 582, L9

Li, H., Finn, J., Lovelace, R., & Colgate, S. 2000, The Astrophysical Journal, 533, 1023

Li, R., Youdin, A. N., & Simon, J. B. 2018, The Astrophysical Journal, 862, 14

Lin, D. N. & Papaloizou, J. 1979, Monthly Notices of the Royal Astronomical Society, 186, 799

Lin, M.-K. 2014, Monthly Notices of the Royal Astronomical Society, 437, 575

Lin, M.-K. & Papaloizou, J. C. 2011, Monthly Notices of the Royal Astronomical Society, 415, 1426

Long, F., Andrews, S. M., Rosotti, G., et al. 2022, The Astrophysical Journal, 931, 6

Long, F., Herczeg, G. J., Harsono, D., et al. 2019, The Astrophysical Journal, 882, 49

Long, F., Pinilla, P., Herczeg, G. J., et al. 2018, , 869, 17

Loomis, R. A., Öberg, K. I., Andrews, S. M., & MacGregor, M. A. 2017, The Astrophysical Journal, 840, 23

Lovelace, R. & Hohlfeld, R. 2013, Monthly Notices of the Royal Astronomical Society, 429, 529

Lovelace, R., Li, H., Colgate, S., & Nelson, A. 1999, The Astrophysical Journal, 513, 805

Lüst, R. 1952, Zeitschrift Naturforschung Teil A, 7, 87

Lynden-Bell, D. & Pringle, J. E. 1974, Monthly Notices of the Royal Astronomical Society, 168, 603

Lynden-Bell, D. & Pringle, J. E. 1974, , 168, 603

Lyra, W. 2014, The Astrophysical Journal, 789, 77

Lyra, W., Turner, N., & McNally, C. 2015, Astronomy & Astrophysics, 574, A10

Lyra, W. & Umurhan, O. M. 2019, Publications of the Astronomical Society of the Pacific, 131, 072001

Malygin, M., Klahr, H., Semenov, D., Henning, T., & Dullemond, C. 2017, Astronomy & Astrophysics, 605, A30

Manara, C., Rosotti, G., Testi, L., et al. 2016, Astronomy & Astrophysics, 591, L3

Manara, C. F., Ansdell, M., Rosotti, G. P., et al. 2023, in Astronomical Society of the Pacific Conference Series, Vol. 534, Protostars and Planets VII, ed. S. Inutsuka, Y. Aikawa, T. Muto, K. Tomida, & M. Tamura, 539

Marcus, P. S., Pei, S., Jiang, C.-H., & Barranco, J. A. 2016, The Astrophysical Journal, 833, 148

Marcus, P. S., Pei, S., Jiang, C.-H., et al. 2015, The Astrophysical Journal, 808, 87

Maschberger, T. 2013, Monthly Notices of the Royal Astronomical Society, 429, 1725

Miotello, A., Bruderer, S., & van Dishoeck, E. F. 2014, Astronomy & Astrophysics, 572, A96

Miotello, A., Kamp, I., Birnstiel, T., Cleeves, L., & Kataoka, A. 2023, in Astronomical Society of the Pacific Conference Series, Vol. 534, 501

Miranda, R., Li, H., Li, S., & Jin, S. 2017, The Astrophysical Journal, 835, 118

Miranda, R. & Rafikov, R. R. 2019, The Astrophysical Journal, 875, 37

Miyake, K. & Nakagawa, Y. 1993, icarus, 106, 20

Monnier, J. D., Harries, T. J., Bae, J., et al. 2019, The Astrophysical Journal, 872, 122

Morbidelli, A. 2020, Astronomy & Astrophysics, 638, A1

Mordasini, C. 2018, arXiv preprint arXiv:1804.01532

Mordasini, C., Alibert, Y., Georgy, C., et al. 2012, Astronomy & Astrophysics, 547, A112

Müller, A., Keppler, M., Henning, T., et al. 2018, , 617, L2

Musiolik, G. & Wurm, G. 2019, The Astrophysical Journal, 873, 58

Nakagawa, Y., Sekiya, M., & Hayashi, C. 1986, Icarus, 67, 375

Natta, A., Testi, L., Johnstone, D., et al. 2004, in ASP Conf. Proc., Vol. 323, 279

Nelson, R. P., Gressel, O., & Umurhan, O. M. 2013, Monthly Notices of the Royal Astronomical Society, 435, 2610

Okuzumi, S., Momose, M., Sirono, S.-i., Kobayashi, H., & Tanaka, H. 2016, , 821, 82

Okuzumi, S. & Tazaki, R. 2019, The Astrophysical Journal, 878, 132

Paardekooper, S. J. & Mellema, G. 2004, , 425, L9

Pascucci, I., Herczeg, G., Carr, J., & Bruderer, S. 2013, The Astrophysical Journal, 779, 178

Pascucci, I., Testi, L., Herczeg, G. J., et al. 2016, The Astrophysical Journal, 831, 125

Pérez, L. M., Carpenter, J. M., Andrews, S. M., et al. 2016, Science, 353, 1519

Pfeil, T. & Klahr, H. 2019, The Astrophysical Journal, 871, 150

Pierens, A. & Lin, M.-K. 2018, Monthly Notices of the Royal Astronomical Society, 479, 4878

Pinilla, P., Benisty, M., & Birnstiel, T. 2012, , 545, A81

Pinilla, P., Birnstiel, T., Benisty, M., et al. 2013, Astronomy & Astrophysics, 554, A95

Pinilla, P., Birnstiel, T., Ricci, L., et al. 2012, Astronomy & Astrophysics, 538, A114

Pinilla, P., Pascucci, I., & Marino, S. 2020, Astronomy & Astrophysics, 635, A105

Pinilla, P., Pohl, A., Stammler, S., & Birnstiel, T. 2017, The Astrophysical Journal, 845, 68

Pinilla, P., Pohl, A., Stammler, S. M., & Birnstiel, T. 2017, , 845, 68

Pinte, C., Price, D. J., Ménard, F., et al. 2018, , 860, L13

Pollack, J. B., Hollenbach, D., Beckwith, S., et al. 1994, , 421, 615

Pollack, J. B., Hubickyj, O., Bodenheimer, P., et al. 1996, Icarus, Vol. 124, Issue 1, p. 62-85

Powell, D., Murray-Clay, R., Pérez, L. M., Schlichting, H. E., & Rosenthal, M. 2019, The Astrophysical Journal, 878, 116

Pringle, J. E. 1981, In: Annual review of astronomy and astrophysics. Volume 19.(A82-11551 02-90) Palo Alto, CA, Annual Reviews, Inc., 1981, p. 137-162., 19, 137

Pérez, L. M., Benisty, M., Andrews, S. M., et al. 2018, The Astrophysical Journal Letters, 869, L50

Raettig, N., Lyra, W., & Klahr, H. 2021, The Astrophysical Journal, 913, 92

Rafikov, R. 2002, The Astrophysical Journal, 569, 997

Ragusa, E., Dipierro, G., Lodato, G., Laibe, G., & Price, D. J. 2017, , 464, 1449

Ricci, L., Testi, L., Natta, A., & Brooks, K. 2010a, Astronomy & Astrophysics, 521, A66

Ricci, L., Testi, L., Natta, A., et al. 2010b, Astronomy & Astrophysics, 512, A15

Ricci, L., Testi, L., Natta, A., et al. 2014, The Astrophysical Journal, 791, 20

Rice, W. K. M., Armitage, P. J., Wood, K., & Lodato, G. 2006, , 373, 1619

Richard, S., Nelson, R. P., & Umurhan, O. M. 2016, Monthly Notices of the Royal Astronomical Society, 456, 3571

Riols, A. & Lesur, G. 2019, Astronomy & Astrophysics, 625, A108

Rodmann, J., Henning, T., Chandler, C., Mundy, L., & Wilner, D. 2006, Astronomy & Astrophysics, 446, 211

Rosotti, G. P., Booth, R. A., Tazzari, M., et al. 2019a, , 486, L63

Rosotti, G. P., Tazzari, M., Booth, R. A., et al. 2019b, Monthly Notices of the Royal Astronomical Society, 486, 4829

Sanchis, E., Testi, L., Natta, A., et al. 2021, Astronomy & Astrophysics, 649, A19

Sanchis, E., Testi, L., Natta, A., et al. 2020, Astronomy & Astrophysics, 633, A114

Savvidou, S. & Bitsch, B. 2023, Astronomy & Astrophysics, 679, A42

Seizinger, A. & Kley, W. 2013, Astronomy & Astrophysics, 551, A65

Sellek, A. D., Booth, R. A., & Clarke, C. J. 2020, , 492, 1279

Shakura, N. I. & Sunyaev, R. A. 1973, Astronomy and Astrophysics, Vol. 24, p. 337-355, 24, 337

Shi, J.-M., Krolik, J. H., Lubow, S. H., & Hawley, J. F. 2012, , 749, 118

Siess, L., Dufour, E., & Forestini, M. 2000, arXiv preprint astro-ph/0003477

Somigliana, A., Testi, L., Rosotti, G., et al. 2024, Astronomy & Astrophysics, 689, A285

Somigliana, A., Testi, L., Rosotti, G., et al. 2023, The Astrophysical Journal Letters, 954, L13

Somigliana, A., Toci, C., Rosotti, G., et al. 2022, Monthly Notices of the Royal Astronomical Society, 514, 5927

Stadler, J., Gárate, M., Pinilla, P., et al. 2022, Astronomy & Astrophysics, 668, A104

Stammler, S. M. & Birnstiel, T. 2022, The Astrophysical Journal, 935, 35

Stammler, S. M., Birnstiel, T., Panić, O., Dullemond, C. P., & Dominik, C. 2017, Astronomy & Astrophysics, 600, A140

Stewart, S. T. & Leinhardt, Z. M. 2009, The Astrophysical Journal, 691, L133

Stokes, G. G. et al. 1851

Suzuki, T. K. & Inutsuka, S.-i. 2014, The Astrophysical Journal, 784, 121

Suzuki, T. K., Ogihara, M., Morbidelli, A., Crida, A., & Guillot, T. 2016, Astronomy & Astrophysics, 596, A74

Tabone, B., Rosotti, G. P., Cridland, A. J., Armitage, P. J., & Lodato, G. 2022, , 512, 2290

Tabone, B., Rosotti, G. P., Lodato, G., et al. 2022, Monthly Notices of the Royal Astronomical Society: Letters, 512, L74

Takahashi, S. Z. & Inutsuka, S.-i. 2014, The Astrophysical Journal, 794, 55

Takahashi, S. Z. & Muto, T. 2018, The Astrophysical Journal, 865, 102

Takeuchi, T. & Lin, D. 2002, The Astrophysical Journal, 581, 1344

Takeuchi, T. & Lin, D. 2005, The Astrophysical Journal, 623, 482

Tazzari, M., Clarke, C. J., Testi, L., et al. 2021a, , 506, 2804

Tazzari, M., Testi, L., Natta, A., et al. 2021b, Monthly Notices of the Royal Astronomical Society, 506, 5117

Teague, R., Bae, J., & Bergin, E. A. 2019, Nature, 574, 378

Teague, R., Bae, J., Bergin, E. A., Birnstiel, T., & Foreman-Mackey, D. 2018, , 860, L12

Teague, R., Guilloteau, S., Semenov, D., et al. 2016, Astronomy & Astrophysics, 592, A49

Teiser, J. & Wurm, G. 2009, Monthly Notices of the Royal Astronomical Society, 393, 1584

Testi, L., Natta, A., Scholz, A., et al. 2016, Astronomy & Astrophysics, 593, A111

Toci, C., Lodato, G., Livio, F. G., Rosotti, G., & Trapman, L. 2023, Monthly Notices of the Royal Astronomical Society: Letters, 518, L69

Toci, C., Rosotti, G., Lodato, G., Testi, L., & Trapman, L. 2021, Monthly Notices of the Royal Astronomical Society, 507, 818

Tominaga, R. T., Takahashi, S. Z., & Inutsuka, S.-i. 2019, The Astrophysical Journal, 881, 53

Toomre, A. 1964, Astrophysical Journal, vol. 139, p. 1217-1238 (1964)., 139, 1217

Trapman, L., Miotello, A., Kama, M., Van Dishoeck, E., & Bruderer, S. 2017, Astronomy & Astrophysics, 605, A69

Trapman, L., Rosotti, G., Zhang, K., & Tabone, B. 2023, The Astrophysical Journal, 954, 41

Trapman, L., Tabone, B., Rosotti, G., & Zhang, K. 2022, The Astrophysical Journal, 926, 61

Tripathi, A., Andrews, S. M., Birnstiel, T., & Wilner, D. J. 2017, , 845, 44

Tychoniec, Ł., Tobin, J. J., Karska, A., et al. 2018, The Astrophysical Journal Supplement Series, 238, 19

Ubach, C., Maddison, S. T., Wright, C. M., et al. 2012, Monthly Notices of the Royal Astronomical Society, 425, 3137

Urpin, V. & Brandenburg, A. 1998, Monthly Notices of the Royal Astronomical Society, 294, 399

van der Marel, N., Cazzoletti, P., Pinilla, P., & Garufi, A. 2016, The Astrophysical Journal, 832, 178

van der Marel, N., Van Dishoeck, E. F., Bruderer, S., et al. 2013, Science, 340, 1199

van Terwisga, S. E. & Hacar, A. 2023, , 673, L2

Wada, K., Tanaka, H., Okuzumi, S., et al. 2013, Astronomy & Astrophysics, 559, A62

Wada, K., Tanaka, H., Suyama, T., Kimura, H., & Yamamoto, T. 2009, The Astrophysical Journal, 702, 1490

Weder, J., Mordasini, C., & Emsenhuber, A. 2023, Astronomy & Astrophysics, 674, A165

Weidenschilling, S. 1977, Monthly Notices of the Royal Astronomical Society, 180, 57

Weingartner, J. C. & Draine, B. 2001, The Astrophysical Journal, 548, 296

Whipple, F. L. 1972, in From plasma to planet, 211

Williams, J. P. & Best, W. M. 2014, The Astrophysical Journal, 788, 59

Williams, J. P. & Cieza, L. A. 2011, Annual Review of Astronomy and Astrophysics, 49, 67

Winter, A. J. & Haworth, T. J. 2022, European Physical Journal Plus, 137, 1132

Woitke, P., Min, M., Pinte, C., et al. 2016, Astronomy & Astrophysics, 586, A103

Xu, W. & Kunz, M. W. 2021a, Monthly Notices of the Royal Astronomical Society, 502, 4911

Xu, W. & Kunz, M. W. 2021b, Monthly Notices of the Royal Astronomical Society, 508, 2142

Yang, C.-C., Johansen, A., & Carrera, D. 2017, Astronomy & Astrophysics, 606, A80

Youdin, A. N. 2011, The Astrophysical Journal, 731, 99

Youdin, A. N. & Goodman, J. 2005, The Astrophysical Journal, 620, 459

Youdin, A. N. & Lithwick, Y. 2007, icarus, 192, 588

Youdin, A. N. & Shu, F. H. 2002, The Astrophysical Journal, 580, 494

Yun, H. G., Kim, W.-T., Bae, J., & Han, C. 2019, The Astrophysical Journal, 884, 142

Zagaria, F., Rosotti, G. P., Alexander, R. D., & Clarke, C. J. 2023, The European Physical Journal Plus, 138, 25

Zagaria, F., Rosotti, G. P., Clarke, C. J., & Tabone, B. 2022, Monthly Notices of the Royal Astronomical Society, 514, 1088

Zhang, K., Blake, G. A., & Bergin, E. A. 2015, The Astrophysical Journal Letters, 806, L7

Zhu, Z., Nelson, R. P., Dong, R., Espaillat, C., & Hartmann, L. 2012, The Astrophysical Journal, 755, 6

Zhu, Z., Zhang, S., Jiang, Y.-F., et al. 2019, The Astrophysical Journal Letters, 877, L18

Zormpas, A., Birnstiel, T., Rosotti, G. P., & Andrews, S. M. 2022, Astronomy & Astrophysics, 661, A66

Zsom, A., Ormel, C. W., Güttler, C., Blum, J., & Dullemond, C. 2010, Astronomy & Astrophysics, 513, A57

Zubko, V., Mennella, V., Colangeli, L., & Bussoletti, E. 1996, Monthly Notices of the Royal Astronomical Society, 282, 1321

Acknowledgements

I would like to thank everyone in the research group of which I had the privilege of being a part during this PhD journey. I would also like to extend my gratitude to the close collaborators of the two projects I had the opportunity to lead during these doctoral years: Dr. Anna Miotello, Dr. Paola Pinilla, Dr. Claudia Toci, Prof. Dr. Giovanni Rosotti, Dr. Sean M. Andrews, Dr. Tommy Chi Ho Lau, Rossella Anania and Dr. Sebastian Stammler. I would especially like to thank my PhD supervisor, Prof. Dr. Til Birnstiel, for giving me the opportunity to collaborate with him and be a part of his research group. I am deeply grateful for the trust he placed in me and the support he provided every day throughout my PhD, and for being an outstanding supervisor as much on the scientific side as on the human side.

I would like to thank all the people who have supported me during this 10-year life journey. Thank you for your support and every single act of kindness. A final special thanks goes to all the people who set sail to be there during the stormy days.